Toughening Mechanisms and Deformation Behaviours of High-Thermal-Resistant Poly(Acrylonitrile-Butadiene-Styrene) (ABS)

Richard Lee

November 1999

A thesis submitted for the degree of Master of Engineering of The Australian National University.

Declaration

This thesis contains no material which has been accepted for the award of any other degree or diploma in any university. To the best of the author's knowledge and belief, no material previously published or written by another person has been included, except where due reference is made in the text.

Richard Lee
11 November, 1999

Acknowledgements

I am particularly indebted to my supervisor, Dr. B. Jar, (who originally suggested this project) for his encouragement throughout this project. I am also grateful that he read the draft of this thesis and offered very helpful advice and long discussions.

I wish to also thank my advisors for their important advice. They are Dr. S. Stowe of the *Electron Microscopy Unit* in the *Australian National University* (who has also reviewed my manuscript), and Dr. R. -Y. Wu of *Division of Molecular science* in *CSIRO* (Melbourne), Australia.

I am grateful to Prof. K. Takahashi of *Kyushu University*, Japan, for allowing me to use his laboratory equipment, particularly the Differential Scanning Calorimeter (DSC).

Appreciation is also extended to Mr. T. Shinmura and Mr. K. Konishi of *Denki Kagaku Co.* (Chiba), Japan, for their precious time and efforts in preparing the materials. In addition, I would like to thank Mr. L. D. McCarthy of *Division of Molecular Science* in *CSIRO* (Melbourne), Mr. D. Krivanek and Mr. B. Moscord of *Department of Engineering* in the *Australian National University*, Mr. F. Brink, Dr. R. Heady and Ms L. Chen of the *Electron Microscopy Unit* in the *Australian National University*, for their patience and time to show me the operations of the equipment.

I would like to thank the Targeted Institutional Links (TIL) program by DETYA and the Australian Research Council (ARC), Small Grant Scheme for the financial supports.

Finally, my gratitude must go to my girlfriend, Ms A. Wu and both our loving families for their supports and encouragement throughout the course.

Abstract of the thesis

The effects of rubber particle morphology on the toughness enhancement of high-thermal-resistant poly(acrylonitrile-butadiene-styrene) (ABS) were examined. Three types of ABS's were used. They were ABS1, ABS5 and ABS15. The ordinary ABS's used to blend with poly(styrene-N-phenyl-male-imide) (SMI) were DENKA's GT-8, GT-14 and a mixture of GT-8 and GT-14 in a ratio of 1:1, to make ABS1, ABS5 and ABS15, respectively. The blending ratio of SMI to SAN was 1:1 in all blends used in this work.

Three mechanical tests (static tensile, single-edge-notched (SEN) tensile and instrumented Izod impact test) show ABS1 is always tougher than its ABS5 or ABS15 counterparts. Scanning and transmission electron (SEM and TEM) micrographs show that particles in ABS1 favour cavitation; whereas in ABS5 they initiate crazes. Small angle X-ray scattering (SAXS) analysis indicates the main deformation mechanism in ABS1 is shear yielding whereas in ABS5 and ABS15 it is crazing. The only factor that was demonstrated to affect the different deformation mechanisms was particle structure.

This study also incorporated a thermal analysis of the blends using differential scanning calorimetry (DSC). The results show that all blends have a single glass transition temperature (T_g) and therefore an acceptable level of miscibility. Comparison between miscibility of the blends using Couchman's equation[1] indicates a decrease in miscibility of SMI/SAN with increase in acrylonitrile (AN) content. However, a high mismatch of AN content between two poly(styrene-co-acrylonitrile) (SAN) in SMI/SAN_x/SAN_y blends (SAN_x and SAN_y are two SANs with different AN content) increases the miscibility of SANs with SMI. The AN content effect was further studied in SAN copolymers. The mechanical and fracture behaviour of SAN copolymers shows that the increase of AN content from 23.4 wt% to 28.9 wt% increases the toughness of the materials.

This study concludes that high AN content can increase the inherent ductility of ABS and that particle structure is an important factor for toughness enhancement of rubber-toughened polymers.

LIST OF TABLES

LIST OF FIGURES

Symbols

Symbol	
ϕ	Volume fraction of polymer
χ	Interaction parameter of the polymer
ρ	Mass density
ν	Poisson's ratio
ΔC_p	Difference in heat capacity
ΔG_{mix}	Gibbs free energy of mixing
Δg_{mix}	Gibbs free energy of mixing per unit volume
a	Initial crack length
ABS	Poly(acrylonitrile-butadiene-styrene)
AN	Acrylonitrile
B	Binary interaction
Bt	Butadiene
DMA	Dynamic mechanical analysis
DSC	Differential scanning calorimeter
FE	Finite element
FTMD	Fourier transform micro-densitometry
HIPS	High impact polystyrene
K	Miscibility coefficient
K_I	Stress intensity factor for crack initiation from the pre-crack
LAED	Low-angle electron diffraction
M	Molecular weight
MAH	Poly(styrene-maleic-anhydride)
M_w	Molecular weight
MWD	Molecular weight distribution
N	Degree of polymerisation of polymer molecules
NMR	Nuclear magnetic resonance
OsO_4	Osmium tetroxide
PC	Polycarbonate
P_{max}	Maximum force
PMI	Phenyl-male-imide
PP	Polypropylene
PS	Polystyrene
PVC	Poly(vinyl chloride)
SAN	Poly(styrene-co-acrylonitrile)
SAN_{ABS}	Grafted SAN of ABS
SAN_g	Grafted SAN
SAN_m	Matrix SAN
SAXS	Small angle X-ray scattering
SEM	Scanning electron microscope
SEN	Single-edge-notched
SMI	Poly(styrene-N-phenyl-male-imide)
St	Styrene
T	Specimen thickness
T_c	Drying or annealing temperature

TEM	Transmission electron microscope
T_g	Glass transition temperature
V_r	Reference volume
w	Specimen width
W	Weight percent of the constituent polymer

CONTENTS

CHAPTER ONE

Introduction

1.1 An overview of the thesis

The usefulness of polymers in structural applications depends on their fracture toughness. Therefore much work has been done to develop effective mechanisms for toughening them. It is common practice for industries to toughen glassy polymers by adding rubbery particulates. Rubber particles increase the toughness of polymers by encouraging two deformation mechanisms: multiple crazing and shear deformation.

Crazing is a microscopic damage occurring in polymeric materials. Several groups have studied this deformation in pure polymers[2-4]. It is one of the main deformation behaviors that contribute to toughness enhancement, particularly for polymers with a lower stress threshold for crazing than for shear yielding. Under tensile stress, crazes are often initiated from a defect, and propagate in the direction perpendicular to the applied stress. As the craze thickness increases, fibrils are drawn, and their diameter reduced. Eventually voids are formed from the failure of fibrils, and crazes transform into cracks. When rubber particles are added to the polymer, stress is concentrated at the particle/matrix interface. As a result, crazes are initiated at relatively low applied stress. Crazes may also terminate at particles. Therefore the addition of rubber particles increases the volume fraction of small crazes, allowing substantial plastic strain before failure.

Shear yielding is another type of deformation that can occur in polymeric materials. It plays a major role in rubber-toughened polymers. It is the dominant deformation mechanism in some polymer systems, such as rubber-toughened poly(vinyl chloride) (PVC)[5-8], nylon[9-11], and epoxy[12-16]. It is generally accepted that shear bands are initiated from rubber particles[17]. Some studies demonstrate that shear yielding is usually accompanied by rubber particle cavitation[11, 15, 16]. Whether cavitation encourages shear yielding or vice versa is yet to be clarified. Cavitation of rubber particles occurs to relieve the build-up of hydrostatic tension, thereby

increasing the barrier for further craze initiation. This reduction in triaxial stress is deemed to encourage shear yielding.

The existence of shear yielding and particle cavitation has been studied for a decade. Yee and coworkers[18, 19] and Bucknall and coworkers[20] have demonstrated that in the case of shear-yielding-dominated materials, cavitation is a precursor of shear yielding. Their work is supported by Narisawa et al.[21], who used finite element (FE) modeling to show that cavitation occurs before shear yielding. Narisawa et al. have also shown that the bulk modulus of rubber particle increases as the Poisson's ratio approaches 0.5. The high bulk modulus induces high triaxial stress, which causes shear yielding[22].

In this thesis, multiple crazing and shear yielding will be shown to be the main deformation mechanisms for the high-thermal-resistant poly(acrylonitrile-butadiene-styrene) (ABS) materials. Whether crazing or shear yielding dominates the deformation behaviour is closely related to the type of rubber particles used. This is the main focus of this thesis. Different types of rubber particles are characterised by particle size and ligament thickness. This study will show that these parameters are not the main contributors to the toughening mechanisms. Other properties such as acrylonitrile (AN) content and molecular weight effects are also investigated.

Toughness of pure polymer blends can be increased by the addition of rubber particles[23]. The increased toughness of rubber-toughened polymers such as ABS can be attributed to the composition of the rubber particle[24], and the different type of the rubber particle[25]. Parameters affecting the properties of rubber-toughened polymer include molecular weight (M_w) of poly(styrene-co-acrylonitrile) (SAN)[26] and interfacial adhesion between particles and matrix[23]. Test variables including strain rate, notch sensitivity and temperature also affect the measured properties of the polymer.

Work on ABS blends performed by Donald and Kramer[25] showed that the size of rubber particles affects the deformation mechanisms. They observed in thin-film specimens that small particles (0.1 μm) cavitate more easily than large particles (1.5 μm), which initiate crazing. Another factor affecting rubber-toughened polymers was shown by Aoki[27], who reported that a low degree of grafting between rubber particles and the matrix could cause rubber particles to agglomerate in ABS materials. He concludes that particle agglomeration occurs at a critical grafting degree, which is

dependent on particle size. Chang[28], using a thermodynamic theory, suggested that particles agglomerate because of thermodynamic incompatibility between components. Kim et al.[29, 30] concluded that particle agglomeration was caused by AN content mismatch between matrix and grafted SAN. Kim and coworkers also demonstrated that the presence of slight particle agglomeration could be of advantage in toughening the materials.

The purpose of this work is to elucidate the effect of rubber particle structure on the deformation mechanisms in ABS materials subjected to varied straining rates. Not much work was done on strain rate effects. The existing work[5, 31] showed that increasing straining rate in PVC could reduce the stress whitening regions, and some[32, 33] showed that increasing the straining rate in high impact polystyrene (HIPS) would increase the energy for fracture.

Other parameters, such as the effects of AN content in SAN, particle size and molecular weight (M_w) are also discussed. Information provided in this work will facilitate the design of rubber-toughened polymers, by allowing more control over deformation behaviours.

The structure of the thesis is as follows:

The materials used and the testing methods are described in Chapter 2. The miscibility of the polymer blends, and the definition and determination of the miscibility, are the topics of Chapter 3. The mechanical results and the microscopic fracture behaviours of the polymer blends are assessed in Chapter 4. Chapter 5 discusses the effect of rubber particles on toughness of the polymer blends, and describes mechanisms of deformation. The final chapter is devoted to the conclusions of this work and indicates how this study relates to the material design.

CHAPTER TWO

Materials and Experimental Procedures

2.1 Introduction

Constituent materials of the blends used in this study are commercial products, supplied by *Denka Co.*, Chiba, Japan. The materials include poly(styrene-N-phenyl-male-imide) (SMI), poly(styrene-co-acrylonitrile) (SAN), and ordinary poly(acrylonitrile-butadiene-styrene) (ABS). They are blended together to create a new series of high-thermal-resistant ABS. Trade name: *Malecca K-series*.

The high-thermal-resistant ABS used in this study was purposely designed to study *(a)* the effect of AN content in matrix SAN (SAN_m) and *(b)* the effect of rubber particle type in the ABS. Chapter 4 suggests that variation of AN content also affects the strength in the interphase region between particles and matrix. However, this variation is yet to be evaluated; further experimentation is needed.

The basic structure of ABS is shown in Figure 2.1. Random copolymers of styrene (St) and acrylonitrile (AN) are grafted to butadiene (Bt) rubber. The chemical structures of the three monomers that make up ABS are shown in Figure 2.2.

The SMI copolymer was used to increase the ABS's glass transition temperatures (T_g), and was produced by post-imidisation of poly(styrene-maleic-anhydride) (MAH) to phenyl-male-imide (PMI). The overall mixing weight ratio of St:PMI:MAH is 45:53:2 for SMI used in this study. The chemical structure of SMI is shown in Figure 2.3.

2.2 Materials

Materials used for the study were SAN copolymer, binary blends of SMI/SAN copolymers, ternary blends of $SMI/SAN_x/SAN_y$ and 3 types of ABS blends. The ratio in all matrix materials, SMI to SAN, was maintained at 1:1. The SMI was used because of its high-thermal-resistance and low production cost. It has a glass transition temperature (T_g) of 196°C. However, because SMI is a brittle material

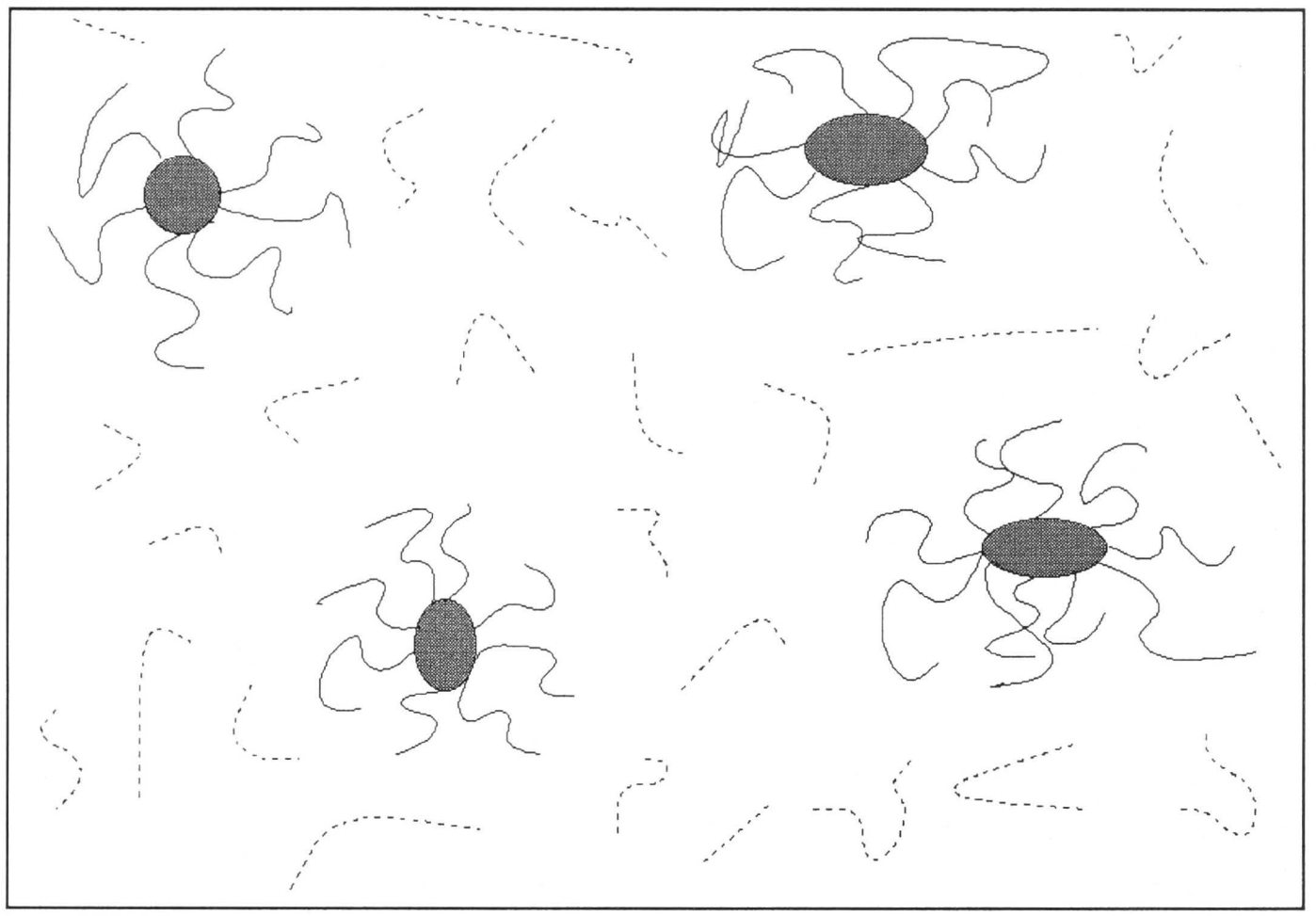

Figure 2. 1: A graphic representation of the basic structure of ABS. Spheres represent block polymer of butadiene, solid lines are the grafted random copolymers of styrene and acrylonitrile and the dotted lines the free random copolymers of styrene and acrylonitrile

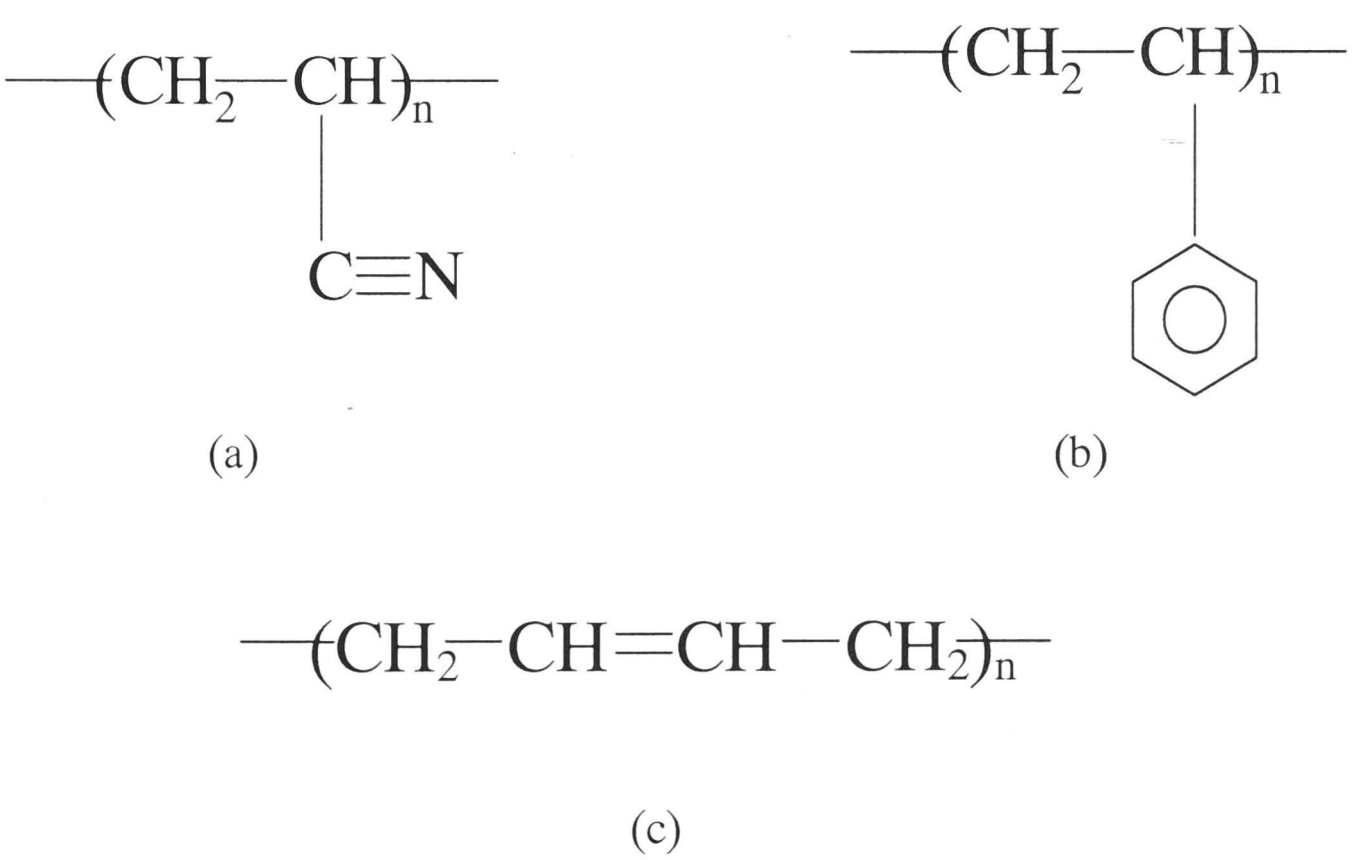

Figure 2. 2: Monomers that make up ABS. (a) acrylonitrile; (b) styrene; and (c) butadiene

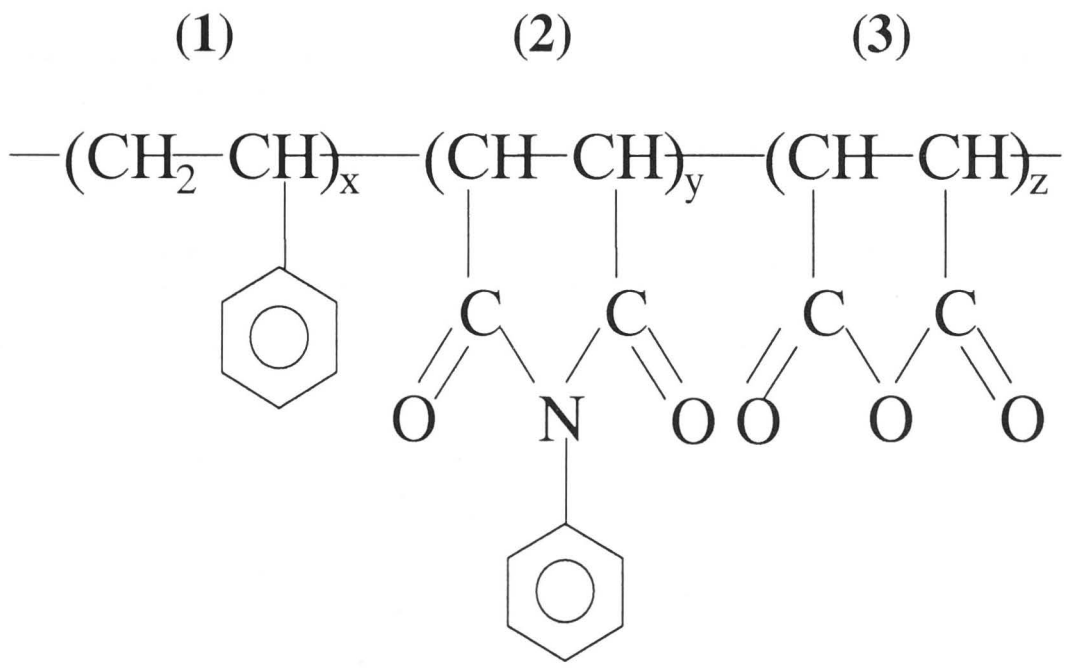

Figure 2. 3: Chemical structure of SMI copolymers; the first monomer (1) represents styrene, the second (2) represents phenyl-maleimide and the third (3), maleic-anhydride

having a critical stress intensity factor (K_{IC}) of 0.5 $MPam^{-1}$, SAN was added to enhance the toughness[34]. SAN has a K_{IC} of 2.2 $MPam^{-1}$ but a low T_g of around 100°C. In addition, it is miscible with SMI[35]. The AN content of SAN used in this work varies from 23.4 wt% to 28.9 wt%. This range of AN content allows us to study the effect of AN variation on the toughness of the materials. Table 2.1 below shows molecular weight (M_w) of the copolymers, as provided by the manufacturers.

***Table 2. 1*:** Properties of the polymers

Polymers type	***Monomers constituent***				***Monomers composition***	***Molecular weight (M_w ×1000)***
	St	**AN**	**PMI**	**MAH**	**① : ② : ③**	
SMI	①	-	②	③	45.0 : 53.0 : 2.0	167
SAN22	①	②	-	-	76.4 : 23.6 : -	121
SAN24	①	②	-	-	76.6 : 23.4 : -	198
SAN25	①	②	-	-	75.4 : 24.6 : -	113
SAN26	①	②	-	-	74.6 : 25.4 : -	122
SAN28a	①	②	-	-	71.1 : 28.9 : -	119

The three ABS's used are ABS1, ABS5 and ABS15. These are blends of ordinary ABS with SMI and SAN. ABS1 and ABS5 were blended using ordinary ABS-g-1 and ABS-g-5, respectively. ABS15 was from a mixture of ABS1 and ABS5 at a weight ratio of 1:1. The main difference between ABS1 and ABS5 is the particle structure (see Figure 2.4). The former has homogeneous particles, and the latter salami particles with SAN occlusions. Information on the properties of ABS1 and ABS5 is given in Table 2.2.

Table 2. 2: Summary of ABS properties from the producer

	Ordinary ABS type ABS-g-1	ABS-g-5
Commercial name	GT-8	GT-14
AN content in SAN_g (wt%)	23	23
Molecular weight of SAN_g (M_w ×1000)	60	65
Rubber content (wt%)	50	50
Grafting ratio (%)	35	N/A
Particle size / Distribution	0.1 μm and 0.5 μm / Bimodal	0.3 μm / Monomodal
Particle structure	Homogeneous	Salami

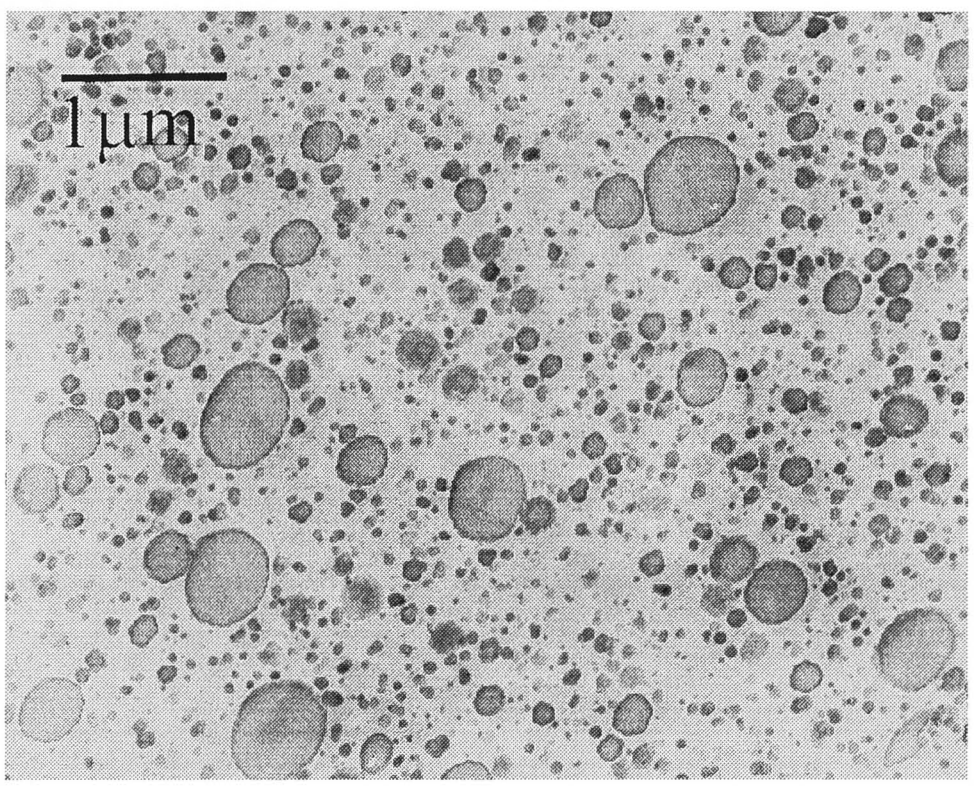

(a)

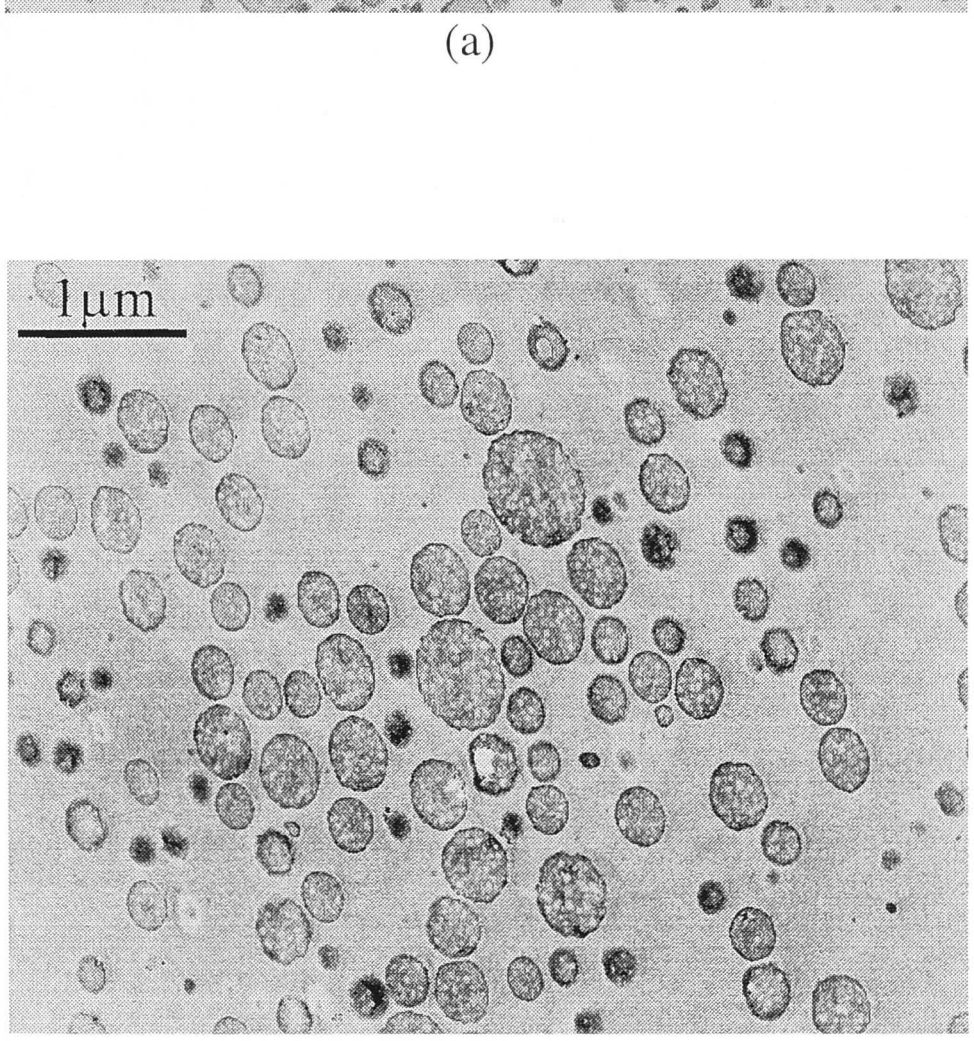

(b)

Figure 2. 4: Blend morphology of the modified ABS. (a) ABS1 having homogeneous particles; and (b) ABS5 having salami-structure particles

2.3 Production of blends and specimens fabrication

The materials were produced by melt mixing in a twin-screw extruder. The screw speed was set at 250 rpm. The extruded pellets were injection moulded into a dumb-bell shape in a mould set at 60°C. A total of 27 sets of specimens were produced, they differed in AN content and rubber particle structure. The type of materials used, together with the blends mixing ratio and the extrusion and injection moulding temperatures of the blends, are summarised in Tables 2.3 - 2.6. The barrel temperatures set in the extruder and injection-moulding machine are given in Table 2.7.

Table 2. 3: The extrusion and injection temperatures of SMI and SAN copolymers

Material no.	*Copolymer*	*Extrusion temp. (°C)*	*Injection temp. (°C)*
01	SMI	-	-
02	SAN22	-	251
03	SAN24	300	266
04	SAN25	294	254
05	SAN26	296	249
06	SAN28a	295	259

Table 2. 4: Mixing ratio of binary blends and the extrusion and injection temperatures

Material no.	*Binary blends*	*Mixing ratio SMI:SAN*	*Extrusion temp. (°C)*	*Injection temp. (°C)*
07	SMI/SAN22	1:1	300	275
08	SMI/SAN24	1:1	298	274
09	SMI/SAN25	1:1	289	275
10	SMI/SAN26	1:1	297	275
11	SMI/SAN28a	1:1	295	271

Table 2. 5: Mixing ratio of ternary blends and the extrusion and injection temperatures

Material no.	*Ternary blends*	*Mixing ratio SMI:SAN24:SAN*	*Extrusion temp. (°C)*	*Injection temp. (°C)*
12	SMI.SAN24/SAN22	2:1:1	296	272
13	SMI/SAN24/SAN25	2:1:1	291	274
14	SMI/SAN24/SAN26	2:1:1	294	270
15	SMI/SAN24/SAN28a	2:1:1	295	273

Table 2. 6: Mixing ratio of ABS blends and the extrusion and injection temperatures

Material no.	*ABS blends*	*Mixing ratio SMI:SAN:ABS*	*Extrusion temp. (°C)*	*Injection temp. (°C)*
16	SMI/SAN22/ABS1	2:1:2	294	277
17	SMI/SAN25/ABS1	2:1:2	297	284
18	SMI/SAN26/ABS1	2:1:2	296	282
19	SMI/SAN28a/ABS1	2:1:2	297	282
20	SMI/SAN22/ABS5	2:1:2	309	281
21	SMI/SAN25/ABS5	2:1:2	300	285
22	SMI/SAN26/ABS5	2:1:2	298	282
23	SMI/SAN28a/ABS5	2:1:2	308	281
24	SMI/SAN22/ABS15	2:1:2	300	276
25	SMI/SAN25/ABS15	2:1:2	297	282
26	SMI/SAN26/ABS15	2:1:2	298	284
27	SMI/SAN28a/ABS15	2:1:2	308	283

Table 2. 7: Cylinder temperatures of both extrusion and injection machines

Material no.	***Extrusion cylinder temperature (°C)***					
	C1	*C2*	*C3*	*C4*	*C5*	*C6*
03-06	230	280	280	280	280	280
07-27	260	280	280	280	280	280
	Injection cylinder temperature (°C)					
	H1	*H2*	*H3*	*H4*		
02-27	260	260	250	240		

Temperatures of the blends in the extruder and injection-moulding machine were higher than the set-up temperatures, as shown in Tables 2.3 - 2.7. This difference in temperature is attributed to the high viscosity of the blend, which introduces shear stress in the melt. It is therefore very difficult to have common processing temperatures for all materials used.

The dumb-bell specimens, with dimensions according to ASTM D638M, were used for simple tensile and SEN tensile tests, whereas Izod impact specimens were machined from the dumb-bell specimens according to ASTM D256. Each dumb-bell specimen was used to produce two Izod impact specimens. The schematic diagrams of the tensile and impact specimens are shown in Figure 2.5.

2.4 Mechanical property measurements

The mechanical tests conducted were simple tension for tensile strength and elongation, single-edge-notched (SEN) tension for stress intensity factor and Izod

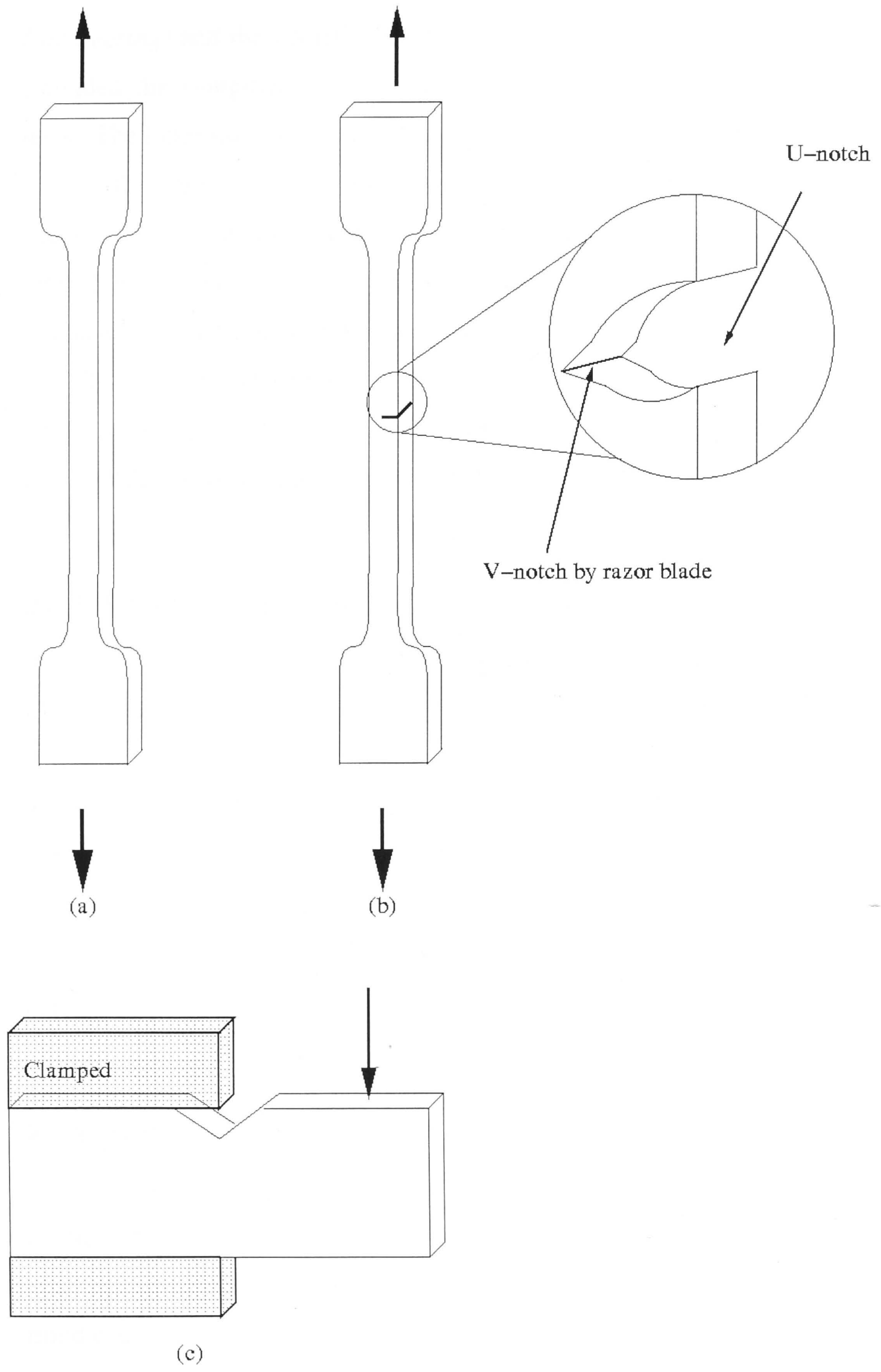

Figure 2. 5: (a) simple tensile specimen; (b) SEN tensile specimen and (c) Izod impact specimen

impact for fracture energy. These tests, carried out at room temperature, were performed in two institutions: the *Australian National University (Dept. of Engineering)* and the *CSIRO (Ian Wark Labs.)* in Melbourne. The former institution provided the equipment to carry out simple and single-edge-notched (SEN) tensile tests. The latter institution provided equipment for the Izod impact test.

The strain rate for the simple tensile test was 0.001 s^{-1}, measured from specimens with an extensometer (*low* strain rate). The Izod impact strain rate is termed *high* strain rate. According to Havriliak et al.[36], with notch size of 10 mil radius and impact speed of 3 m/sec, the strain rate for the Izod test corresponds is 200 s^{-1}. The notch introduced in the SEN tensile test generates a strain rate at the notch tip about 3-10 higher than the strain rate of simple tensile test, resulting in a strain rate between that of Izod impact and simple tensile strain rates (*intermediate* strain rate).

2.4.1 Simple tensile test

An *Instron 4505* universal-testing machine was used for the simple tensile test. The tests were done at a constant cross-head speed of 5 mm/min. An extensometer with a 2.5 mm gauge length was used in all pure polymer blends. The extensometer was attached to the middle gauge of dumb-bell specimens. ABS blends were tested without the extensometer.

The dumb-bell specimen's gauge length was 69 mm with a cross-section of 12.58 × 3.18 mm^2. A minimum of three specimens was tested from each sample batch.

2.4.2 Single-edge-notched (SEN) tensile test

Single-edge-notched (SEN) tensile specimens were tested at the same speed as in the simple tensile test. The SEN specimens measure stress intensity factors for crack initiation from the pre-crack (K_I). A U-notch was prepared by machining at the middle gauge. Prior to testing, a new razor blade was used to generate a sharp V-notch tip in front of the U-notch. The difference in V- and U-notches is shown in Figure 2.6.

The maximum force for fracture used for the calculation of K_I follows the equation:

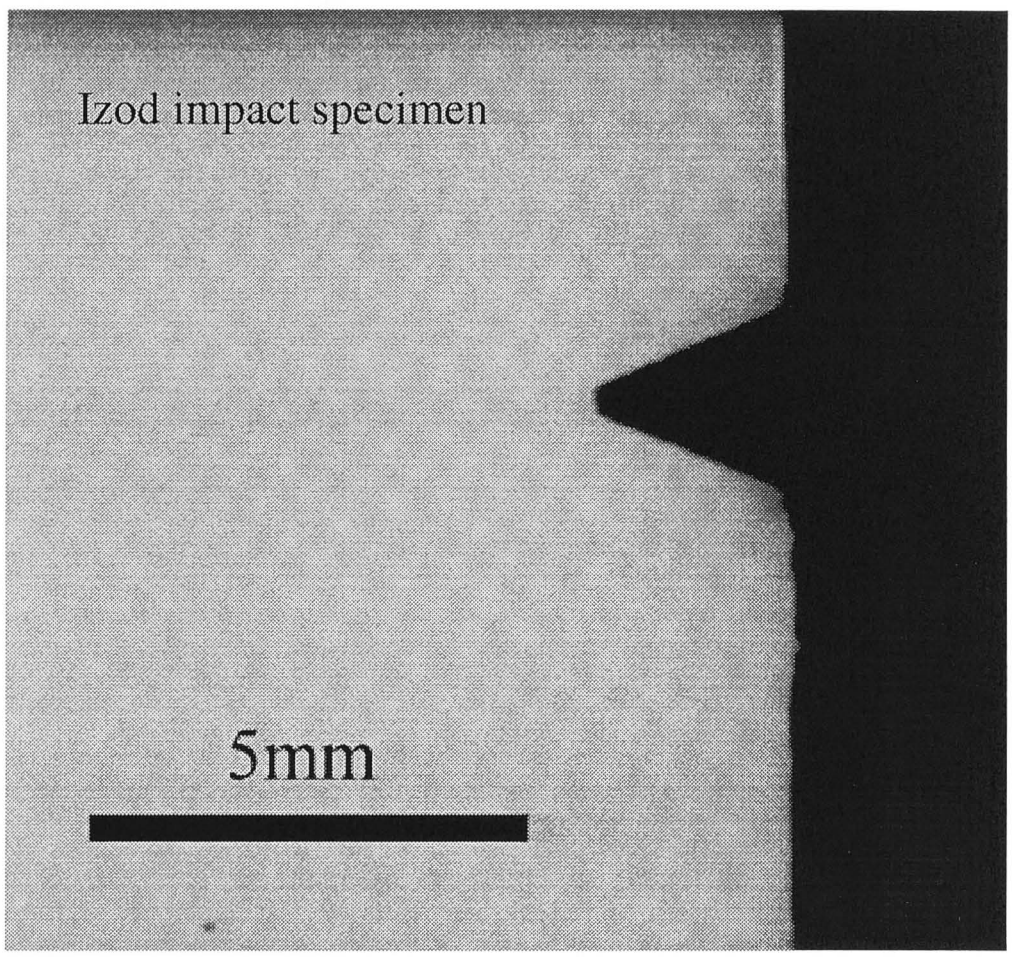

(a)

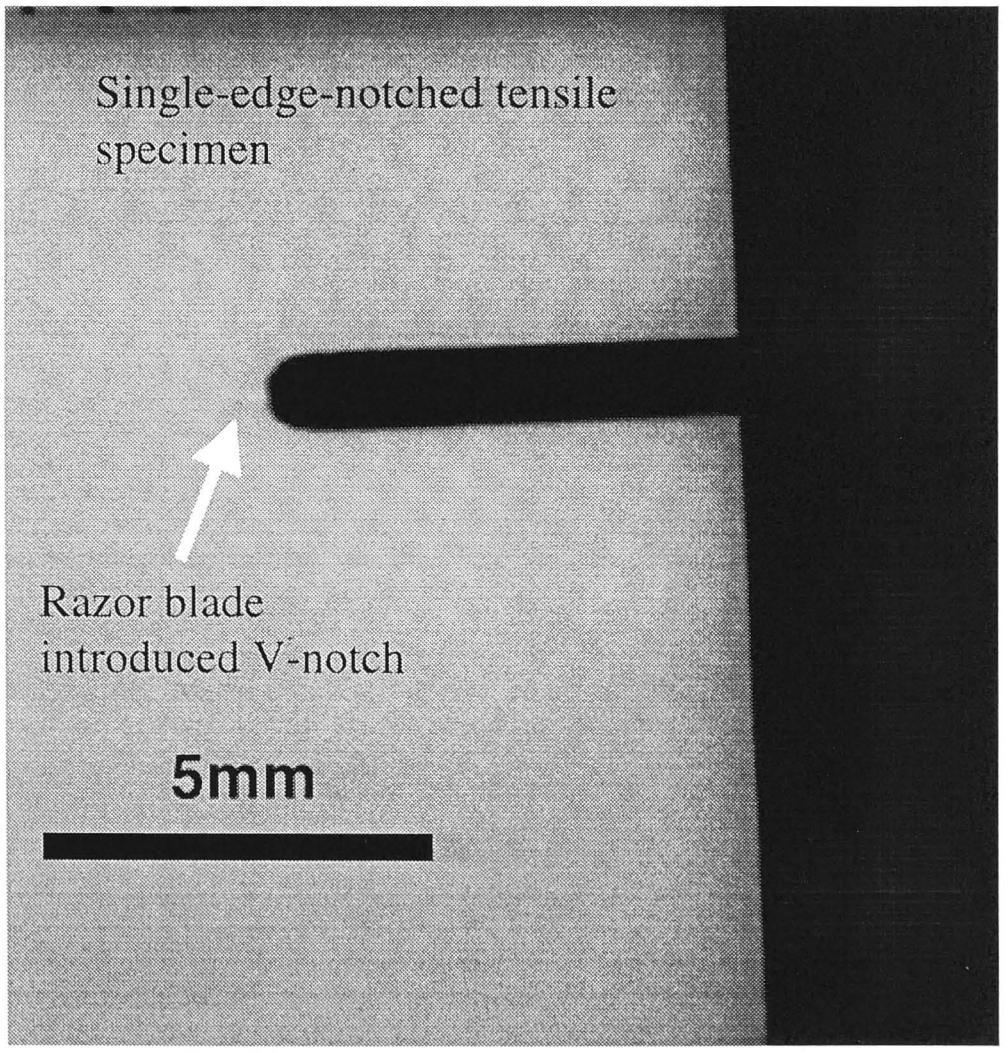

(b)

Figure 2. 6: Optical image of (a) Izod V-notch; (b) SEN machined U-notch and razor blade introduced V-notch

$$K_I = \frac{P_{\max}\sqrt{a}\,f(\frac{a}{w})^4}{Tw} \qquad \textbf{(2. 1)}$$

where,

$$f(\tfrac{a}{w}) = 1.12 - 0.231(\tfrac{a}{w}) + 10.55(\tfrac{a}{w})^2 - 21.72(\tfrac{a}{w})^3 + 30.39(\tfrac{a}{w})^4$$

P_{max} is the maximum force; w is the specimen width; a the initial crack length; and T, the specimen thickness. The initial crack length to width ratio $\left(\frac{a}{w}\right)$, was approximately 46 %.

2.4.3 Impact test

An instrumented Izod impact tester, *Radmana ITR 2000* (*CSIRO*, Melbourne), was used in this study. The impact specimen has the dimensions of 63.3 × 12.58 × 3.18 mm. The test set-up followed the requirements of ASTM D256. The position of the striker was set at 22 mm from the notch, and the initial impact velocity of the striker was 3.2 m/sec. A schematic diagram of the impact test set up is shown in Figure 2.7. A minimum of four specimens was tested for each blend.

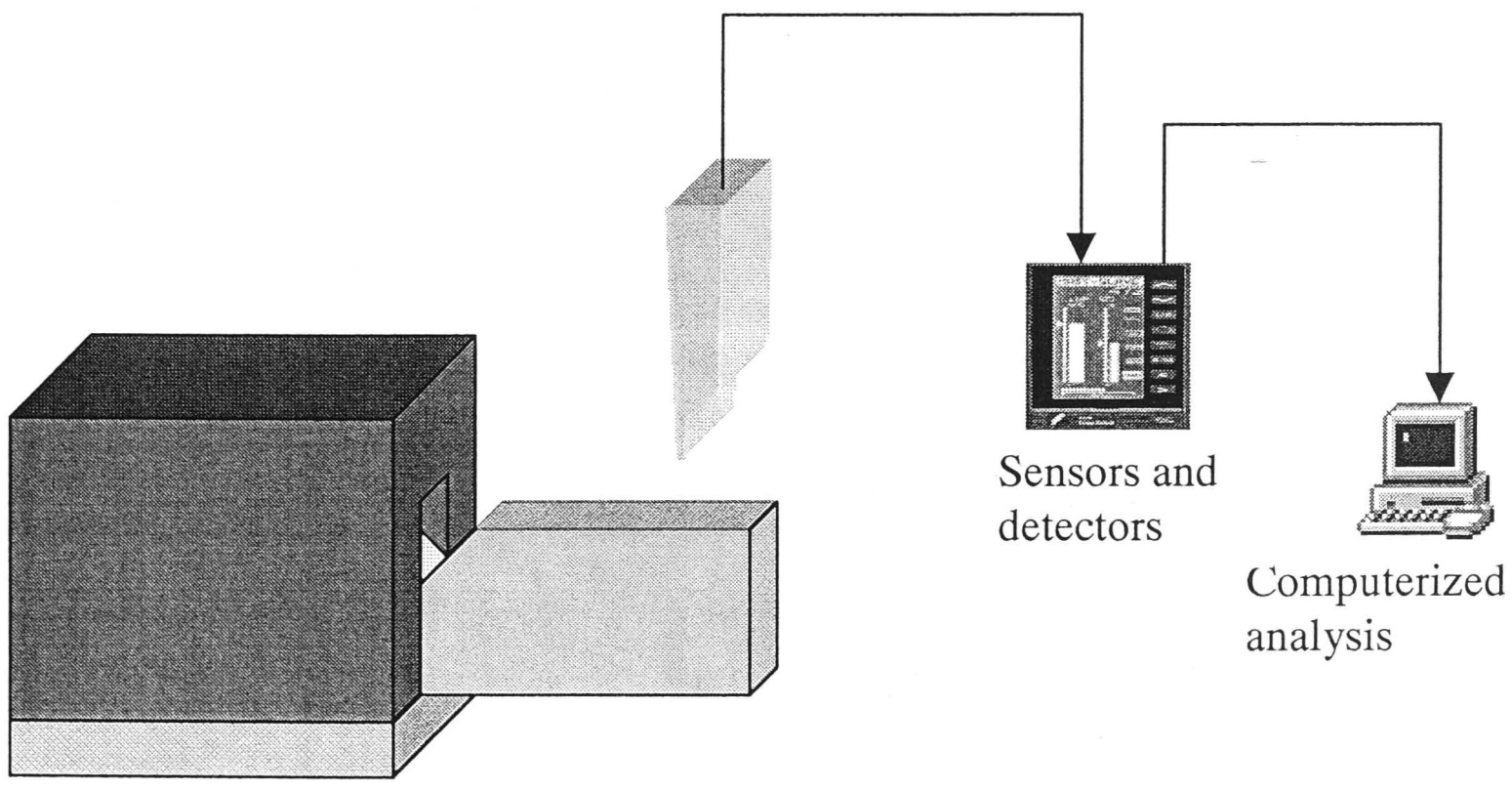

Figure 2. 7: The schematic diagram of the instrumented Izod impact test

2.5 Thermal analysis

Thermal analysis was conducted to determine the glass transition temperature (T_g). A differential scanning calorimeter (DSC), *Seiko Instruments DSC 120* (*Kyushu University*, Kyushu), was used with heating and cooling rates of 5 $Kmin^{-1}$.

The materials were prepared using a slow cutter to cut the dumb-bell specimens to a thickness of about 1.5mm. The materials were then polished on both surfaces using 1200-grade sandpaper, to remove any oil-stains introduced during the slow cutting.

The sample was cut to a dimension of about 4 × 4 mm^2 (7-9 mg) and placed in DSC aluminum pan. The sample was scanned in two heating cycles. The first cycle allowed the materials to create good contact with the pans' surfaces. After the first heating cycle, the sample was cooled to slightly above room temperature before starting the second heating cycle. T_gs of the blends were measured in the second heating cycle. For pure SAN copolymers, due to possible polymerisation during heating, T_gs were measured in the first heating cycle.

Figure 2.8 gives the scanning program in the DSC analysis. The maximum heating temperatures were 240°C for SAN copolymers and 290°C for the other blends.

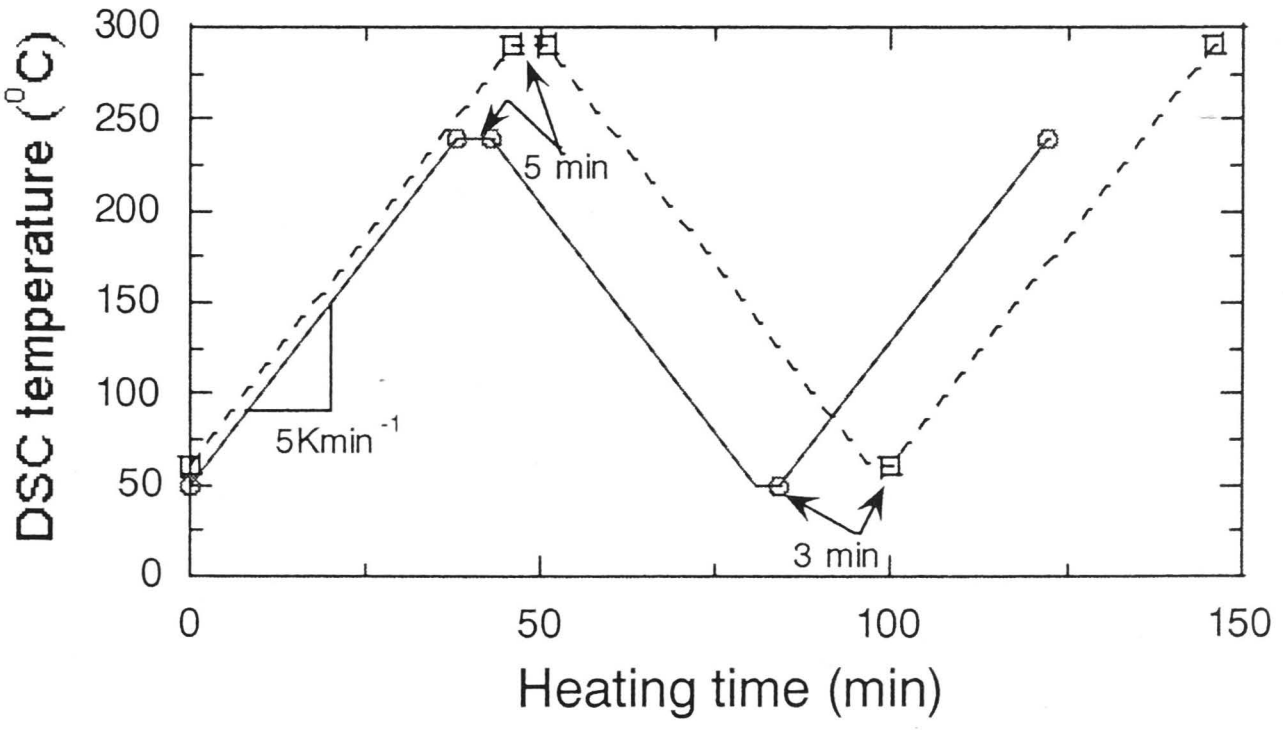

Figure 2. 8: Scanning programs of DSC analysis, solid line for pure SAN, dash line for other blends

2.6 Fracture surface analysis

After each mechanical test, the fractured pieces were carefully stored in a cool, dark place for future fracture analysis.

The fracture behaviours of the materials were examined by scanning and transmission electron microscopy. Materials with SAN22 and SAN28a constituents were chosen for the fracture analysis because of their extremes in mechanical properties.

To prepare the specimens for examination in the electron microscopes, the fractured specimens were hand-sawn using a jeweler's saw. The test piece was sawn at around 5-7 mm from the fractured surface.

2.6.1 Scanning electron microscopy (SEM)

Hand sawn specimens were glued onto SEM stubs with double-sided carbon sticky tape. The samples were gold-sputter-coated using a *Polaron E5000 SEM Coating Unit*. A gold layer of around 200 Å was deposited on the sample under a 0.04 Torr argon at 0.7 KV, 5 mA for 12 min. For comparison, some users coated with a thicker, faster coat (1.2 KV, 20 mA, 3 min).

A *Cambridge S360 SEM* was used for fracture behaviour analysis. The image was recorded on 70 mm *Kodak Plus-X Pan* film. Unless otherwise stated, fractured surfaces examined by SEM were taken near the initiation spot before fast fracture.

2.6.2 Transmission electron microscopy (TEM)

The hand-sawn simple tensile specimens were clamped directly into the microtome chucks, leaving the initiation region at a distance of about 2 mm from the clamps. As for the SEN tensile and Izod specimens, a third of the un-notched end of the specimen was trimmed off with a sharp razor blade. The specimen was then glued onto a block of Araldite resin (*Araldite 502*). The block allows the specimens to be firmly clamped in the chuck for trimming. In the case of simple tensile specimens, crazes around the initiation regions were examined. For the notched specimens, crazes from initial crack growth were examined.

For TEM analyses, ultra thin sections 60-70 nm thick were taken from the initiation zones of fractured specimens, with planes perpendicular to the fractured

surfaces. The sections were prepared by first trimming the section into a trapezoid, with the fractured surface as one of the edges as shown in Figure 2.9. Secondly, the trimmed surface was clean cut with glass knives. Trimming and microtoming were done with a *Reichert-Jung Ultracut* microtome.

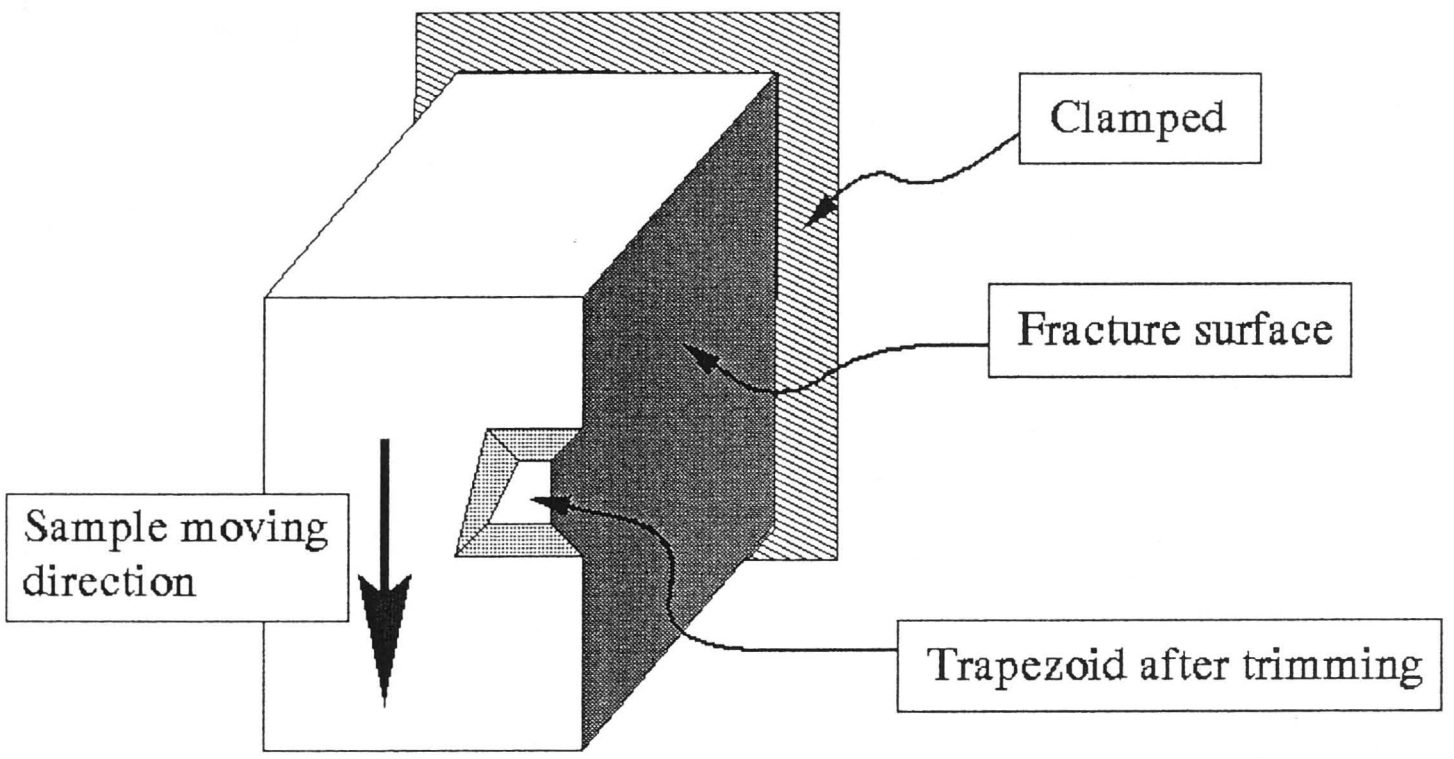

Figure 2. 9: Schematic diagram of specimen microtoming

After being cut with glass knives, the ABS materials were stained in vapour over a 2 wt% aqueous solution of osmium tetroxide (OsO_4) for no more than 48h, prior to microtoming with a diamond knife (*Diatome*). The OsO_4 staining is necessary, as it makes the rubber particles in ABS brittle enough for microtoming. Staining also assists in identifying the rubber particles under TEM. It provides a contrast between the rubber particles and the SMI/SAN matrix phase. Polymer blend specimens were microtomed immediately after being cut with glass knives. The microtomed pieces were picked up using thin bar *600 mesh hexagonal* copper grids. Figure 2.10 shows the procedures for preparing the microtomed samples.

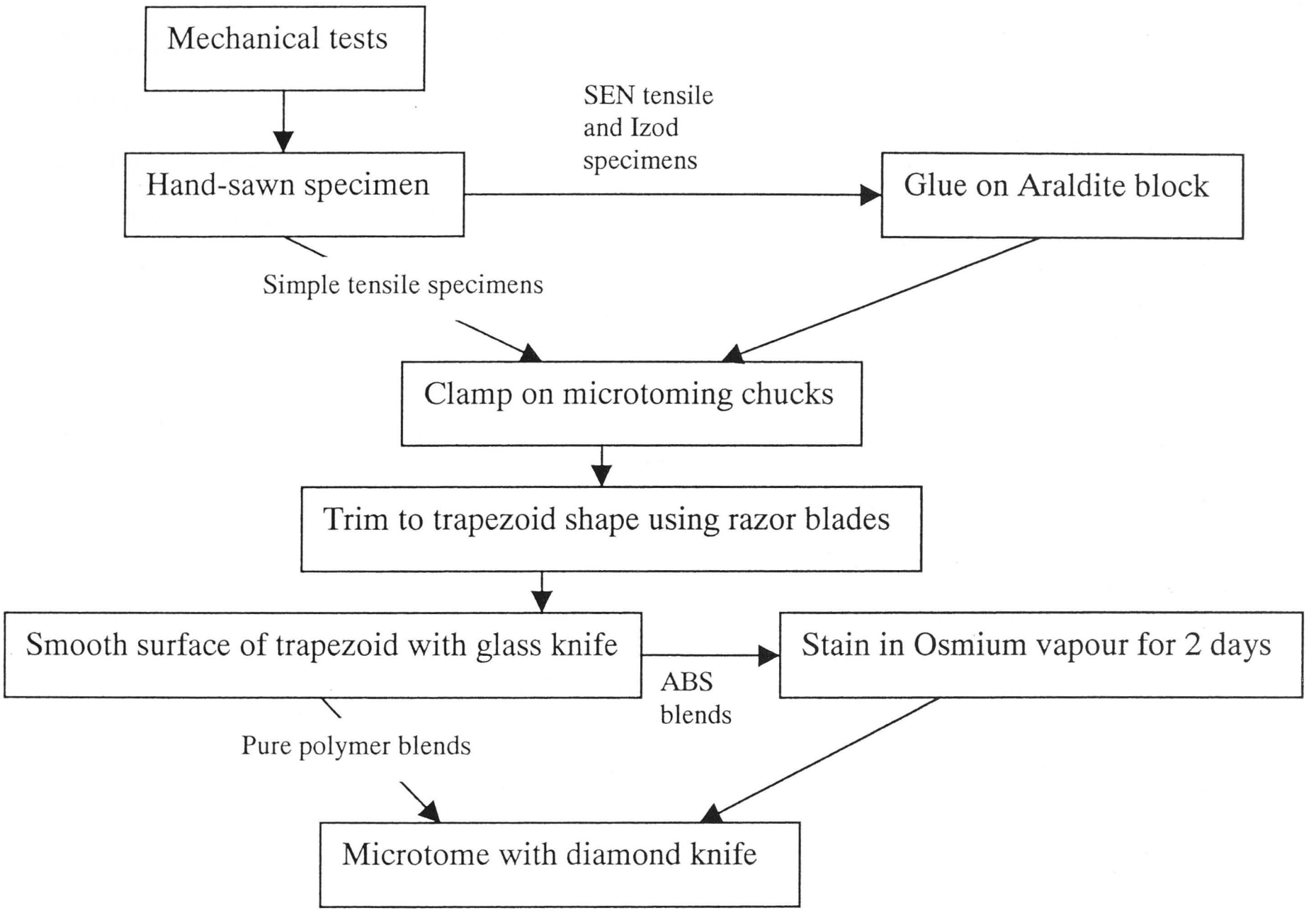

Figure 2. 10: Flow chart of sample preparation for microtoming

All samples were microtomed near the initiation spot, unless otherwise stated. Sections were examined with a *Hitachi 7100 TEM* at 75KeV. The film used was *Kodak SO-163* film.

2.6.3 Small angle X-ray scattering (SAXS)

The mechanically-tested specimens were tested by Dr. Jar in a SAXS experiment carried out in Japan. The SAXS was to confirm the presence of shear yielding in the materials. Therefore, only limited sets of specimens were tested. They were simple tensile specimens with SAN28a constituents for ABS1, ABS5 and ABS15, and Izod specimens with SAN22 and SAN28a constituents for both ABS1 and ABS5.

Four different locations on the specimens were examined by SAXS. *Location 1* was 4 mm above the fracture surface; *location 2* on the edge of the fracture surface; *location 3* 0.6 mm under the fracture surface; and *location 4* 3.6 mm under the fracture surface. The SAXS beam size was 0.4 mm in diameter. Further details of the SAXS method are given by Jar[37].

CHAPTER THREE

Miscibility of the polymer blends

3.1 Introduction

Polymer blends are used in commercial applications as they are relatively inexpensive products, which remedy the deficiency in performance of existing homopolymers. Developing polymer blends takes less time and effort than developing a completely new homopolymer of similar properties. For these reasons, polymer blends are used in most engineering applications. Improving the interfacial adhesion between polymer phases can enhance toughness of the materials. Without good interfacial adhesion, polymer blends would not have the generic properties of the individual polymer constituents. It is widely recognised that studying interfacial adhesion is the first step in understanding polymer blends. The molecular interaction at the interfacial region is studied in this chapter by investigating the polymer-polymer miscibility.

The term "miscible" is used here to describe blends that are resistant to phase separation and able to yield the macroscopic properties of a single-phase material. It does not necessarily imply ideal molecular interactions but shows homogeneity at a molecular level[38]. Polymer-polymer miscibility can be investigated and elucidated[39, 40] by direct methods or indirect methods. A direct method can be used for amorphous polymers by checking the opacity of the blends. The indirect method involves calculating the interaction parameters through a mathematical approach. Other methods include observing the glass transition temperatures of the blends experimentally. In this work, an indirect thermodynamic approach was used, in conjunction with thermal analysis, to evaluate the miscibility.

From the thermodynamic point of view, every polymer has some solubility in other polymers. However, the chance of having a miscible blend is exceedingly smaller than that of having an immiscible blend[41]. The miscibility of mixtures of polymers is determined by measuring the glass transition temperature (T_g) through thermal analysis. The use of T_g to elucidate polymer-polymer miscibility is based on

the assertion that blends with a single T_g are miscible, and blends with multiple T_gs are immiscible. However, if constituents have similar T_gs, other techniques must be used to determine miscibility of the constituents.

Two systems of polymer blends were investigated in this study, binary blends consisting of poly(styrene-phenyl-N-maleimide) (SMI) and poly(styrene-co-acrylonitrile) (SAN) copolymers and ternary blends consisting of SMI and two SANs of different acrylonitrile (AN) content. By varying the AN content in the SAN, the degree of miscibility in the blends was determined.

The SMI is a brittle polymer with a T_g of 196°C[42]. By blending SMI with SAN, which is a tougher material with a T_g of around 100°C, a blend with a T_g higher than 100°C and good toughness is obtained.

3.2 Experimental determination of miscibility

There is no single method that can unambiguously elucidate the polymer-polymer miscibility in all blend systems. One way to determine miscibility of constituents is by electron microscopy that relies on detecting a contrast in electron density between the phases, and often requires staining. Another method of studying miscibility involves measuring the material refractive indices, but this method has proved unreliable in principle as well as in practice.

The arguably reliable but sophisticated way to determine polymer-polymer miscibility is by studying the glass transition temperatures (T_g) of the blends using thermal analysis. Methods by which the T_g of polymers may be determined include differential scanning calorimetry (DSC), dynamic mechanical analysis (DMA), and nuclear magnetic resonance (NMR). Each of these techniques has advantages and limitations. Details for comparison of the methods can be found in[43, 44]. In this work, DSC is used for its ease of operation and accessibility. The specifications of the DSC can be found in the previous chapter.

With the T_g obtained, the miscibility of the blend can be calculated by using Couchman's equation to determine the *K*-value[1], as defined in Equation 3.7. There is considerable controversy over the use of *K*-value to find the blend miscibility[39], especially when miscibility is compared among blends of different constituents. In our study, the blends are of similar constituents. The only difference in the blends is the acrylonitrile (AN) content in the SAN of the blends. In addition to the miscibility

evaluation using the *K*-values, a thermodynamic approach to an understanding of polymer blends is briefly discussed in a latter section of this work.

3.3 Theoretical discussions

Thermodynamics theory is popular in describing polymer-polymer miscibility. Based on Flory's[45] and Huggins'[46] theory, Scott[47] obtained an expression for the Gibbs free energy of mixing:

$$\Delta G_{mix} = \left(\frac{RTV}{V_r}\right)\left[\left(\frac{\phi_A}{N_A}\right)\ln\phi_A + \left(\frac{\phi_B}{N_B}\right)\ln\phi_B + \chi_{AB}\phi_A\phi_B\right] \qquad \textbf{(3. 1)}$$

where V_r is the reference volume, ϕ the volume fraction of polymers A and B (represented by subscripts *A* and *B*), N the degree of polymerisation of polymer molecules, and χ the interaction parameter of the polymers.

In the above equation, V_r has been difficult to obtain[48]. Its misuse has been heavily criticised by Paul and his colleagues[49].

Equation 3.1, representing the Gibbs free energy of mixing per unit volume (Δg_{mix}), can also be represented as a van Laar expression for a binary blend[41]:

$$\Delta g_{mix} = RT\left[\frac{\rho_A\phi_A\ln\phi_A}{M_A} + \frac{\rho_B\phi_B\ln\phi_B}{M_B}\right] + B\phi_A\phi_B \qquad \textbf{(3. 2)}$$

where ρ is the mass density, M the molecular weight and B the binary interaction energy density.

For a binary blend system of SMI/SAN, the B for the mixing is given by:

$$\begin{aligned} B = {} & B_{12}\left(\phi_1''\phi_2' - \phi_1'\phi_2'\right) + B_{13}\left(\phi_1''\phi_3' - \phi_1'\phi_3'\right) + B_{14}\left(\phi_1'\phi_4'' - \phi_1''\phi_4''\right) \\ & + B_{24}\phi_2'\phi_4'' + B_{34}\phi_3''\phi_4'' - B_{23}\phi_2'\phi_3' \end{aligned} \qquad \textbf{(3. 3)}$$

where subscripts *1*, *2*, *3*, and *4* represent monomers St, PMI, MAH and AN, respectively. The superscripts ′and ″ represent copolymer SMI and SAN, respectively.

A stability analysis by Takakuwa et al.[50] shows that the binary mixture is miscible when B is less than a critical value. This is represented by:

$$B_c = \frac{RT_c}{2}\left[\sqrt{\frac{\rho_A}{M_A}} + \sqrt{\frac{\rho_B}{M_B}}\right]^2 \qquad \textbf{(3. 4)}$$

where T_c is the drying or annealing temperature.

The miscibility of the blends can be predicted with the known binary interactions (B). Unfortunately, the true values of B for these materials are not known. The problem was attempted by Jar et al.[51], to predict B_{ij} values that were then used to estimate miscibility of the constituent polymers. However, experimented evidence to support the values is yet to be obtained.

3.4 The glass transition temperature (T_g) and polymer-polymer miscibility

The glass transition temperatures (T_gs) of the materials were determined using a DSC. Details of the experiment are in Chapter 2. The T_gs of the materials are summarised in Table 3.1.

Table 3. 1: The glass transition temperature of various polymer blends varying in AN content

SAN_x Type	**SAN_x Copolymer (^oC)**	**Binary Blends (SMI/SAN_x) (^oC)**	**Ternary Blends (SMI/SAN24/SAN_x) (^oC)**
SAN22	102.2	127.3	127.5
SAN24	106.9	129.0	*N/A*
SAN25	106.8	130.0	129.5
SAN26	107.7	130.4	129.6
SAN28a	107.8	130.0	129.1

Various researchers have determined the miscibility of polymer blends by examining the T_g[43, 52]. This method relies on the fact that one T_g implies miscibility and two or more T_gs imply immiscibility. Both Eisenberg[52] and MacKnight[43] have stated that if the blend is miscible, the T_g of the blend can be obtained by the following equation:

$$\frac{1}{T_g} = \left(\sum_x \frac{W_x}{T_{gx}} \right) \tag{3. 5}$$

where W is the weight percentage of the constituent polymers and T_{gx} refers to the glass transition temperature of polymer x.

Couchman[1] established a relationship between T_g and compositional variation in polymer blends, based on classical thermodynamics theory, with the following equation:

$$\ln T_g = \frac{\left[\sum_i W_i \Delta C_{pi} \ln T_{gi} \right]}{\left[\sum_i W_i \Delta C_{pi} \right]} \tag{3. 6}$$

where ΔC_p is the difference in heat capacity before and after the mixing and i the number of monomers in the blends.

The following equation is obtained for a binary blend by substituting $\frac{\Delta C_{p2}}{\Delta C_{p1}} = K$ into Equation 3.6:

$$W_1 \ln\left(\frac{T_g}{T_{g1}} \right) + KW_2 \ln\left(\frac{T_g}{T_{g2}} \right) = 0 \tag{3. 7}$$

where K is the miscibility coefficient.

The K-value ranges from 0 to 1 if $T_{g1}<T_{g2}$, or ∞ to 1 if $T_{g2}<T_{g1}$ (where T_g is between T_{g1} and T_{g2}), thus representing completely immiscible to totally miscible. The subscript *1* and *2* refer to polymer 1 and 2.

In this study, blending ratio of the binary blends is 1:1, for SMI:SAN. SMI and SAN are represented by subscripts *1* and *2*, respectively. With the weight percentage W_1 and W_2 equaled, Equation 3.7 is simplified to:

$$\ln\left(\frac{T_g}{T_{g1}}\right) + K\ln\left(\frac{T_g}{T_{g2}}\right) = 0 \qquad \textbf{(3. 8)}$$

Ternary blends are produced by mixing SMI with SAN_x and SAN_y, where SAN_x and SAN_y are SANs with different AN content. The mixing ratio of SMI:SAN_X:SAN_Y is 50:25:25. Assuming the ternary blend consists of two binary blends, SMI/SAN_x and SMI/SAN_y both have a 50:50 weight-mixing ratio, the sum of the two binary blends from Equation 3.8 can be modified to:

$$\ln\left(\frac{T_{ga}}{T_{gSANx}}\right) + K_a\ln\left(\frac{T_{ga}}{T_{gSMI}}\right) + \ln\left(\frac{T_{gb}}{T_{gSANy}}\right) + K_b\ln\left(\frac{T_{gb}}{T_{gSMI}}\right) = 0 \qquad \textbf{(3. 9)}$$

where T_g represents the glass transition temperature and subscripts *a* and *b*, the binary blends a and b.

Assuming that a single *K*-value represents miscibility between SMI and the two SANs, that is $K = \frac{K_a + K_b}{2}$, the above equation becomes:

$$\ln\left(\frac{T_g}{T_{gSANx}}\right) + \ln\left(\frac{T_g}{T_{gSANy}}\right) + 2K\ln\left(\frac{T_g}{T_{gSMI}}\right) = 0 \qquad \textbf{(3. 10)}$$

3.5 Miscibility state of the blends

The calculations of miscibility coefficients of the binary and ternary blends, based on Couchman's equation are given in Table 3.2. The table shows that in the binary blends, the blend of SAN24 has an exceptionally low miscibility compared to other blends. The low miscibility is presumably caused by the high molecular weight (M_w) of the SAN24 copolymer. This hypothesis is supported in the ternary blends, where the SAN24 copolymer was one of the blend constituents. The miscibility values of the ternary blends exhibit lower *K*-values than their binary counterparts.

Table 3. 2: The *K*-values of binary and ternary blends varying in AN content

SAN_x Type	**Binary Blends (SMI/SAN_x)**	**Ternary Blends (SMI/SAN24/SAN_x)**
SAN22	0.509	0.462
SAN24	0.449	*N/A*
SAN25	0.479	0.464
SAN26	0.469	0.456
SAN28a	0.456	0.442

Neglecting the high M_w in the SAN24 blends, the trend of decreasing miscibility with increasing AN content in both binary and ternary blends is obvious. It is thus confirmed that the increase in AN content from 23.6 wt% to 28.9 wt% decreases the interaction between SAN and SMI. The similar effect of a decrease in miscibility with the increase in AN content of SAN has been observed previously[49, 53, 54].

However, in comparing the *K*-value difference between SAN22 and SAN28a in binary and ternary blends, the miscibility of ternary blends does not decrease as much as the binary blends. The *K*-value difference between binary and ternary blends, reveals less difference in *K*-value with regard to SAN28a blends than SAN22 blends. The results are summarised in Table 3.3. This indirect estimation reveals the ternary blends with a high AN content uphold better miscibility between SMI and SAN than binary blends. The hypothesis is that the repulsion between the SANs of different AN content allows the SANs to have better interaction with SMI copolymers, thus forming more miscible blends. This concept was drawn from Molau's work[55], which showed that the AN content mismatch in SANs of 5 wt% or more induces phase separation. Therefore, by increase in the AN content mismatch in the ternary blends, SANs become more miscible with SMI.

Table 3. 3: The *K*-value difference between binary and ternary and SAN22 and SAN28a

	Binary	*Ternary*	*K-value difference*
SAN22	0.509	0.462	***0.047***
SAN28a	0.456	0.442	***0.014***

	SAN22	*SAN28a*	*K-value difference*
Binary	0.509	0.456	***0.053***
Ternary	0.462	0.442	***0.020***

This finding can be used to infer a miscibility trend for the poly(acrylonitrile-butadiene-styrene) (ABS) systems. It is known that the AN content of grafted SAN (SAN_g) in ordinary ABS used in this work is 23 wt%. Increasing AN content in the SAN matrix (SAN_m) will increase the AN content mismatch between SAN_g and SAN_m, therefore the blend miscibility should increase with SMI. This increase in AN content for the ABS systems creates an overall decrease in miscibility between SANs but simultaneously, the decrease in miscibility between SANs is compromised with the increase in their interaction with SMI.

The T_gs of the ABS's are given in Table 3.4. ABS1 and ABS5 show a trend of the T_g increasing to a plateau with the increase in AN content. However, ABS15 systems do not show the trend. The *K*-values of the ABS blends were calculated and shown in Table 3.5. It does not show any direct trend in the miscibility of the matrices with AN content. It is possible that the SMI ratio added during processing was not consistent. It is not possible to determine the amount of SMI added quantitatively. However, it can be concluded that the inconsistency in SMI content was too small to be revealed in T_g analysis, and not show any apparent effect on the mechanical properties of the blends. This inconsistency of the SMI disables the *K*-values of ABS blends to be compared. Another factor that limit the comparison of *K*-values in ABS blends was that the ABS products employed in this research contain both grafted and ungrafted SAN. Because the ABS's used have different grafting ratios, evaluating the miscibility of the ABS matrices using *K*-values cannot be well quantified.

Table 3. 4: The glass transition temperature of ABS blends with varying AN content

SAN_x	**ABS1 (°C)**	**ABS5 (°C)**	**ABS15 (°C)**
SAN22	128.2	129.5	131.4
SAN25	132.7	132.5	133.0
SAN26	133.1	133.0	131.2
SAN28a	133.8	133.6	133.1

Table 3. 5: The *K*-values of ABS blends

SAN_x	**ABS1**	**ABS5**	**ABS15**
SAN22	0.534	0.571	0.628
SAN25	0.557	0.551	0.566
SAN26	0.547	0.544	0.492
SAN28a	0.566	0.560	0.542

3.6 Conclusive remarks

All the blends analysed using DSC show single T_g. This shows that the blends are in the miscible range. The *K*-value, or miscibility coefficient has been used to compare the miscibility of blends in this study. It is clear that high M_w reduces the *K*-value, and therefore the miscibility of the blends. Similarly, the increase in AN content reduces the blends' miscibility, with the miscibility still in the miscible range the AN content from 23.6 wt% to 28.9 wt%. In contrast, the T_g increases to a plateau with increasing AN content.

It is also shown in the ternary blends that the interaction between SAN and SMI increases with the increase in repulsion between SANs, at least in the range of AN content used in this study. The SMI added to the ABS blends was believed to be inconsistent with the specifications, therefore the comparison of miscibility in matrix polymers of ABS blends cannot be made.

This work provides a basis for the following chapters regarding the molecular interaction at the interface of rubber particles and matrix.

CHAPTER FOUR

Deformation and fracture of polymer blends

4.1 Introduction

This chapter focuses on the mechanical behaviours of polymer blends that are the matrix in the high-thermal- resistant poly(acrylonitrile-butadiene-styrene) (ABS), that is, blends of poly(styrene-N-phenyl-maleimide) (SMI) and poly(styrene-co-acrylonitrile) (SAN). The materials studied also include pure SAN copolymer and blend of SMI with SAN. Studying the mechanical properties of these polymers allows a better understanding of matrix deformation.

Three types of testing were performed on the polymer blends; simple tensile, single-edge-notched (SEN) tensile and Izod impact. The mechanical properties determined from these tests are later associated with the growth and breakdown of crazes observed by electron microscopy. No attempt was made to consider the craze nucleation. However, this type of work has been presented elsewhere[56, 57].

Owing to the separation of fibrils, crazes have a lower density than the bulk polymer. The lower density of the crazes can be contrasted with undeformed regions by using transmission electron microscopy (TEM). In this study, a scanning electron microscope (SEM) was also used to examine fracture behaviour of the polymer blends specimens. All samples studied by TEM and SEM were taken from the initiation regions of fracture, unless otherwise stated.

Figure 4.1 shows an example of crazes in styrene-based polymers, taken from bulk and solution-cast thin film[58] specimens, and examined under TEM. The loading direction is perpendicular to the craze. Interestingly, most failure begins when a void generates in the craze, followed by the propagation of the craze, until the final fracture. Figure 4.2 shows the regions of initiation and fast fracture.

Factors that are known to affect the polymer resistance to deformation are molecular weight, composition, molecular orientation, entanglement density, etc. In this work, attention is primarily focused on the influence of the following three variables; acrylonitrile (AN) content, molecular weight (M_w), and straining rate.

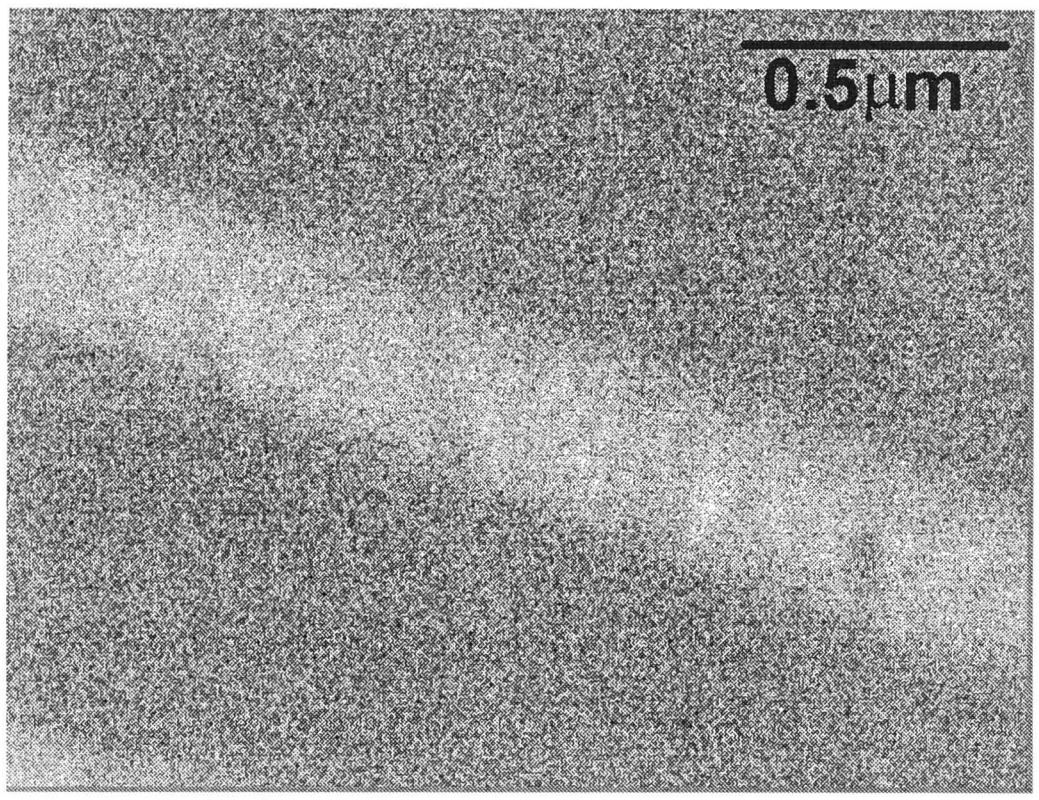

(a)

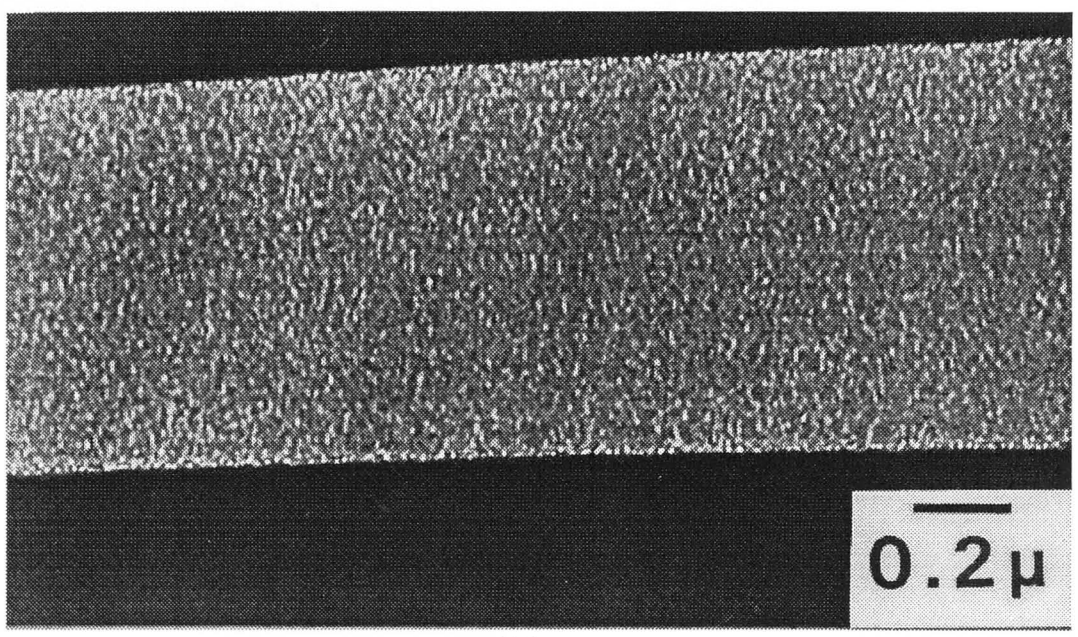

(b)

Figure 4. 1: Transmission electron micrographs of a region near the centre of the craze, showing a characteristic craze/polymer boundary. (a) craze from SAN bulk specimen under monotonic loading; (b) craze from PS thin film showing the distinctive midrib (courtesy of Jar[58])

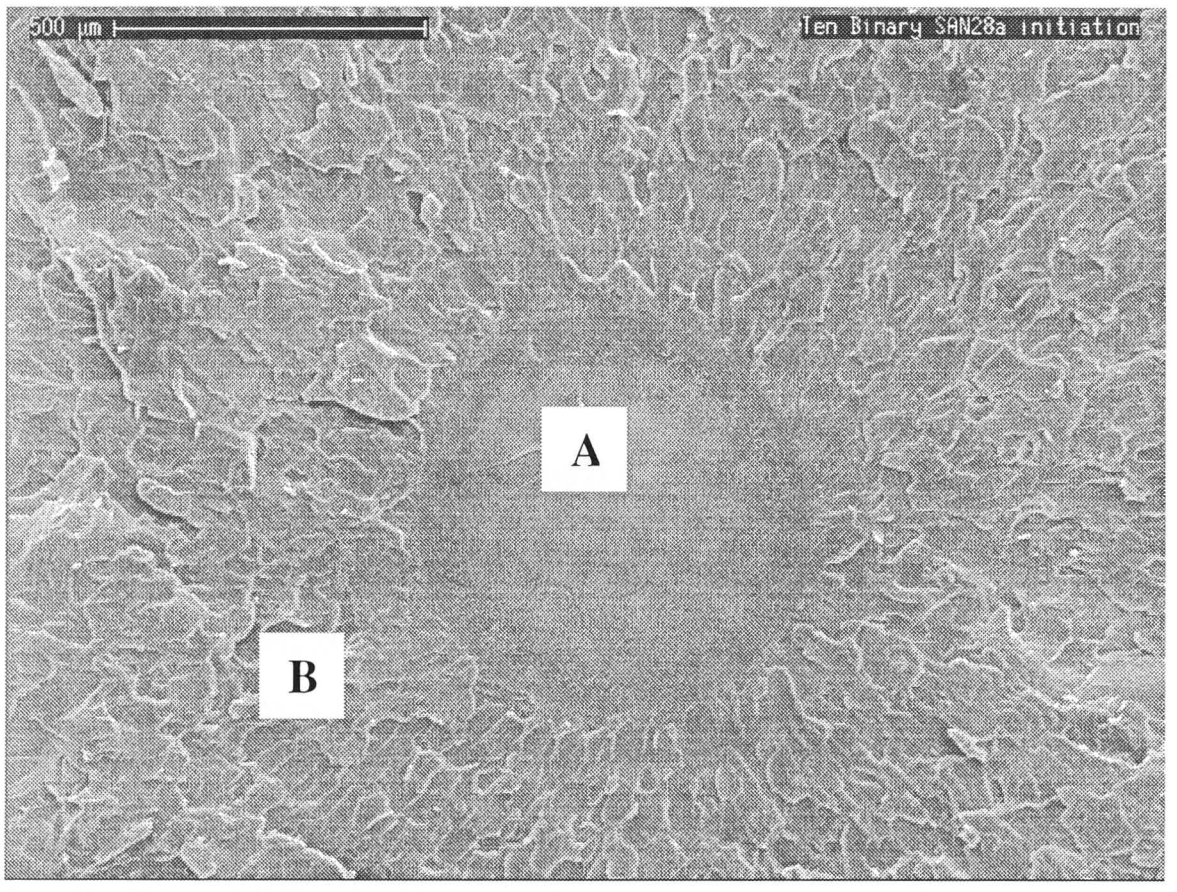

Figure 4. 2: Scanning electron micrograph showing the difference between initiation region (labeled A) and fast propagation region (labeled B) of a simple tensile specimen

It has been reported[30, 59, 60] that AN content in SAN can have an appreciable effect on the material properties. It will be shown in later sections of this work that by increasing the AN content, mechanical properties of SAN are improved significantly. M_w can also have significant effects on material properties. Although the effect of M_w has been minimised by proper material selection, SAN24, with a considerable higher M_w than the other SANs clearly shows the high M_w effect.

The last variable to look at is the straining rate. Different straining rates were achieved by different mechanical tests. These tests show that different straining rates cause different deformation behaviours.

4.2 Mechanical test results and deformation behaviours

Mechanical properties of SAN copolymers and SMI/SAN blends, that vary in acrylonitrile (AN) content from 23.4 to 28.9 wt%, were obtained from simple tensile, single-edge-notched (SEN) tensile and Izod impact tests. The tested specimens were then analysed by electron microscopy. The following sections present the observations of the deformation mechanisms and the mechanical properties. Discussions of these results are presented at the end of this chapter.

For simplicity, SAN copolymers are termed pure SANs and SMI/SAN blends as binary blends. The examinations of the fracture mechanics were performed only on materials containing SAN22 and SAN28a, because the materials with SAN22 and SAN28a constituents show the poorest and best mechanical properties, respectively.

4.2.1 Simple tensile test

Results obtained from the simple tensile test are plotted as a function of AN content in Figure 4.3. The fracture energy increases constantly with AN content, except in the case of SAN24 and SMI/SAN24, which have a high molecular weight. Compared to pure SANs, the fracture energy for the binary blends decreases because of the addition of SMI. In the binary blends, the gradient of the fracture energy trend also reduces with AN content.

There are two stages of fracture during crack development under constant loading; stable crack growth and fast crack growth. A crack is usually generated at the interfaces of impurities or artifacts in the polymer. The crack propagates stably in the initiation region until it is too large to maintain the stability. At this point, fast

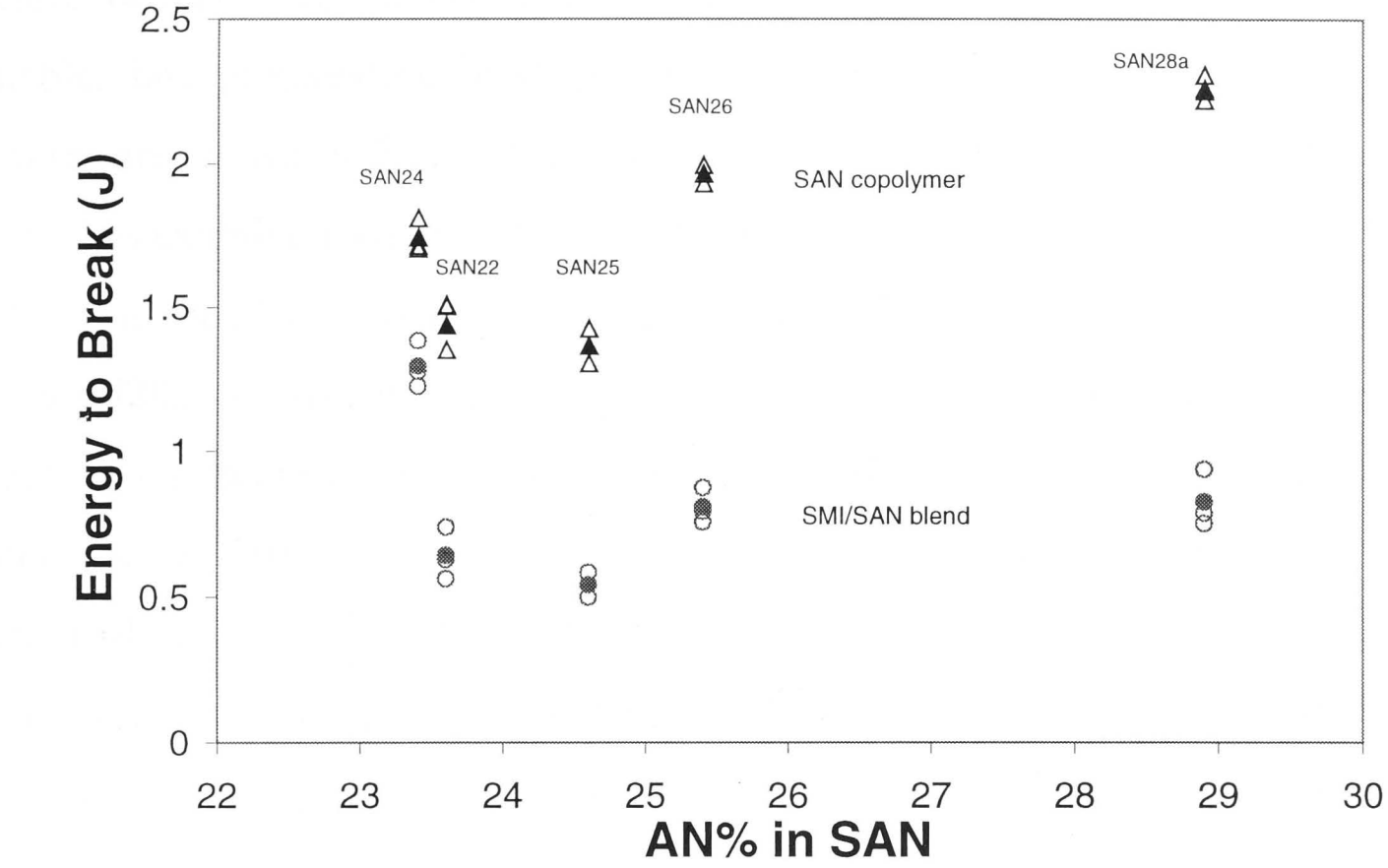

(a)

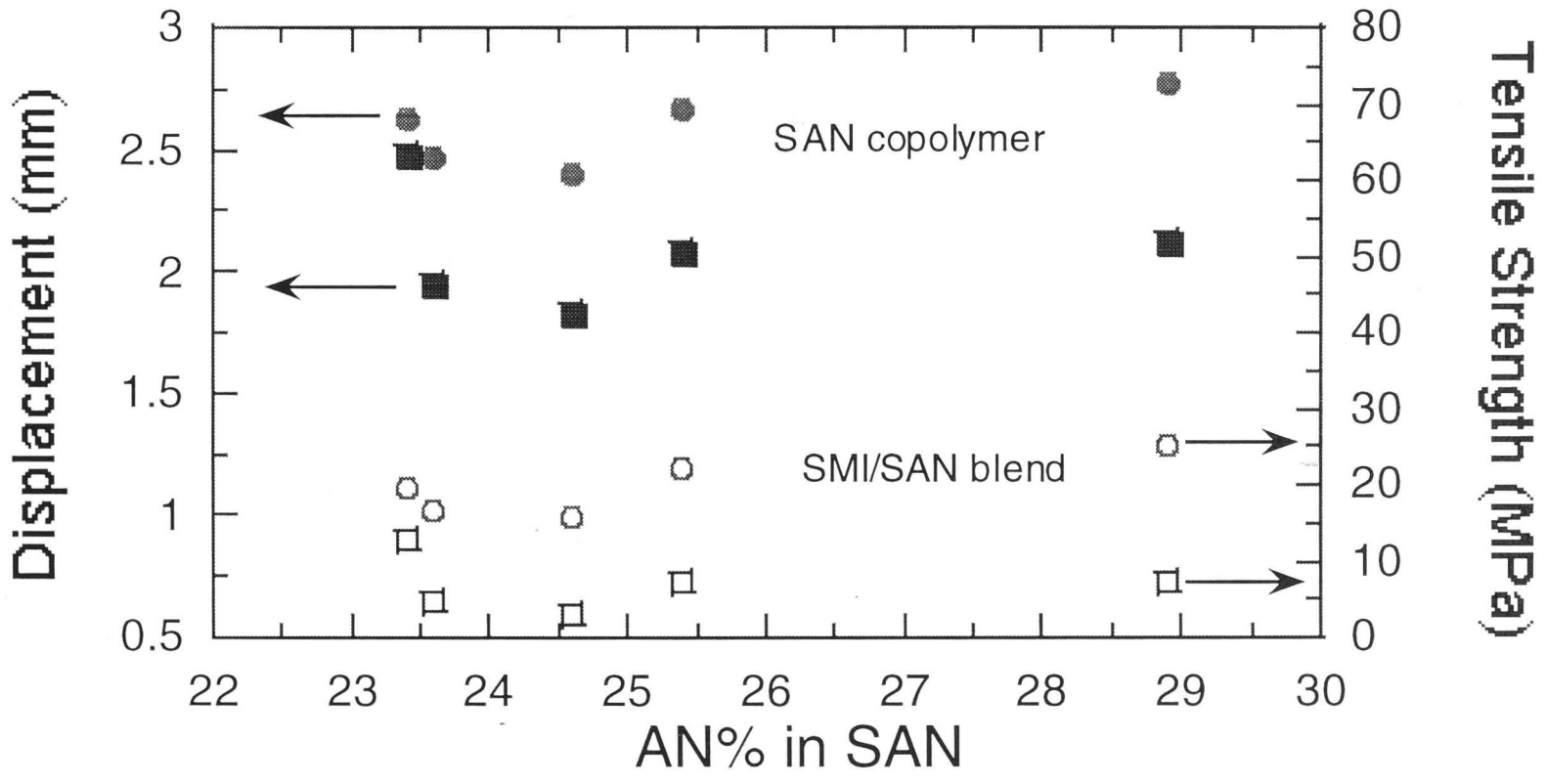

(b)

Figure 4. 3: Simple tensile results vs. acrylonitrile (AN) content of SAN copolymer and SMI/SAN blend. (a) tensile energy to break vs. AN content in SAN (solid points represent the average value whereas open points represent individual data point); and (b) tensile strength and displacement vs. AN content in SAN (solid points represent the tensile strength and open points represent the displacement)

fracture occurs. The stable crack propagation results in mirror craters, and the unstable, fast propagation mode results in rough surfaces. These two modes of fractures are shown in Figure 4.2. However, only the deformation from the initiation region was examined using electron microscopy, unless otherwise stated.

It is seen by the naked eye that pure SAN22 has smaller initiation regions than pure SAN28a. A typical SEM comparison of the two surfaces is shown in Figure 4.4. Higher magnification of the initiation region shown in Figure 4.5 indicates that patches were formed on the fracture surfaces. Small patches are abundantly distributed in SAN22 but fewer and larger ones are in SAN28a. A close up observation of a patch in Figure 4.5(c), shows fibril structure around the patch edges.

Figure 4.6 shows TEM micrographs of pure SANs (see Figures 4.6(a)-(b)) and binary blends (see Figures 4.6(c)-(d)) containing SAN22 or SAN28a. Fibril bundles are seen on all surfaces, indicating that the materials fail through pre-existing craze planes. Multiple crazing is present underneath the fracture surface of pure SAN22 but not pure SAN28a. In binary systems, blends with SAN22 show more crazes compared to those with SAN28a.

In Figure 4.7, TEM micrographs show fast fractured regions of pure SAN22 and SAN28a. The deformation observed is similar to that in the initiation region. That is, multiple crazing is observed in pure SAN22 but not in pure SAN28a.

Other deformations observed are large crazes, named micro-cracks, which were generated in the gauge section of pure SAN specimen, as shown in Figure 4.8. The extent to which micro-cracks are formed was found to be independent of material type. The same materials, in Figures 4.8(a)-(b), and Figures 4.8(c)-(d) show different number of micro-cracks formed on each specimen.

4.2.2 Single-edge-notched tensile test

The single-edge-notched (SEN) tensile test is used to determine the stress intensity factor (K_I) of crack initiation at the pre-crack. The K_I values for both pure SAN and binary blends are plotted in Figure 4.9. The figure shows K_I values to increase with AN content in SAN.

Observations underneath the fracture surfaces using TEM reveal different fracture behaviour to that produced by the simple tensile test. Multiple crazes are seen in SEN specimens, as shown in Figure 4.10. However, the micrographs also illustrate a general similarity in the failure mechanism of the SEN specimens, to those

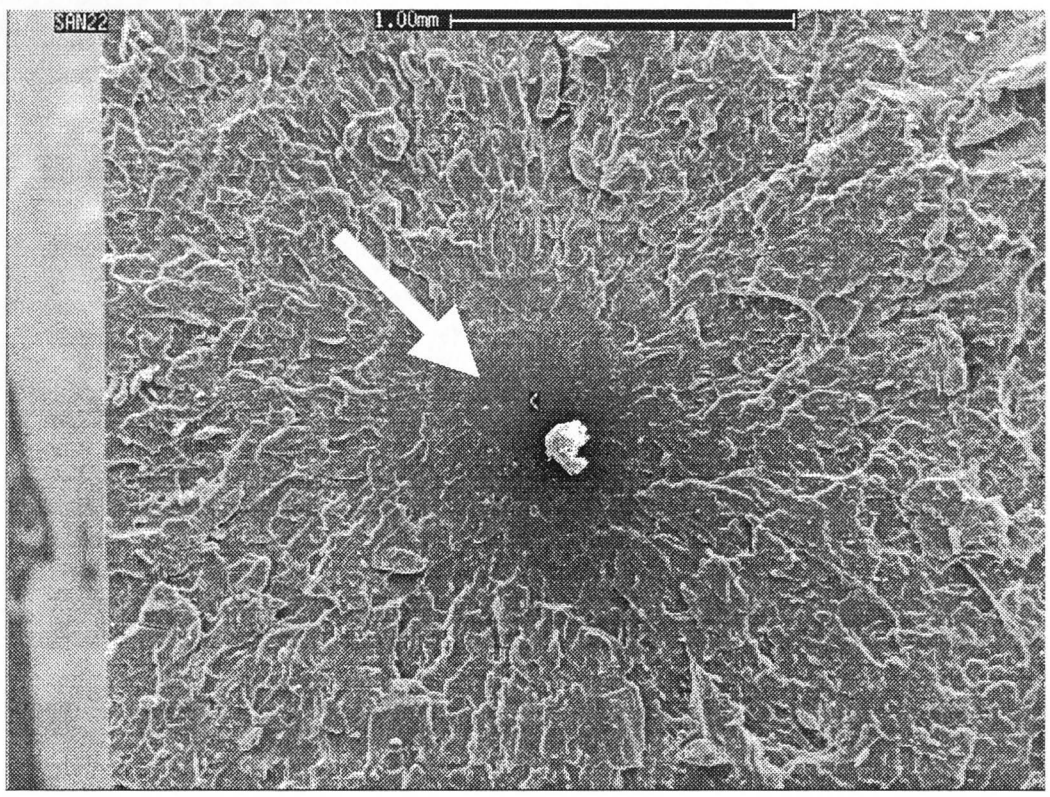

(a)

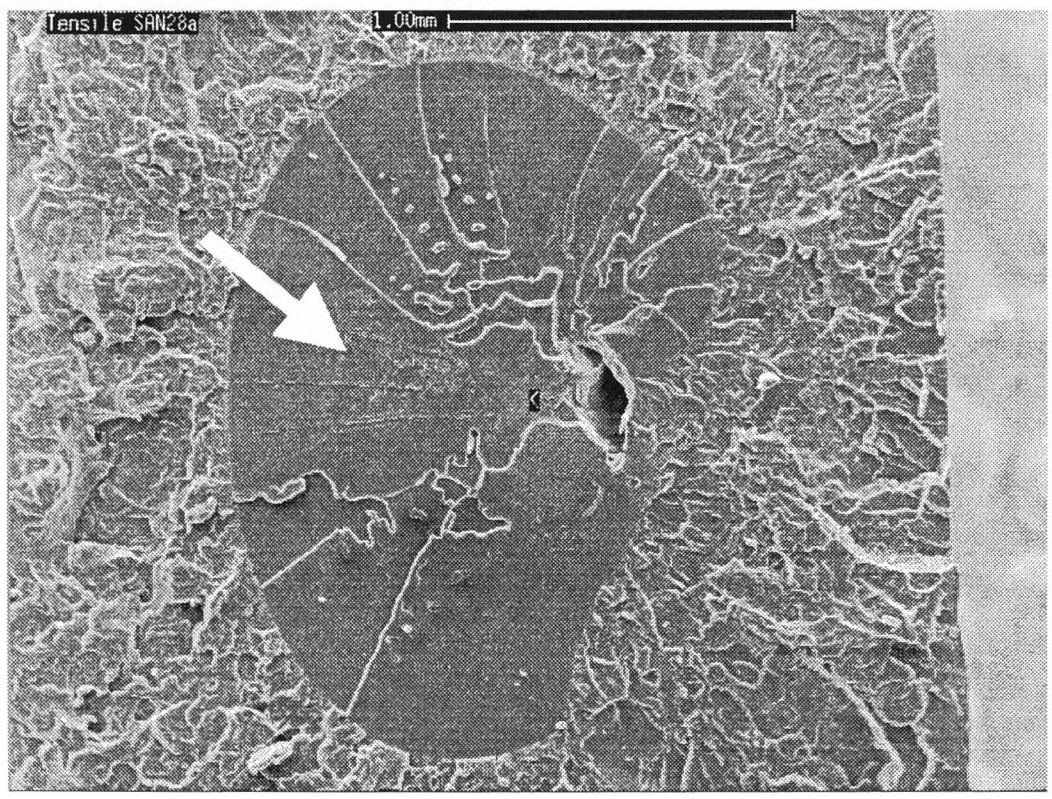

(b)

Figure 4. 4: Scanning electron micrographs of simple tensile fracture surfaces of SAN copolymers. The smooth surface (arrowed) is the initiation region whereas the rough surface represents fast propagation of crack. (a) SAN22 copolymer; and (b) SAN28a copolymer

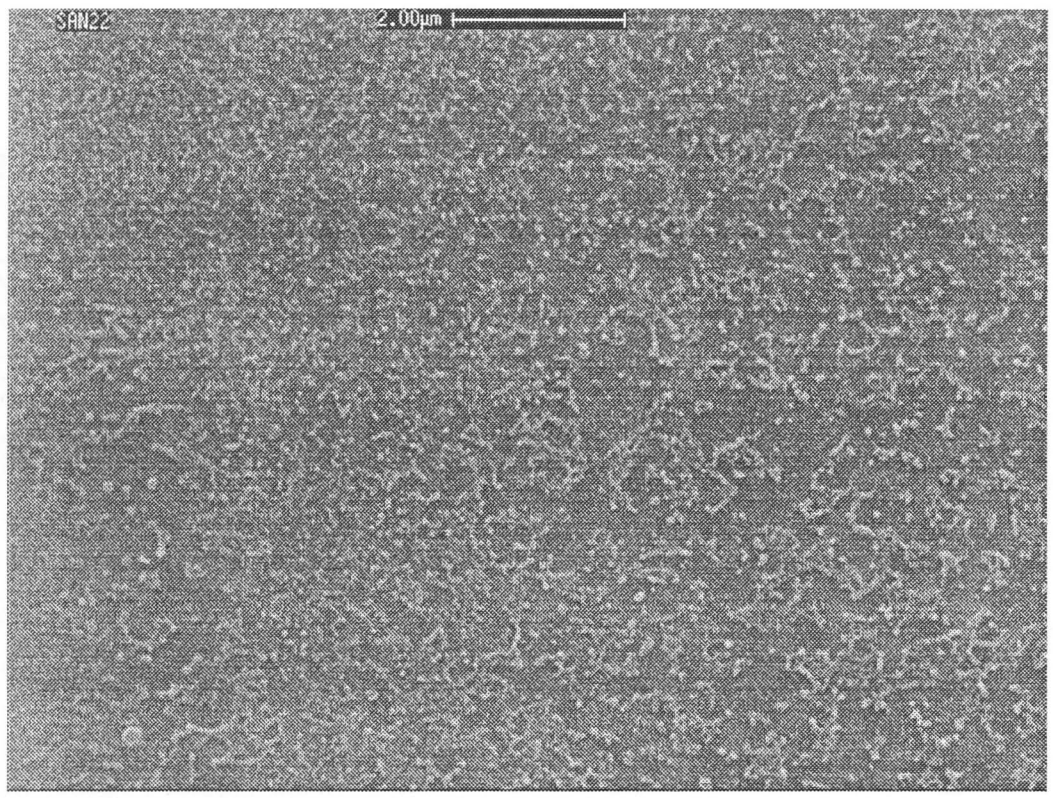

(a)

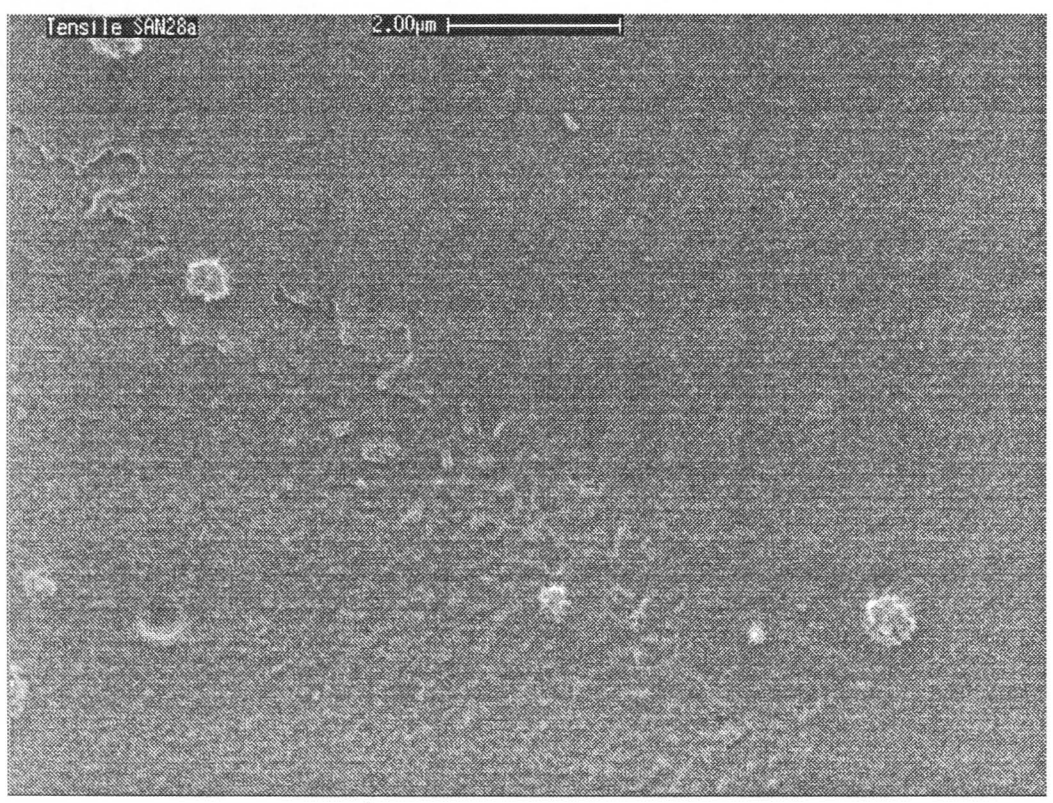

(b)

Figure 4. 5: Scanning electron micrographs of simple tensile specimen under higher magnification. (a) multiple small and tiny patches in SAN22; (b) fewer, larger patches in SAN28a; and

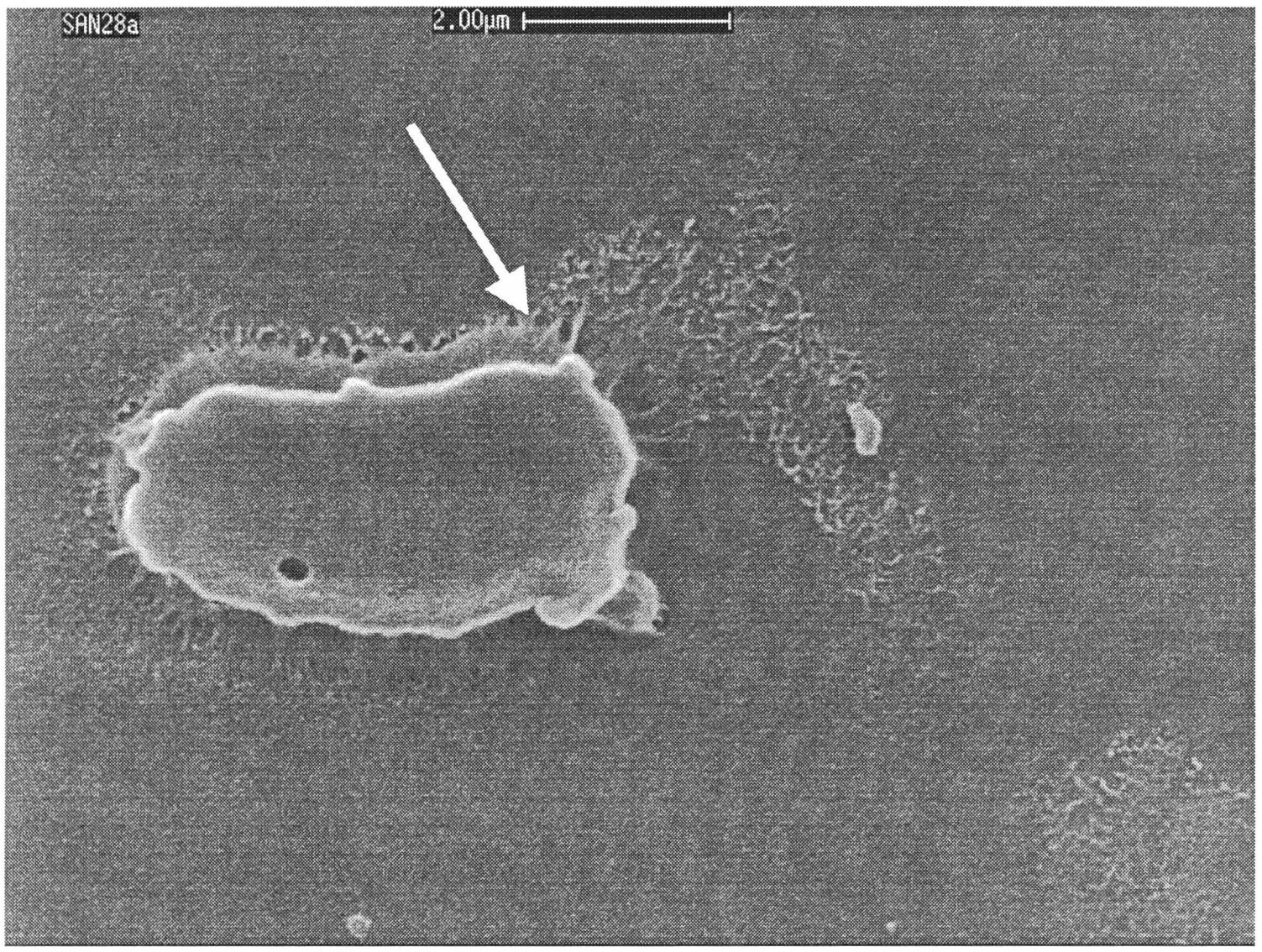

(c)

Figure 4. 5: (c) morphology of a patch, showing the fibril structure around the edges and fibril failure (arrowed)

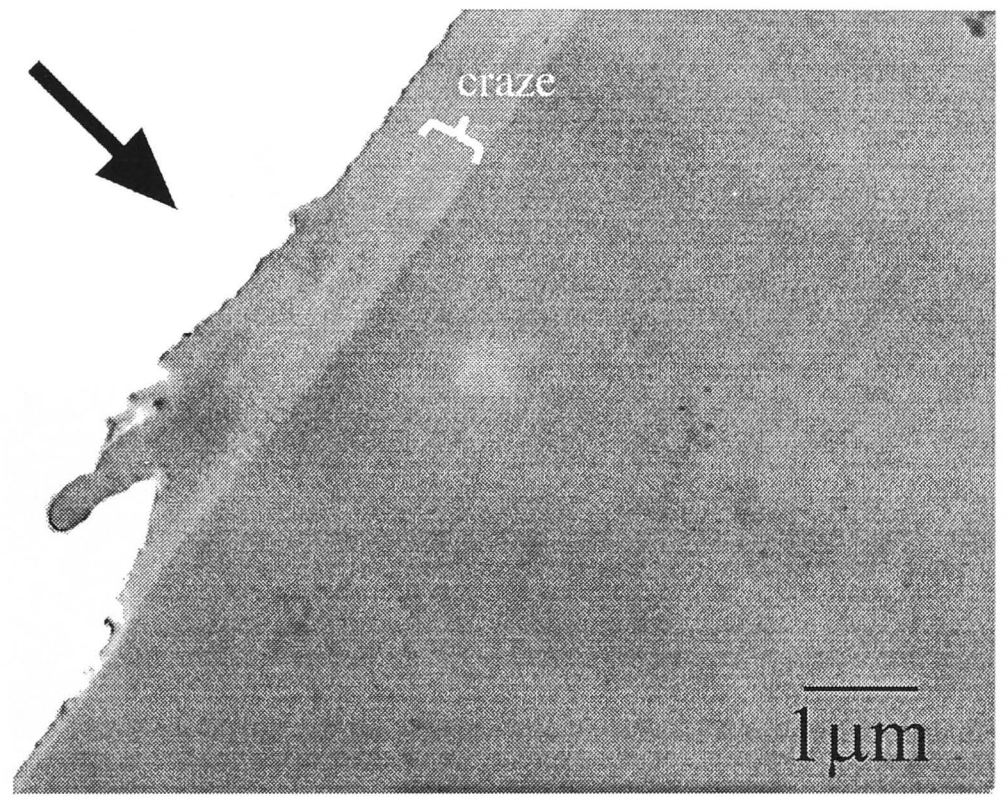

(a)

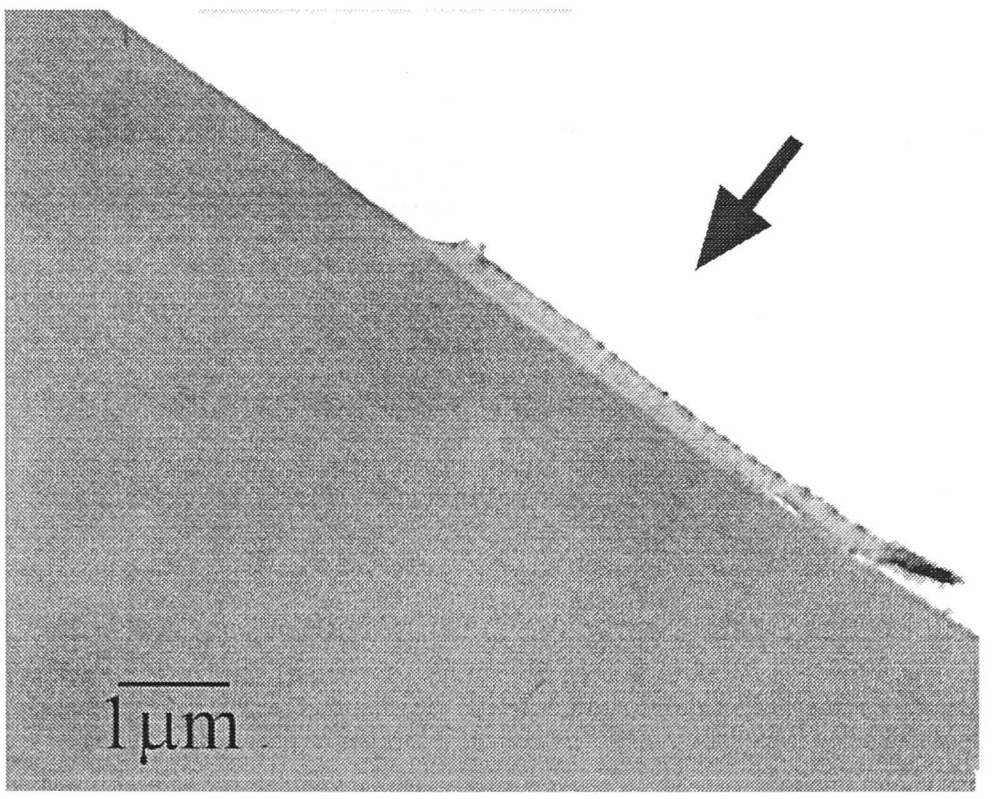

(b)

Figure 4. 6: Transmission electron micrographs of simple tensile specimens at initiation region. Arrow indicates the fractured surface. (a) SAN22 copolymer; (b) SAN28a copolymer;

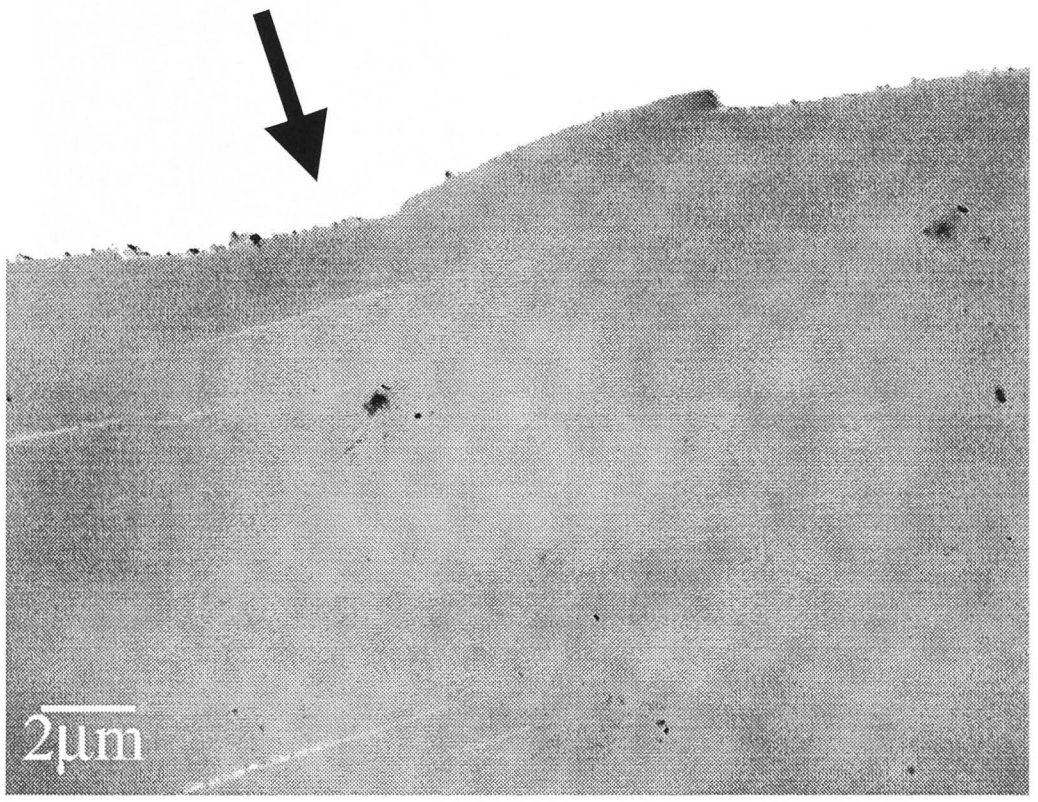

(c)

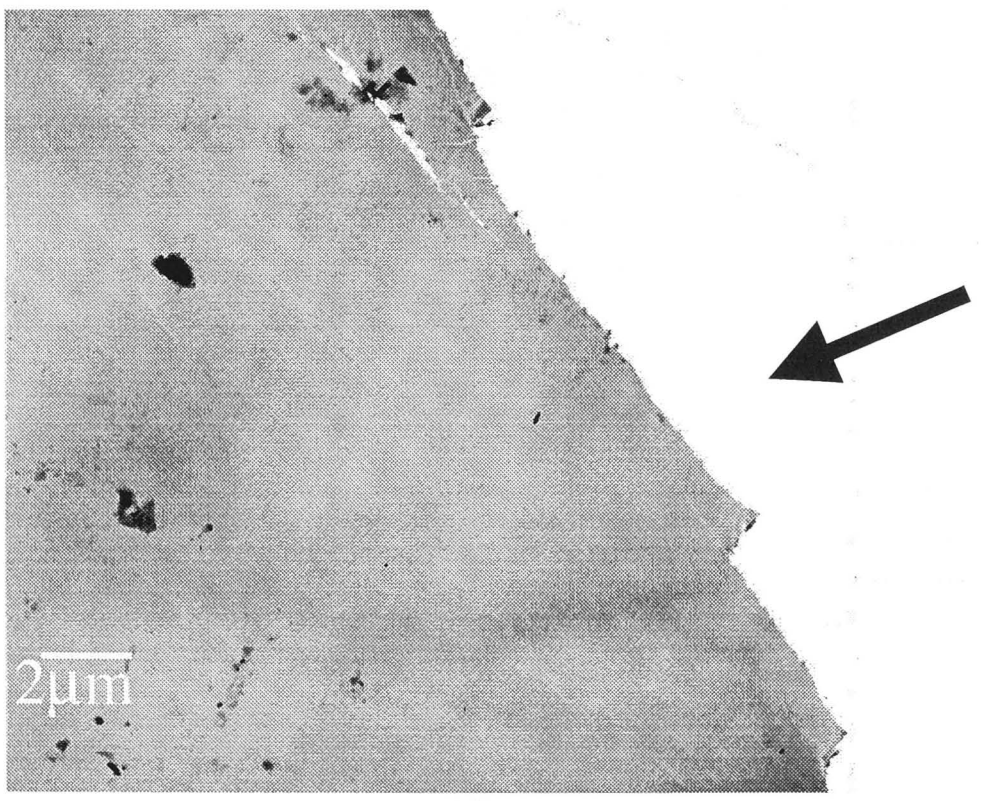

(d)

Figure 4. 6: (c) SMI/SAN22 blend; and (d) SMI/SAN28a blend

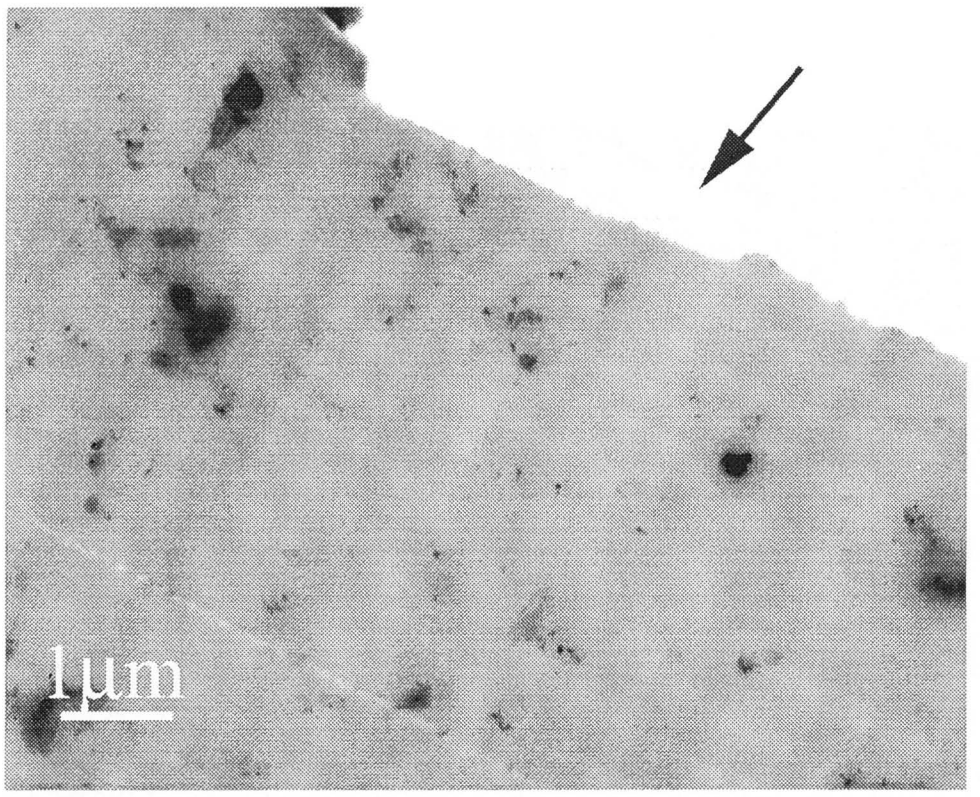

(a)

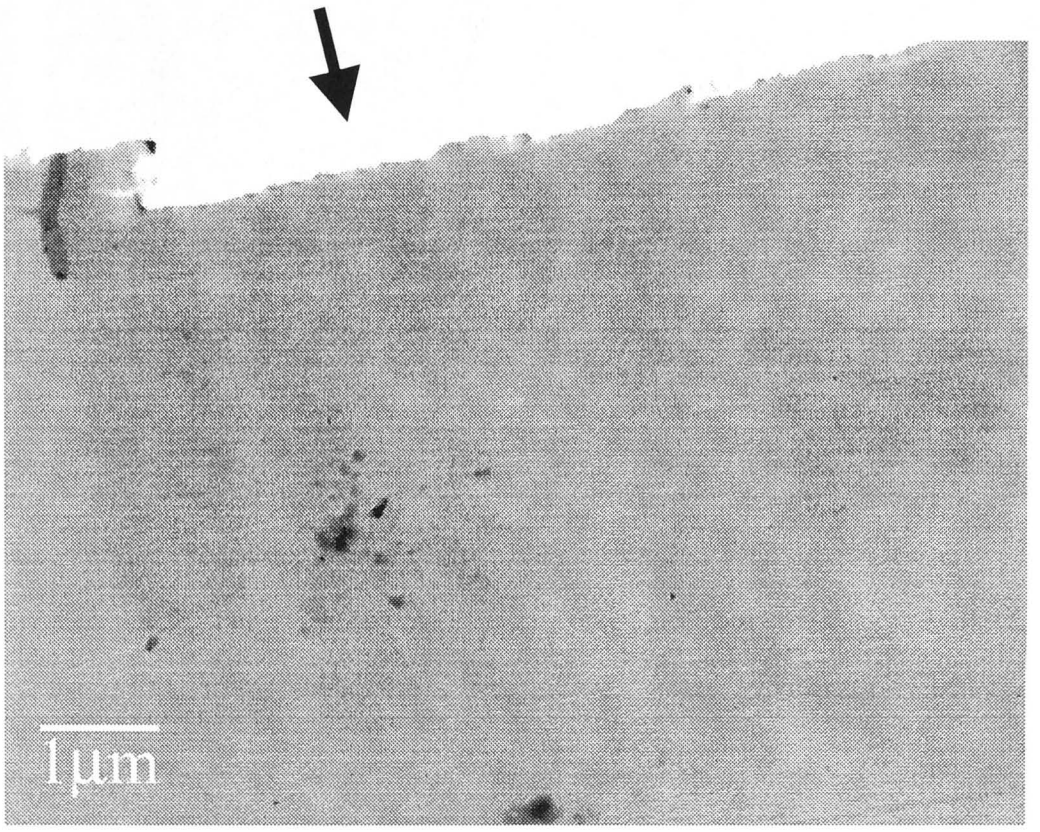

(b)

Figure 4. 7: Transmission electron micrographs of fast fracture region. (a) SAN22 copolymer; and (b) SAN28a copolymer

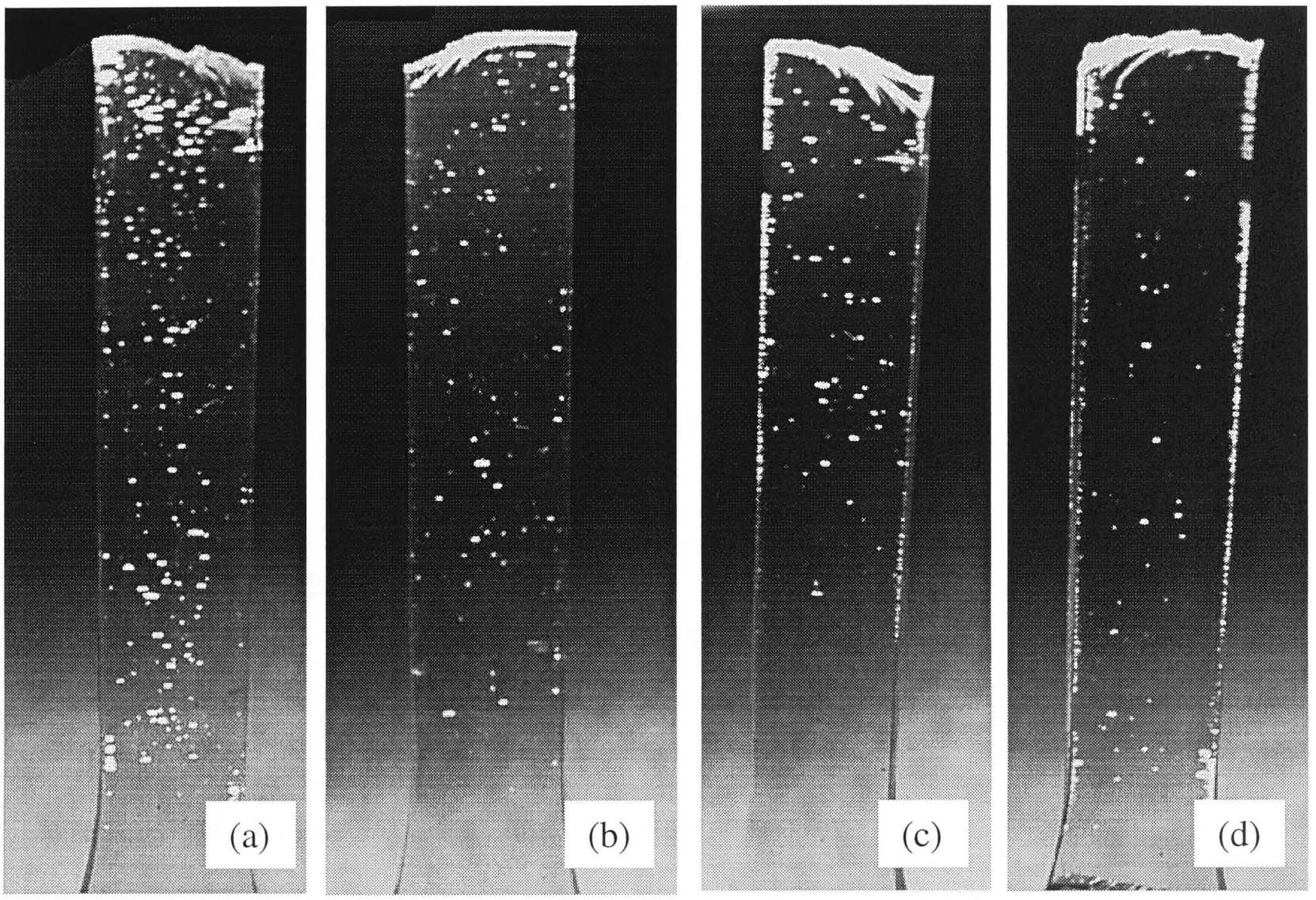

Figure 4. 8: Micro-cracks or large crazes in SAN copolymers. (a), (b) SAN24 copolymer; and (c), (d) SAN28a copolymer

specimens in a simple tensile test. The similarity is that fibril bundles are observed on all fracture surfaces.

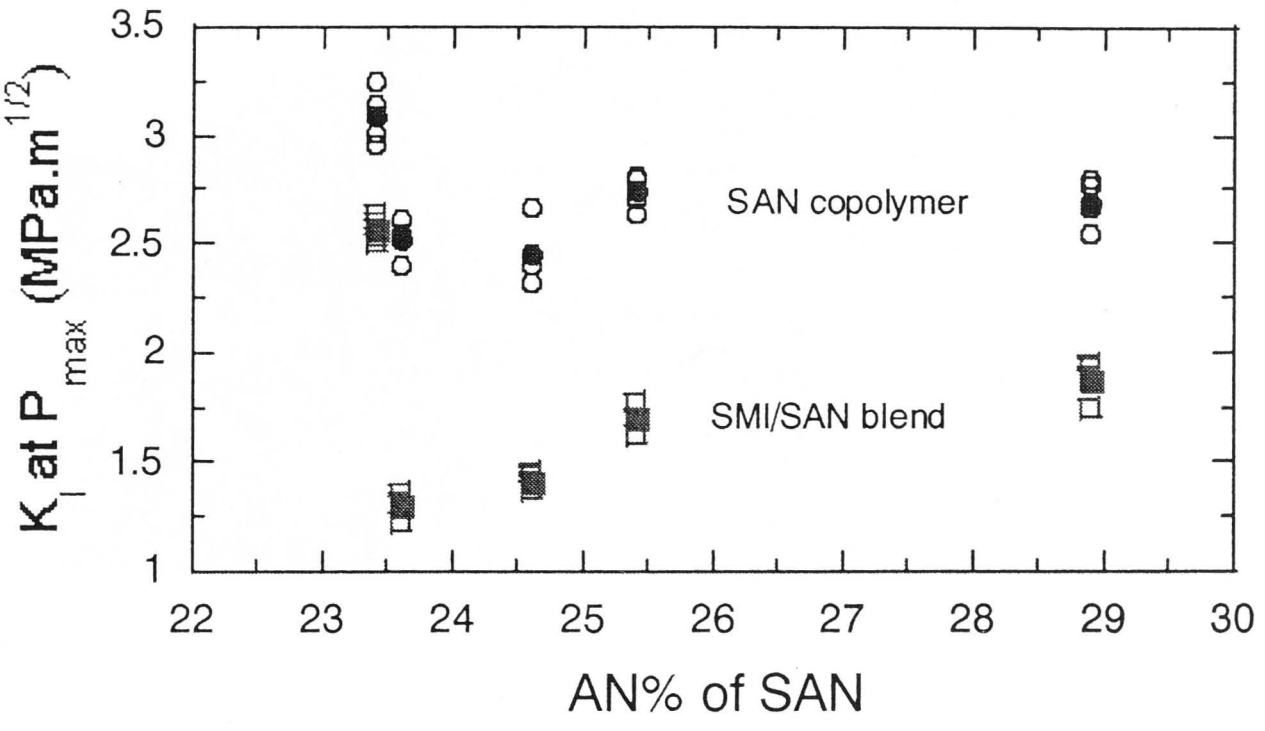

Figure 4. 9: Variation of stress intensity factor (K_I) vs. acrylonitrile (AN) content for SAN copolymer and SMI/SAN blend (solid points represent the average value whereas open points represent individual data point)

Morphologies observed using SEM show river-flow patterns at the initiation region of pure SAN. The SEM micrographs shown in Figure 4.11, indicate that there is a difference in fracture surface morphology compared to that of simple tensile test in Figure 4.5.

4.2.3 Izod impact

The use of instrumented Izod impact enables the total fracture energy, crack initiation energy and crack propagation energy to be obtained. The latter two energies represent the two stages of crack growth: firstly, the crack from the notch progressed steadily in the initiation region; and secondly, the crack accelerated beyond the initiation region, causing a catastrophic fracture. The sum of both crack initiation energy and crack propagation energy gives the total fracture energy of the material.

The total fracture energy, shown in Figure 4.12, shows that AN content is relatively insensitive to the Izod impact test. All three energy-absorption elements do not show much variation in impact toughness as a result of AN content.

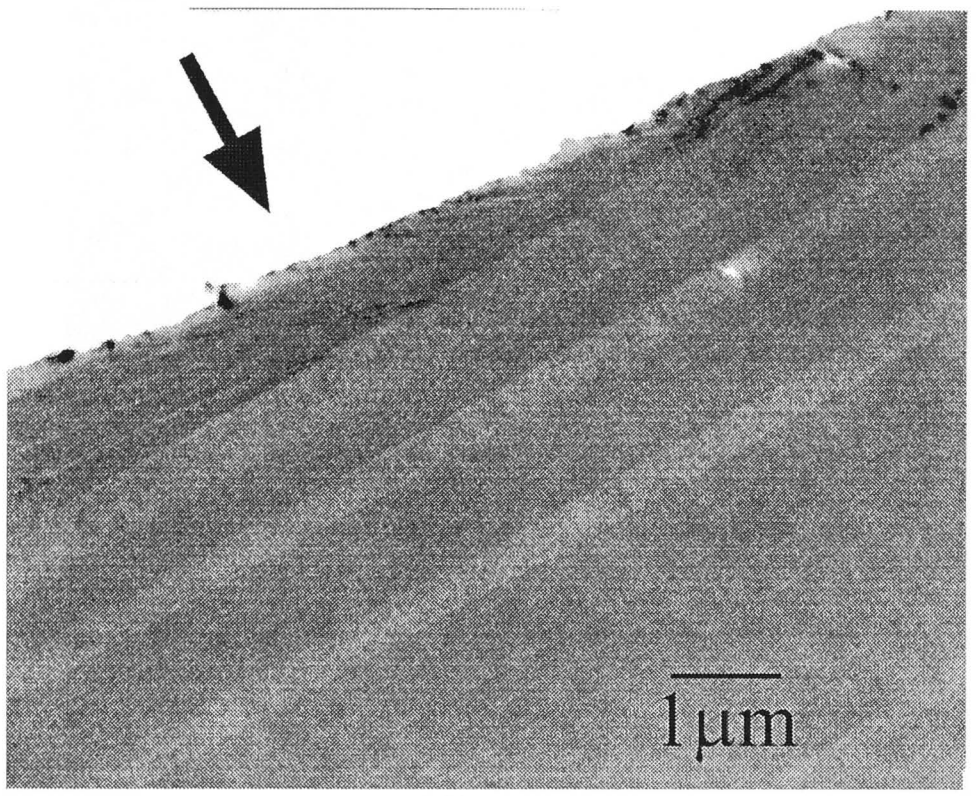

(a)

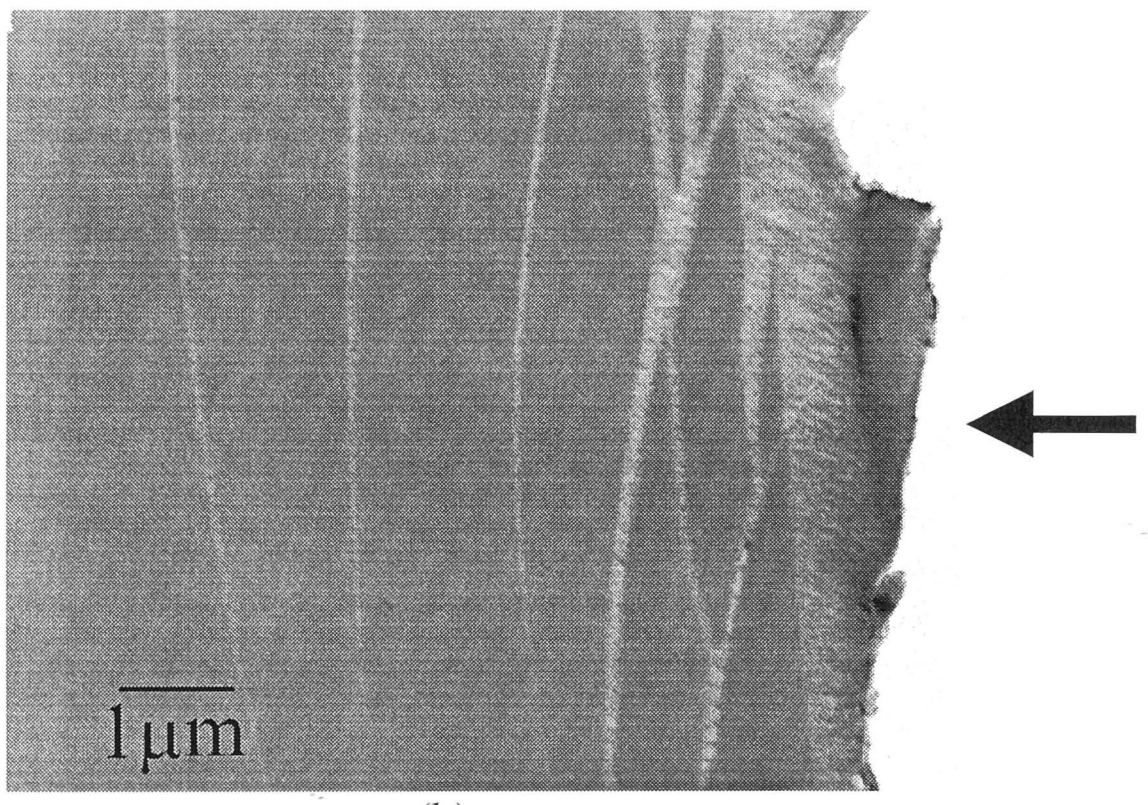

(b)

Figure 4. 10: Transmission electron micrographs of single-edge-notched specimen from initiation region. Arrow indicates the fractured surface. (a) SAN22 copolymer; (b) SAN28a copolymer;

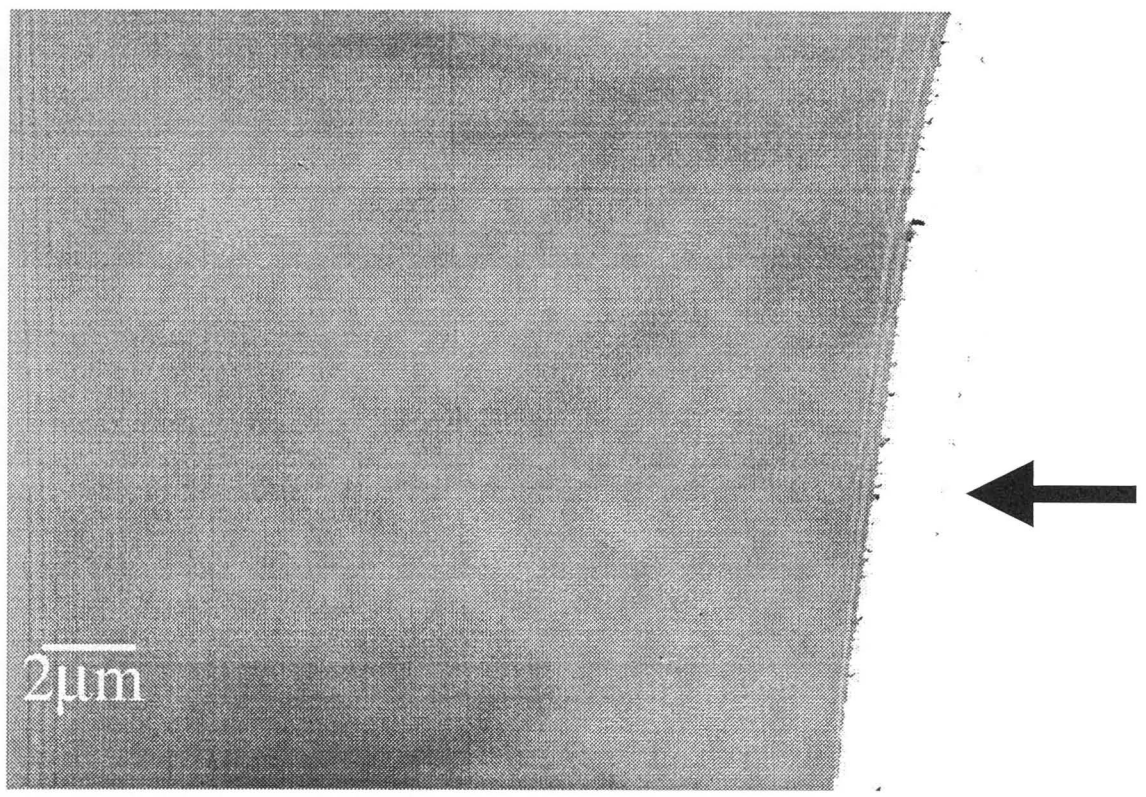

(c)

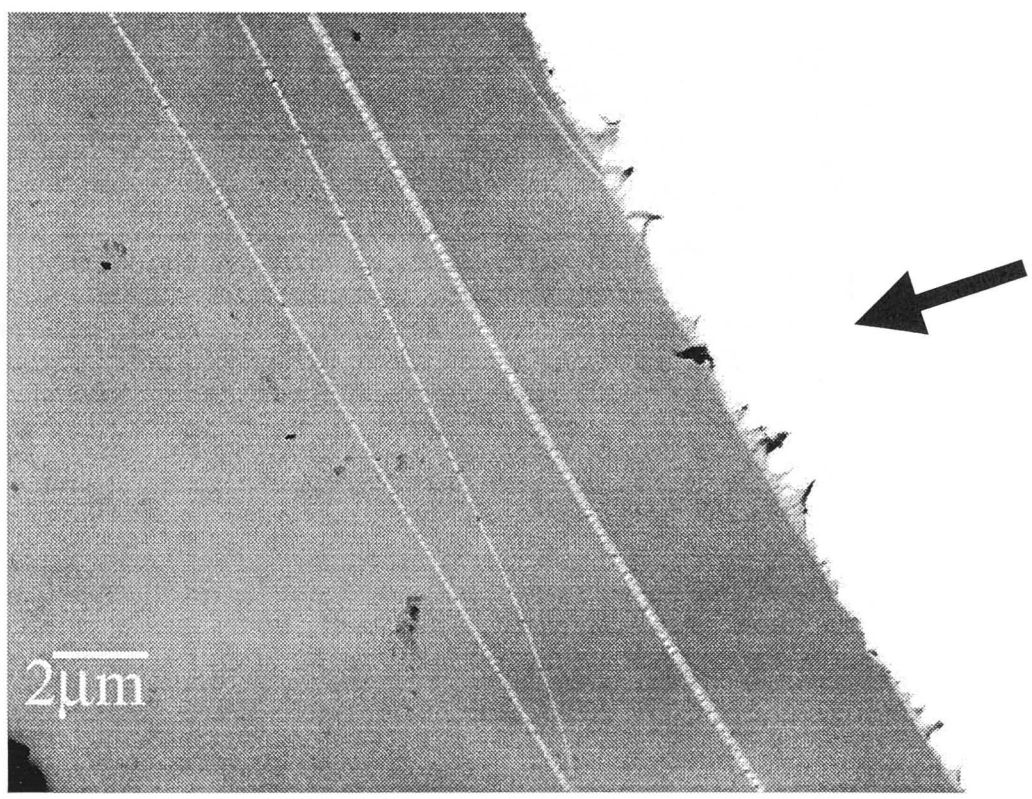

(d)

Figure 4. 10: (c) SMI/SAN22 blend; and (d) SMI/SAN28a blend

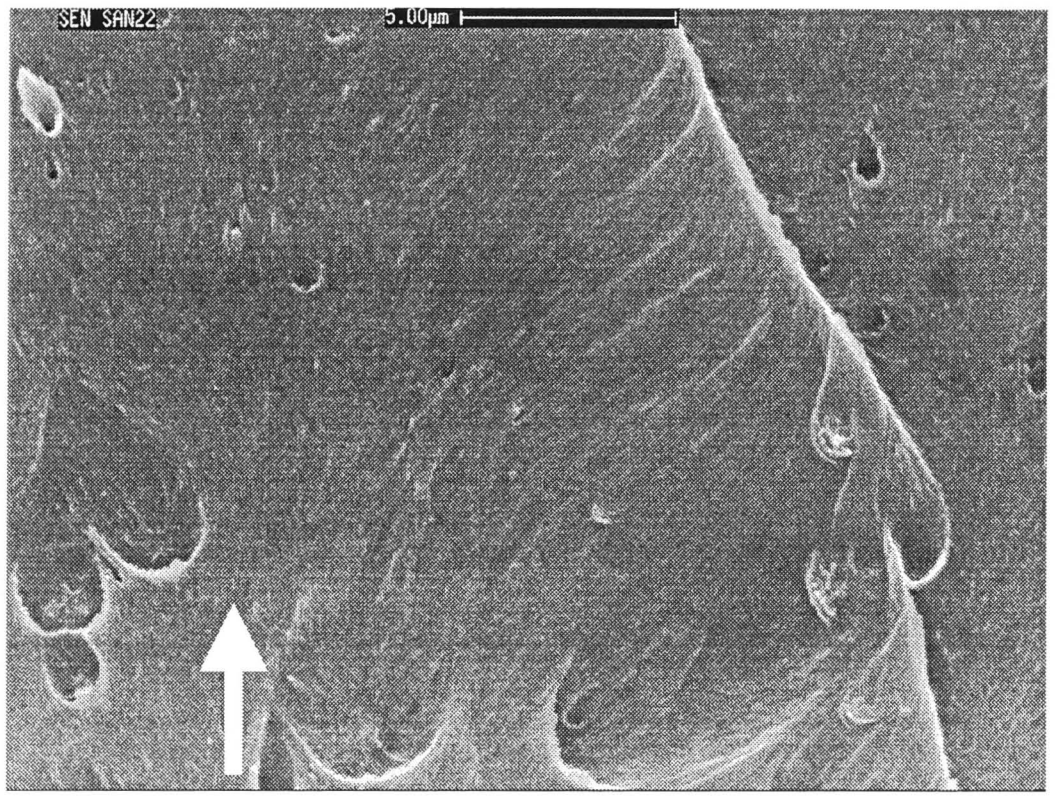

(a)

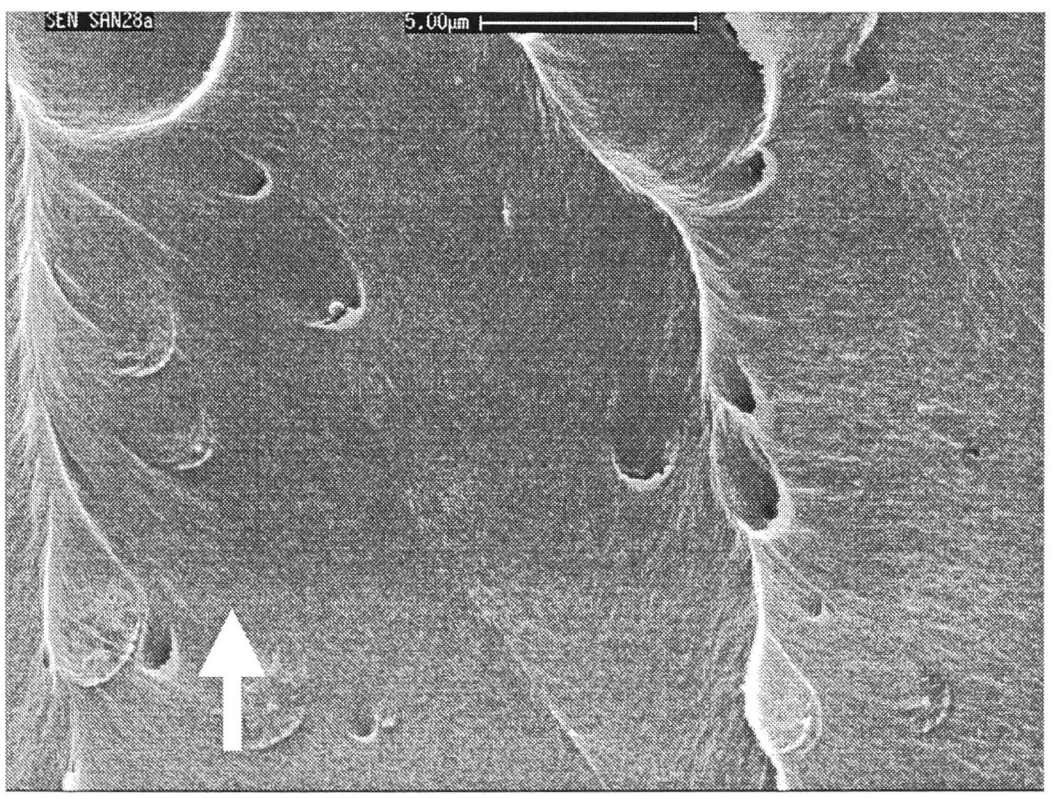

(b)

Figure 4. 11: Scanning electron micrographs of single-edge-notched specimen at the initiation region. Arrows indicate the direction of fracture. (a) SAN22 copolymer; and (b) SAN28a copolymer

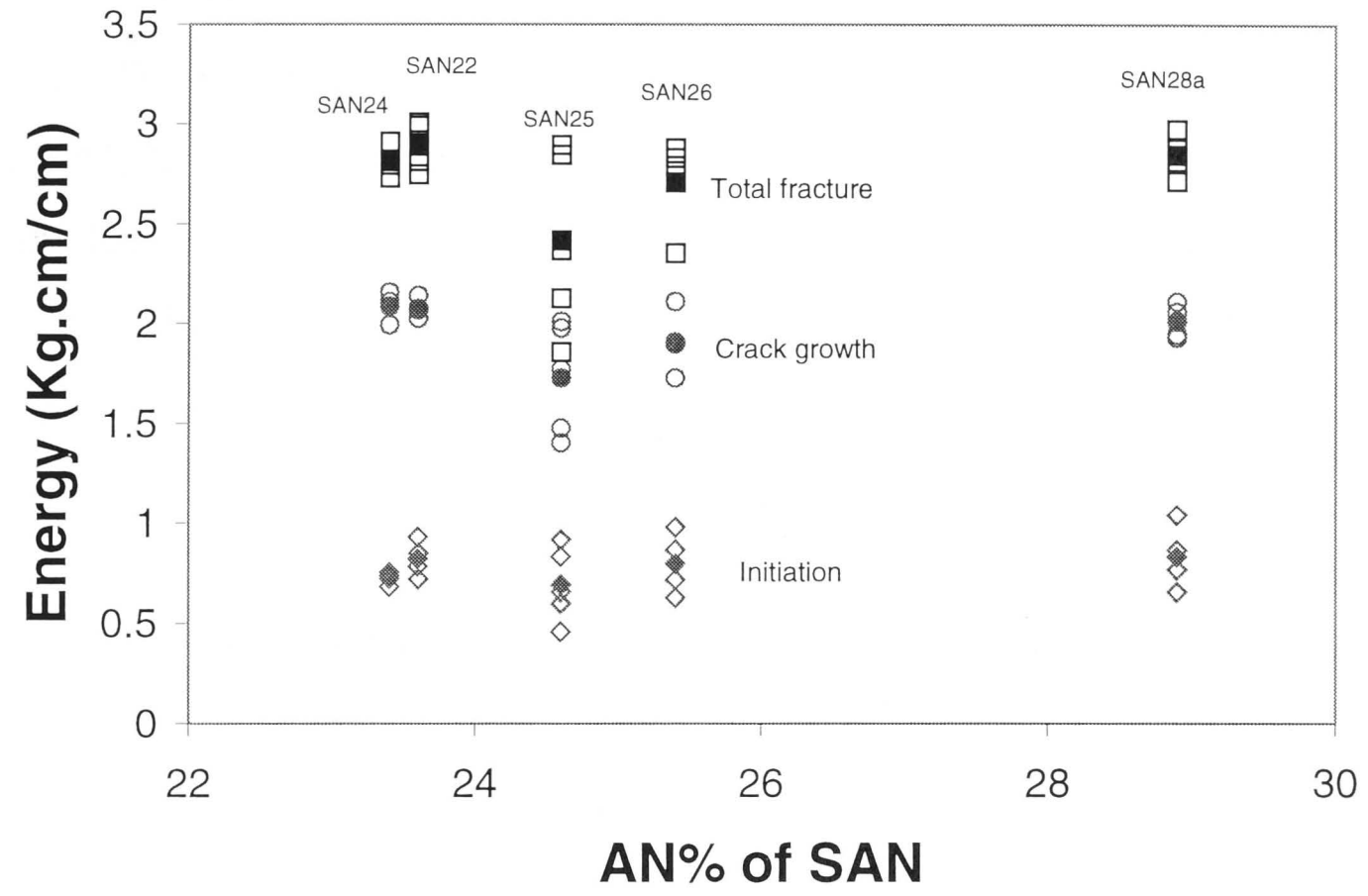

(a)

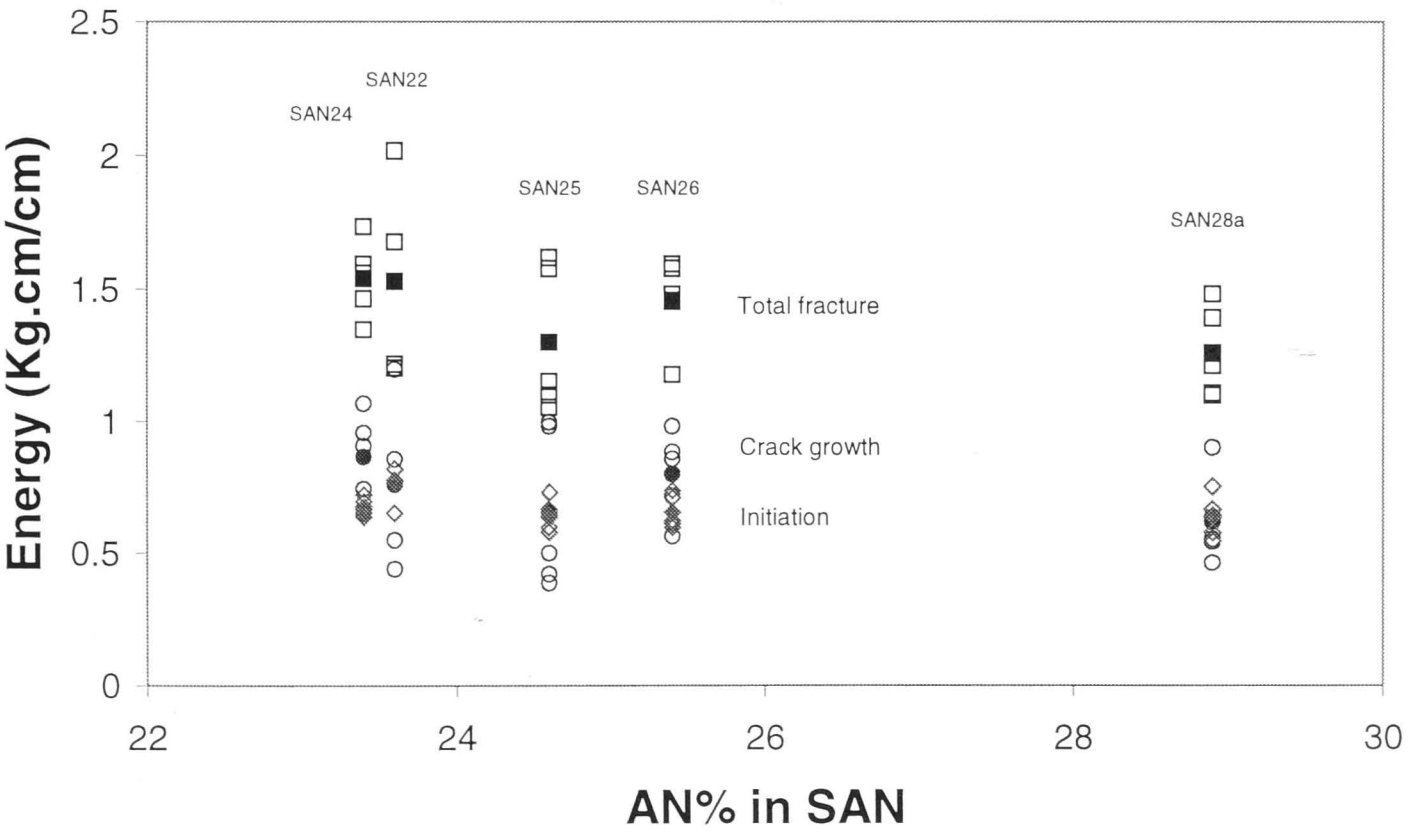

(b)

Figure 4. 12: Mechanical results of Izod impact specimens vs. acrylonitrile (AN) content. (a) impact energy for SAN copolymer; and (b) impact energy for SMI/SAN blend

The Izod fracture surface morphologies of pure SAN differ from those of tensile tests, as seen in Figure 4.3 and Figure 4.9. The fracture morphologies of Izod impact, shown in Figure 4.13, show material pull-out to form whiskers at the initiation region. The whiskers are in the direction of the fracture. The whiskers formed in pure SAN22 are not as ductile as are those in SAN28a. Further examination of the morphologies in TEM micrographs reveals multiple crazing underneath the fracture surfaces of both pure SAN and binary blends (see Figure 4.14). Observation of the fracture surfaces shows failure by crazing, which is also observed in other mechanical tests.

4.3 Mechanisms affecting mechanical properties

This section looks at the intrinsic factors affecting the mechanical trends in the three tests. One of the crucial factors observed in the previous sections, is the effect of AN content in SAN. This effect is well documented as a critical material toughening mechanism[30, 59].

The other factor that affects the mechanical properties, is molecular weight (M_w). However, in this study, materials were chosen so that the M_w remained the same and did not contribute to the toughening effect being studied, with the exception of SAN24, which has a higher M_w than the others. Full details of the materials used can be found in Tables 2.3 - 2.6.

4.3.1 Acrylonitrile (AN) content effect

Simple tensile and SEN tensile results in Figure 4.3 and Figure 4.9, respectively, show an increase in the materials strength and crack resistance with AN content. This work relates to the work of Quintens et al.[60], who demonstrated the effects of the AN content of SAN on tensile properties. Quintens et al. also proved that optimal strength of the material is reached at 24 wt% AN for PC/SAN blends. A further increase in AN content would result in a decrease in the mechanical properties of PC/SAN.

To understand the physical behaviours of these materials, SANs of both a low (SAN22) and high (SAN28a) AN content were examined by electron microscopy.

Stability of initial craze growth under simple tensile test is indicated by size of the initiation zone. As shown in Figure 4.4, crazes in SAN28a are more stable than those in SAN22. The stability of the craze is again illustrated in Figure 4.5 and Figure

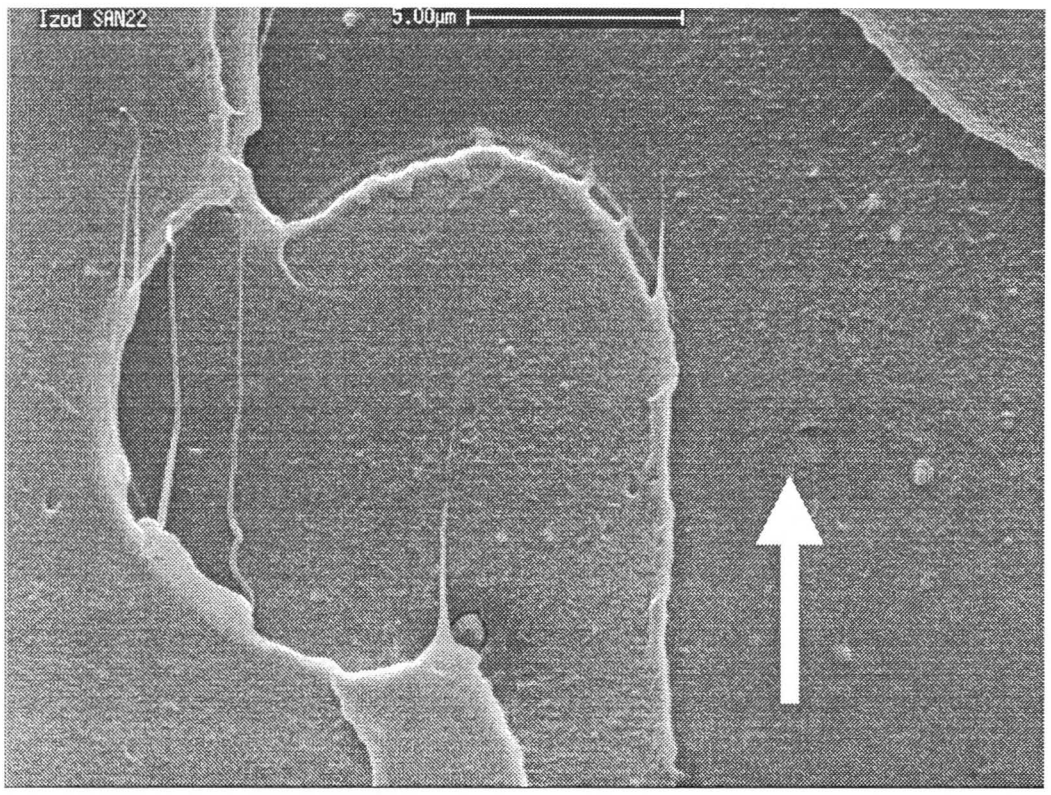

(a)

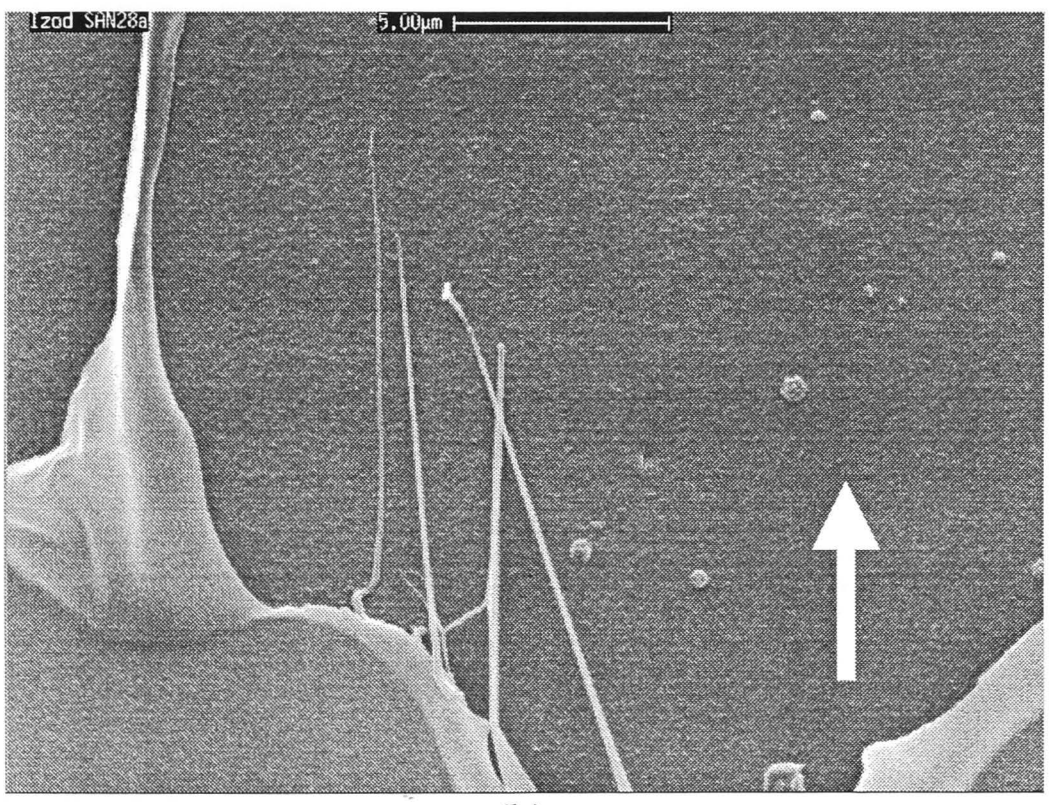

(b)

Figure 4. 13: Scanning electron microscopy of Izod impact fracture surfaces. Arrows indicate the direction of fracture. Specimens were taken from the clamped fractured pieces. (a) SAN22 specimen; and (b) SAN28a specimen;

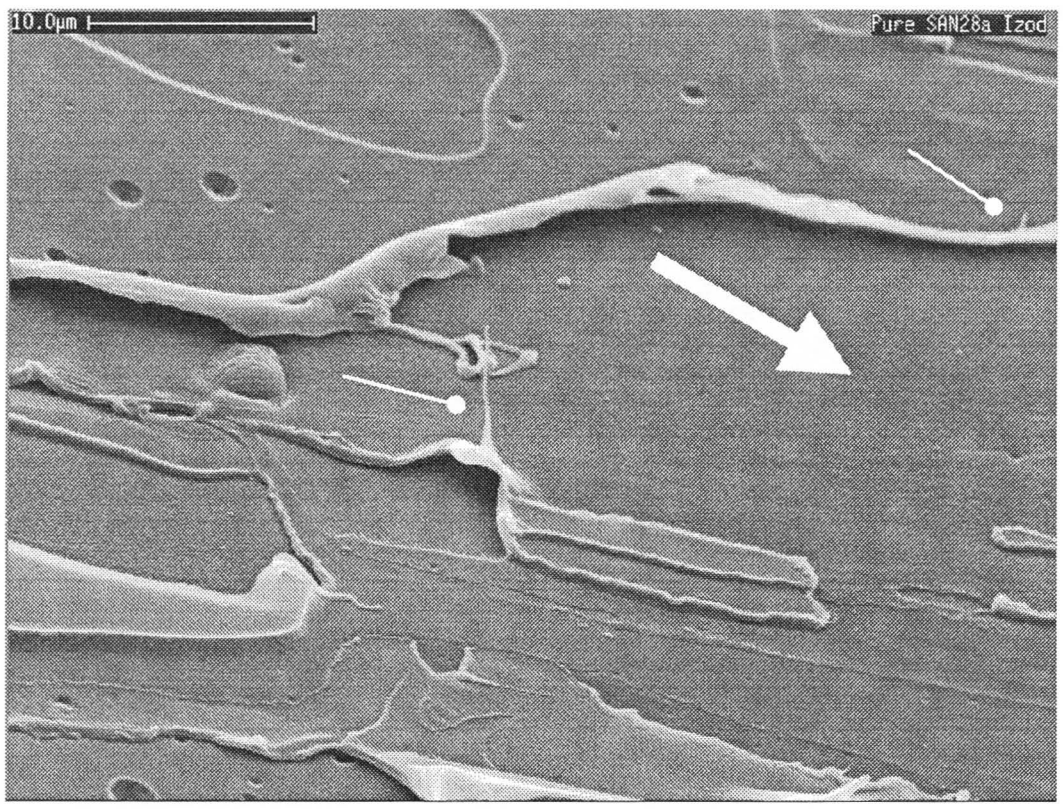

(c)

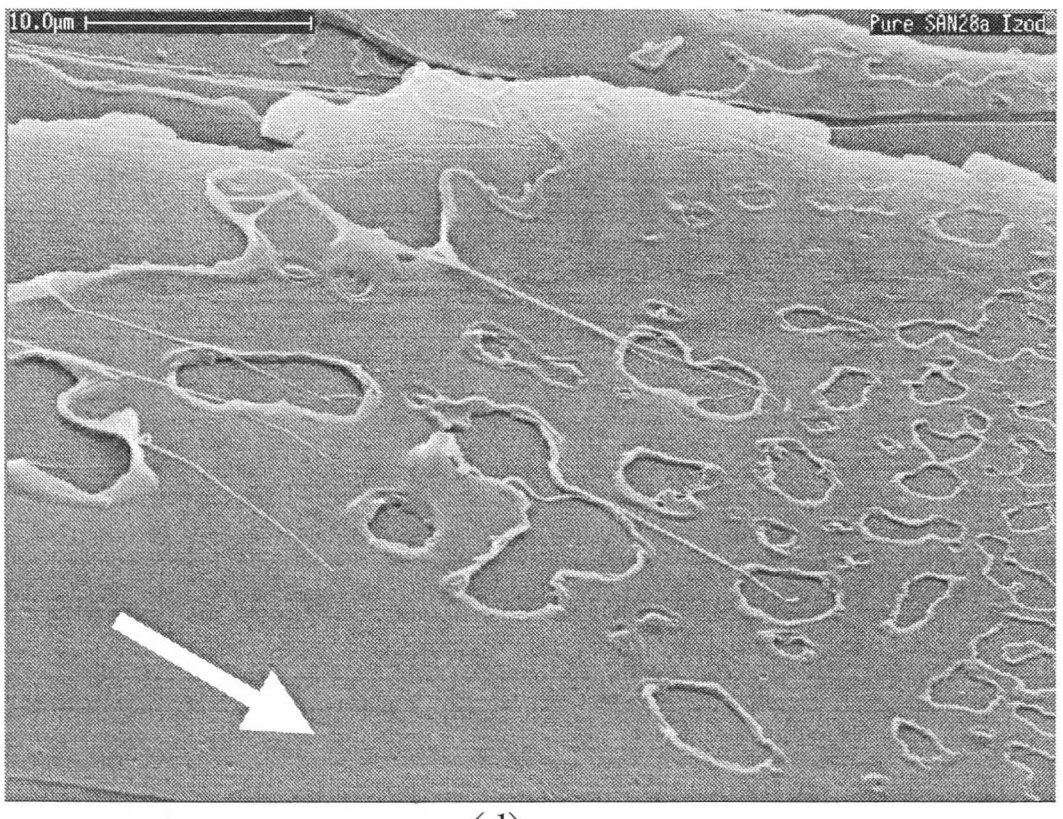

(d)

Figure 4. 13: (c) SAN28a specimen with whiskers pointing normal to the fracture surface (indicated by round-headed arrows); and (d) SAN28a specimen with whiskers pointing in the direction of fracture

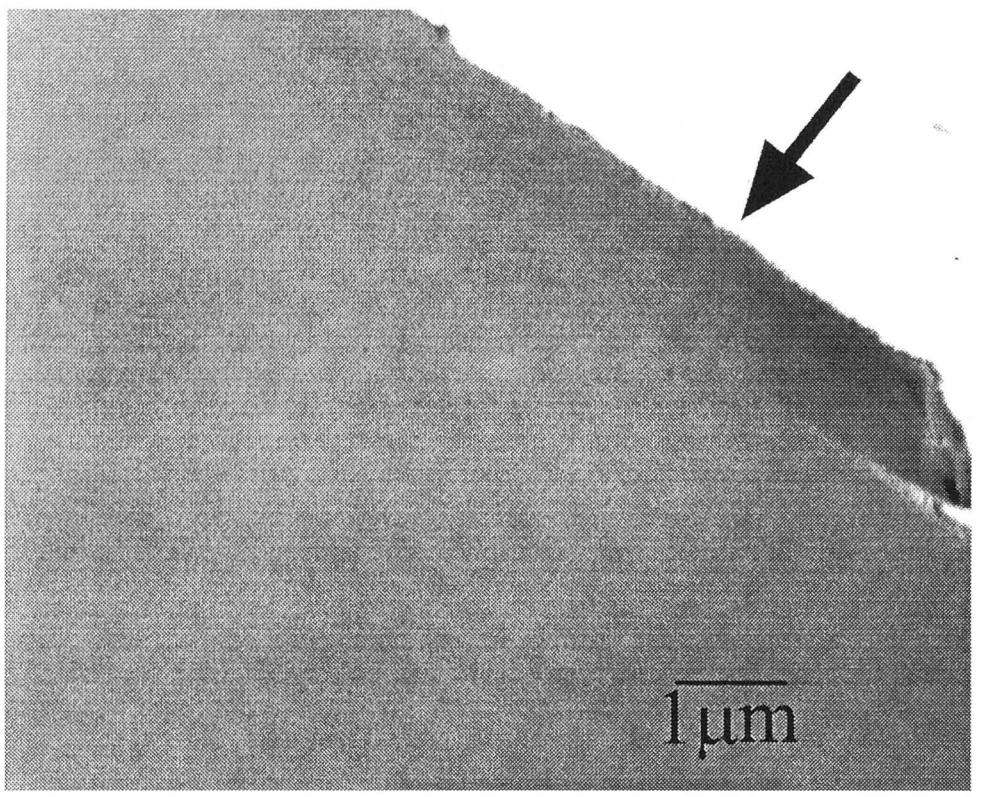

(a)

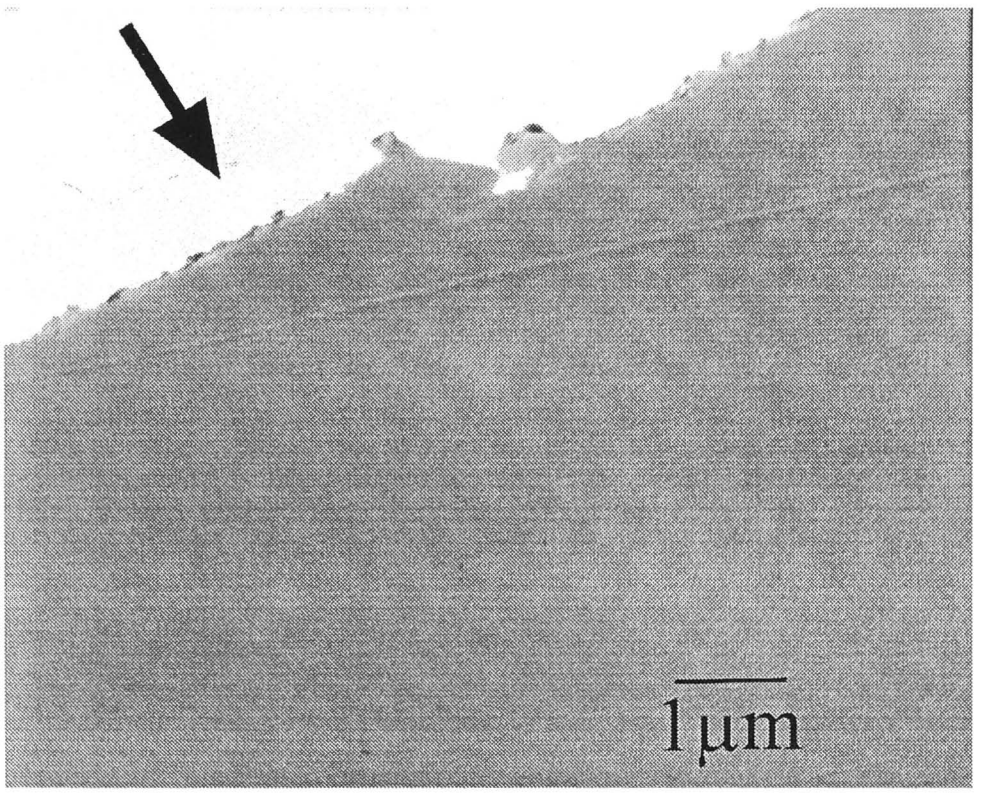

(b)

Figure 4. 14: Transmission electron micrographs of Izod specimen. Arrows indicate the fracture surfaces. (a) SAN22 copolymer; (b) SAN28a copolymer;

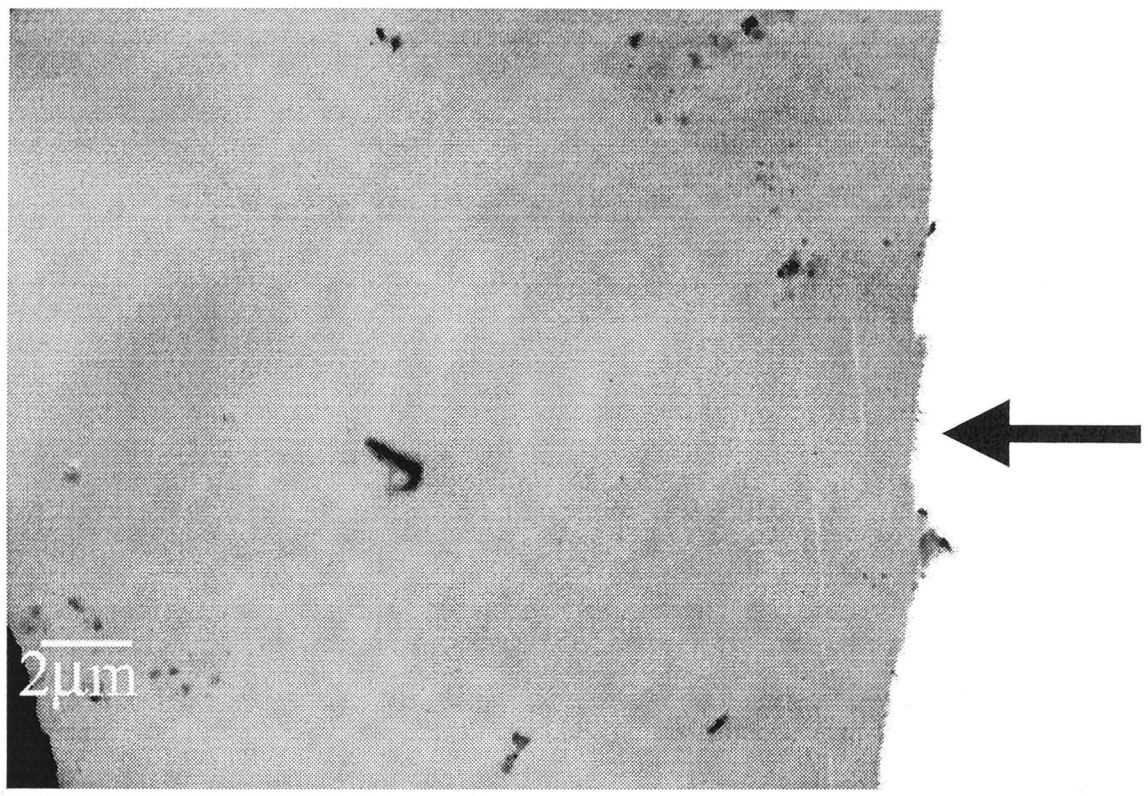

(c)

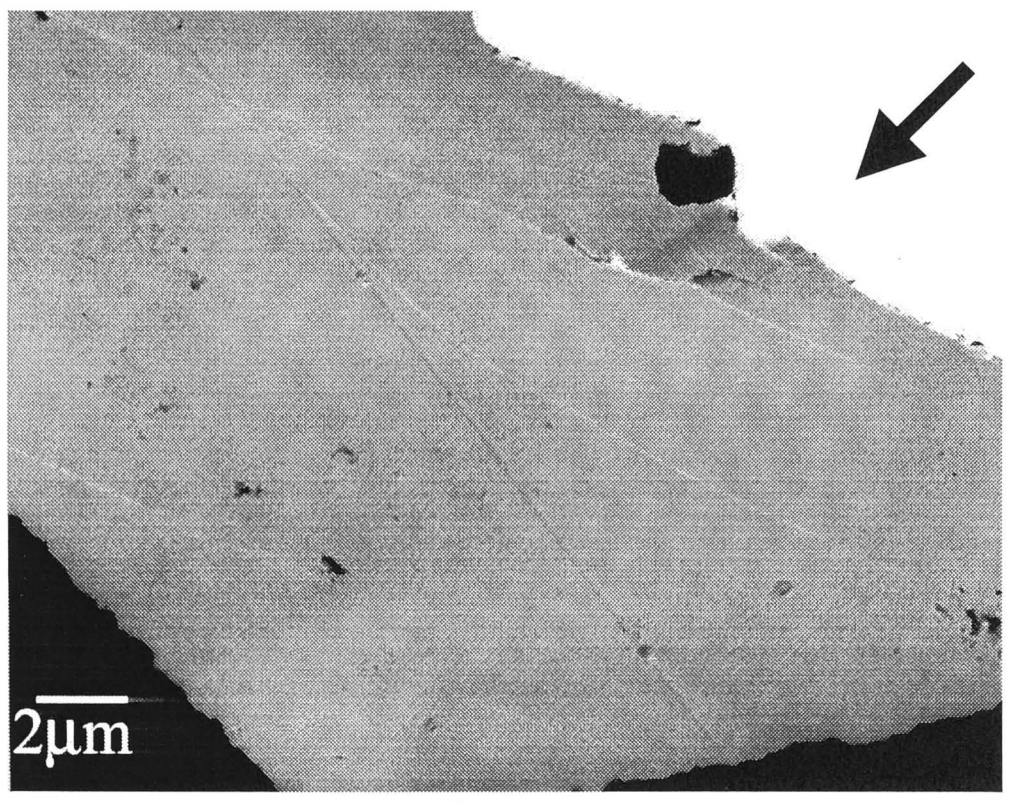

(d)

Figure 4. 14: (c) SMI/SAN22 blend; and (d) SMI/SAN28a blend

4.6. Higher magnification shows patches formed on the fracture surfaces of both SAN22 and SAN28a. Murray and Hull observed the formation of these patches[61]. Additionally, Lauterwasser and Kramer[62] used air craze to confirm the model postulated by Murray and Hull. Moreover, in this work, the fibrils shown around the patch in Figure 4.5(c), verify that the patch is formed by the failure of crazes. The model of a typical craze failure, which forms a patch, is schematically shown in Figure 4.15.

The number of patches formed is determined by the stability of the crazes. Stable crazes travel along a plane, thus reducing the number of patches formed. Alternatively, unstable crazes increase the chances of a secondary crack or higher stress concentration region at the root of craze fibrils. This allows a primary crack to divert from travelling along the midrib, thus creating a bundle of craze fibrils when the craze fails, as seen in Figure 4.5(c). This explains why many small patches are formed in SAN22 and larger but fewer patches are formed in SAN28a.

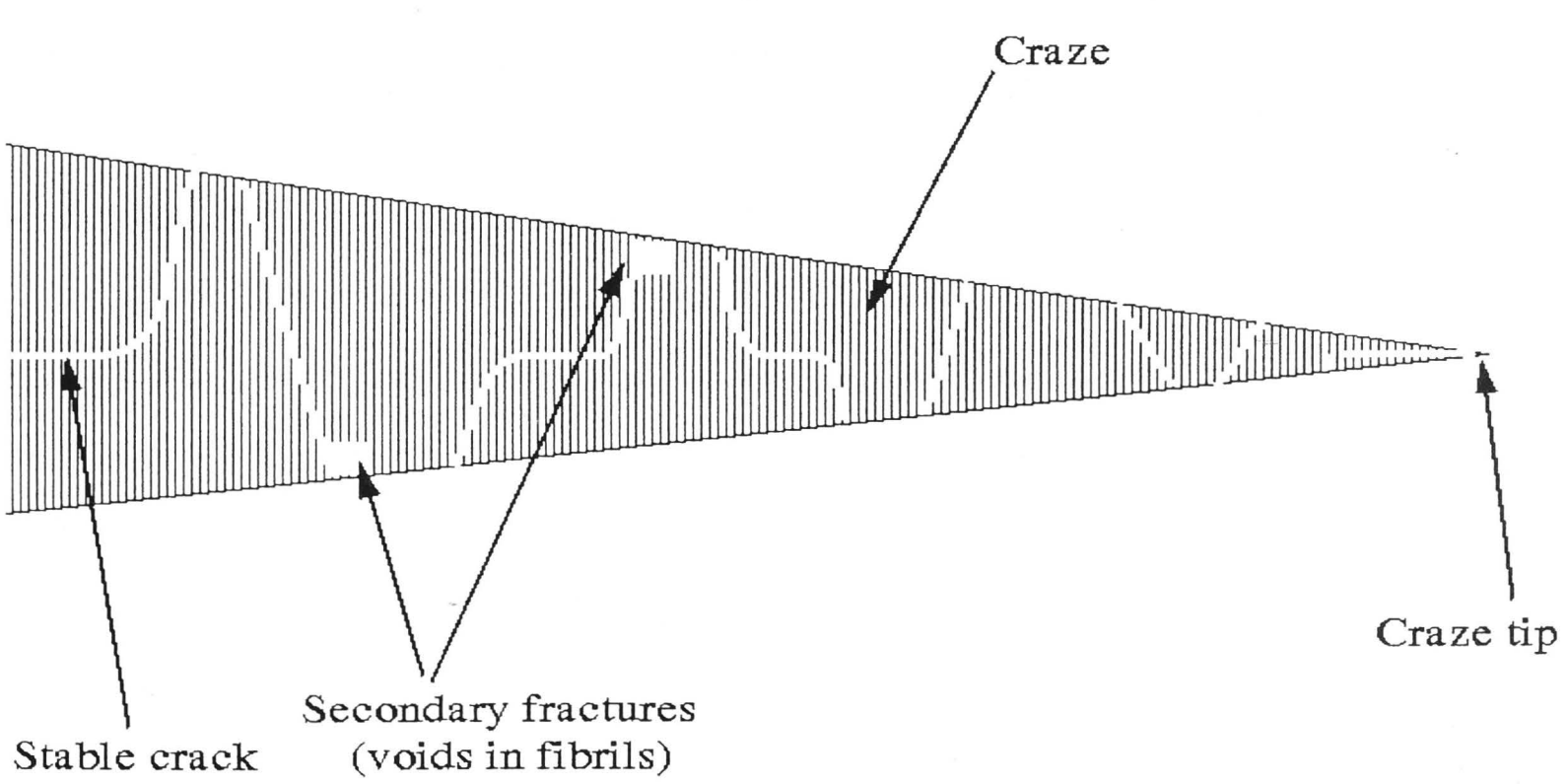

Figure 4. 15: A schematic diagram showing the fracture process of a craze. This process gives rise to the patch pattern[61]

As shown in Figure 4.5 and Figure 4.6, transmission electron microscopy (TEM) explains the development of big and small patches. The micrographs of both SAN22 and SAN28a show a failure of the material as a result of crazing. There is

evidence of craze fibrils at the fracture surface. Multiple crazes can also be seen underneath the fracture surface of SAN22, but not under the surface of SAN28a. The multiple crazes in SAN22 are the result of the change in stress distribution around a rapidly moving craze. As a craze propagates, other crazes may grow from the root of craze fibrils due to stress concentration caused by the fibril failure. Therefore craze branching initiates from the region. Due to the unstable crazes of SAN22, multiple crazing is formed along the craze-polymer boundary. This leads to a smaller initiation region, as shown in Figure 4.4, which reviews the failure of an initiated craze in SAN22 material, before growing to the size of a SAN28a craze and branching off.

The increase in the stress intensity factor with AN content (see Figure 4.9) was previously shown by Kim et al.[59] They attributed the increase to the effect of the inherent ductility of SAN copolymers. In the case of a pure SAN copolymer, inherent ductility can increase with increase in AN content. The high inherent ductility in materials of a high AN content increases the materials' yield stress. Stable crazes were also observed in SAN28a under simple tension. This reduces the chances of other craze growth on the craze-polymer interface in the region of the high stress concentration, increasing the strength of SAN28a.

4.4 Multiple-crazing in notched specimens

Figure 4.10 shows TEM micrographs of both pure and binary blends of SAN22 and SAN28a under SEN tension. The blends show multiple crazing under the fracture surfaces. The multiple crazes do not correspond to the behaviour observed in simple tensile test. It is accepted that multiple crazes are caused by defects that form in the notching of materials, not by unstable crazes in the materials. In the case of SEN tensile specimens, a new razor blade was used to introduce a sharp V-notch at the tip of the U-notch of each specimen prior to testing. However, the V-notch still contained many defects of microscopic scale. When stressed, each of these defects caused stress concentration regions, thus increasing the chances of a multiple craze initiating. Similar behaviours occurred in Izod specimens. However, the extensiveness of multiple crazes in Izod specimens was reduced because the Izod V-notch with a 10 mil radius did not allow the defects to be concentrated in a small location compared to the SEN V-notch.

Scanning electron microscopy of SEN tensile, (see Figure 4.11) reveals different deformation behaviour to that of simple tensile. The river-flow structure

seen in SEN tensile was typical in glassy polymers, and was first observed by Murray and Hull[61, 63] three decades ago. A schematic representation of the formation of river-flow structure is in Figure 4.16. Murray and Hull suggest that as the primary crack propagates through material, it may encounter secondary cracks that form ahead of the primary crack. The propagating crack would meet up with the growing secondary crack, and depending on the relative velocity of the two propagating cracks, the overlap would result in different river-flow structure.

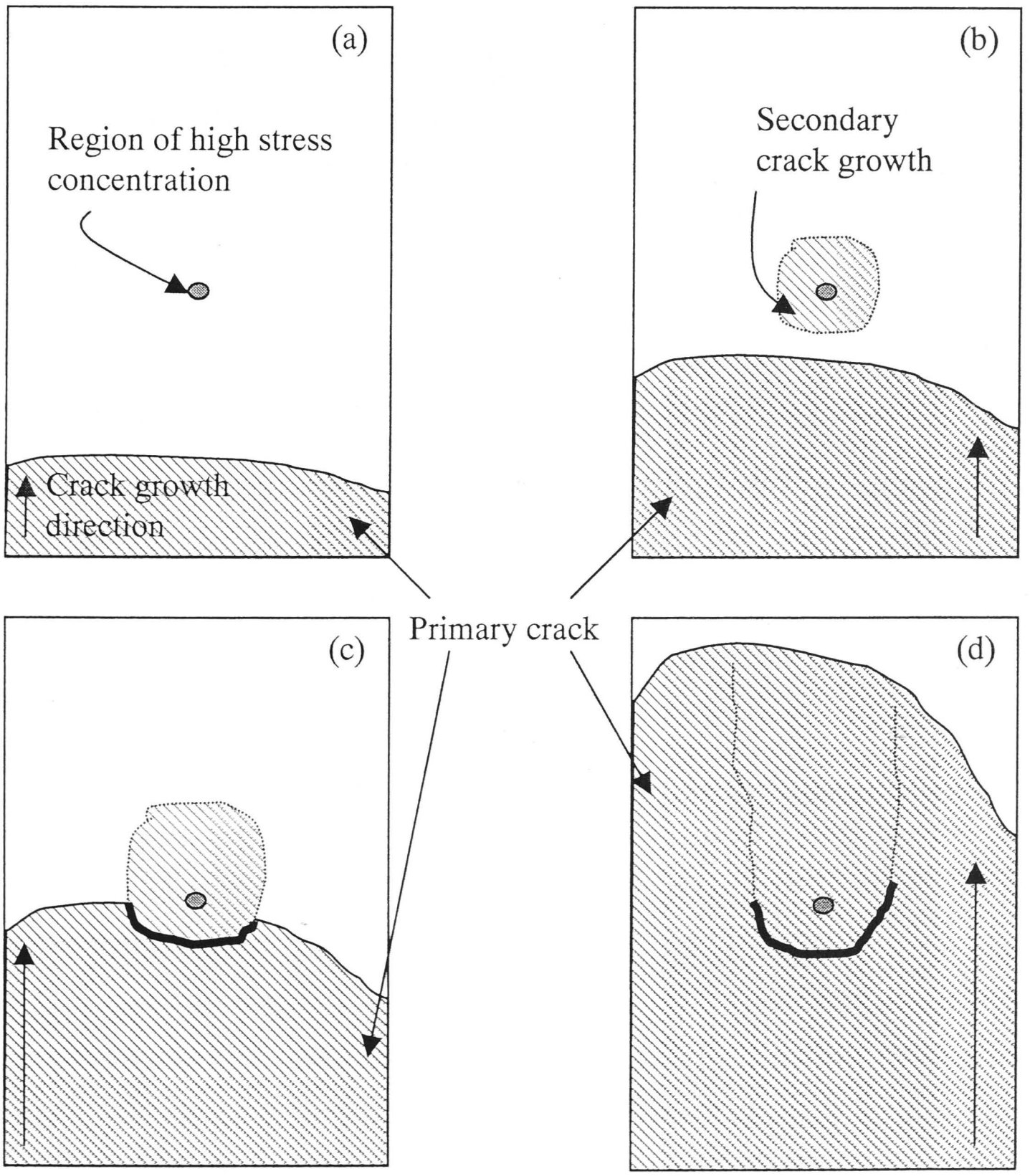

Figure 4. 16: A schematic representation of the formation of river-flow structure in single-edge-notched specimens. (a) Arrow represents the direction of primary crack propagation. Secondary crack formed at high stress region shown as a dot; (b) primary crack propagates further, secondary crack grows spherically outwards; (c) primary crack overlaps secondary crack, secondary crack continues growing; and (d) river-flow structure occurs when primary crack totally overlaps the secondary crack

4.4.1 Molecular weight (M_w) and the weight distribution (MWD) effect

The increase in energy absorption of both simple tensile and SEN tensile, show a foreseeable increase with the increase in AN content, in both pure and binary blends. However, the exceptionally high energy absorption of SAN24 compared to its counterparts, under both simple tensile and SEN tensile tests, were clearly exposed in binary blends. The high mechanical properties of SAN24 were the result of high M_w.

This finding is in accordance with various studies performed previously to determine the influence of M_w on the toughening of polymers[26, 64-66]. Chen[26] noted that by changing the M_w in the range between 1.15×10^{-5} and 1.85×10^{-5}, and keeping the AN content of SAN consistent, tensile strength increases rapidly. In addition, he also observed that M_w affects the surface morphology. Similarly, work by Sauer and Hara[66] have shown that M_w affects tensile rather than compressive stress. Their finding corresponds to Argon and coworkers'[67, 68] concept that shear yielding is independent of molecular chain length. Furthermore, Sauer and Hara have shown that high M_w materials have more stable crazes than low M_w materials. This finding justifies the greater toughness of high M_w material, and agrees with the finding by Yang and Kramer[69]. Yang and Kramer used low-angle electron diffraction (LAED) and Fourier Transform Micro-Densitometry (FTMD) to show that a high M_w polymer has more cross-tie fibrils, thus allowing more entanglements between neighbouring molecular coils. Brown[70] used a model to successfully verify the concept of cross-tie fibrils to enhance the fibril stress in a high M_w polymer.

Recently, Bersted and Anderson[71] proved the M_w effect to be only applicable to materials above a certain M_w threshold. They have also acknowledged that molecular weight distribution (MWD) is important in elucidating tensile properties.

Recently, molecular weight distribution has been considered an influential factor in many properties. Properties like tensile strength in the melt, solution viscosity and melt elasticity are all dependent on the length distribution of molecular chains. In this work, the selection of SAN has been carefully controlled to eliminate the effects of M_w and MWD. The molecular weight distribution in this study is around 2.0 and is kept constant to avoid any effect on the mechanical properties.

4.5 Effect of straining rate on deformation mechanisms

The straining rates for the simple tensile test, SEN tensile test and Izod impact test are termed *low*, *intermediate* and *high* respectively, as described in Chapter 2.

The mechanical results of the Izod impact test show no correlation with an increase in AN content (see Figure 4.12). It is believed that the lack of correlation in Izod mechanical properties was caused by the *high* strain rate.

Several researchers have shown that straining rate affects deformation behaviours and therefore toughness[33, 72-75]. In this work, the straining rate effect is obvious when it is observed by scanning electron microscopy (SEM). SEM shows the surface fractography of SAN change under different strain rates. Figure 4.13 shows an SEM observation of a material pullout in Izod impact. These pullouts, or whiskers, are observed in both fractured pieces of the same Izod specimen and can be distinguished only at a *high* strain rate. Since the material was the same as the material used in tensile specimens subjected to *low* and *intermediate* strain rates, the whiskers formed were the result of strain rate effect. This phenomenon has not been reported in any other literature. However, bridging ligaments observed by Gilbert and Donald[76] can be used to explain the formation of these whiskers. It is believed that at high strain rates, the bridging ligaments become thinner and show improved ductility. Thus, they did not fracture till extensive bending of the specimen had occurred, making the whiskers bend slightly towards the crack growth direction. Whiskers that are vertical to the fracture surface can still be found in our samples, as shown in Figure 4.13(c). This serves as evidence for the above suggestion. After fracture, most of the whiskers collapsed and fell into the direction of crack growth, as shown in Figures 4.13(d).

The bridging ligament acts as a beam when two cracks approach each other on different planes. Under a *high* strain rate, the crack that is in the tension direction travels rapidly, diverting off the planes at some stage and thus creating a whisker in the tension direction. Gilbert and Donald did not observe whiskers, partly because the bridging ligaments in their research had a width of around 3 μm whereas in this case, the bridging ligament is of sub-micron scale. This sub-micron bridging ligament results in ductile deformation, compared to the brittle fracture in Gilbert and Donald's study. The formation of whiskers in one direction (see Figure 4.13) clearly shows that Izod impact is under a Mode I and not a Mode II condition.

Although the effect of AN content was concealed by the *high* strain rate of Izod impact test, the better inherent ductility of high AN content was shown in Figures 4.13(a)-(b), indicating longer whiskers in SAN28a than SAN22. This shows the effect of better inherent ductility in a high AN content material.

Further examination was done on the Izod specimens to determine why others did not observe the whiskers. The specimens were gold coated with a thicker coat prior to SEM examination. SEM observation reveals that the high heat generated under some coating conditions can destroy the whiskers (see Figure 4.17). This may explain why others have not reported this phenomenon.

TEM micrographs in Figure 4.14 indicate multiple crazes in both SAN22 and SAN28a. This supports the claim that two or more cracks propagate in different planes, enabling the formation of whiskers. The appearance of multiple crazes in Izod specimens is the outcome of defects being introduced during the milling of the notches, as discussed earlier. Crazes initiate from these defects, thus forming multiple crazing. However, because of the milled V-notches, the defects were not as concentrated as those in SEN tensile specimens.

The Gilbert and Donald's model, however, did not explain the drawing of the whiskers. It was noticed in Figure 4.13 that the whiskers have pointed ends. This shows that whiskers were being drawn before breakage. The drawing phenomenon was correlated to the adiabatic effect. It was believed that under *high* strain rate, heat could not dissipation easily. The high generated at a localised region was high enough to melt the material, thus allowing the drawing of whiskers.

4.6 Micro-cracks examination

Many authors[77, 78] recognise the micro-cracks as shown in Figure 4.8, as large crazes. Such micro-cracks usually appear in polycarbonate (PC) and polypropylene (PP) placed under tensile test. The phenomenon is observed in this study but only in a SAN copolymer placed under simple tensile test.

It is shown in Figure 4.8 that the number of the micro-cracks has no, or very little, relationship to the materials' toughness. In addition, the scattering in the mechanical properties is too small to have any effect on the amount of micro-crack formation. Also, varying the AN content does not seem to have any effect on the extensiveness of the micro-cracks.

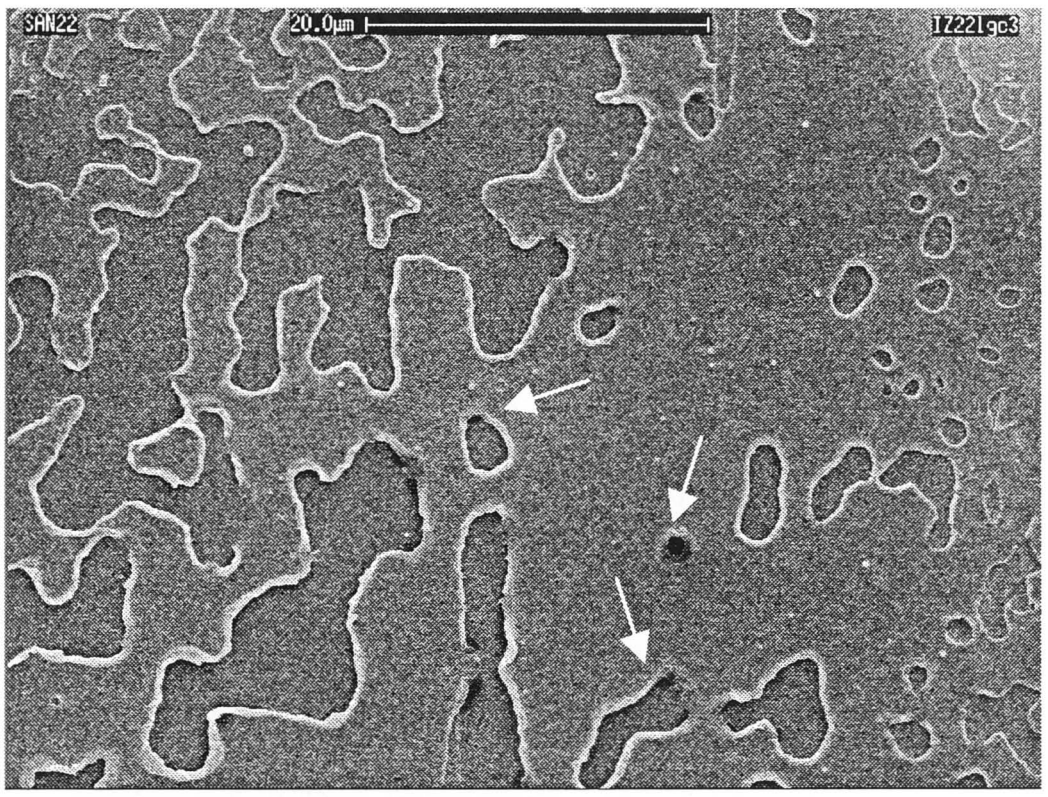

(a)

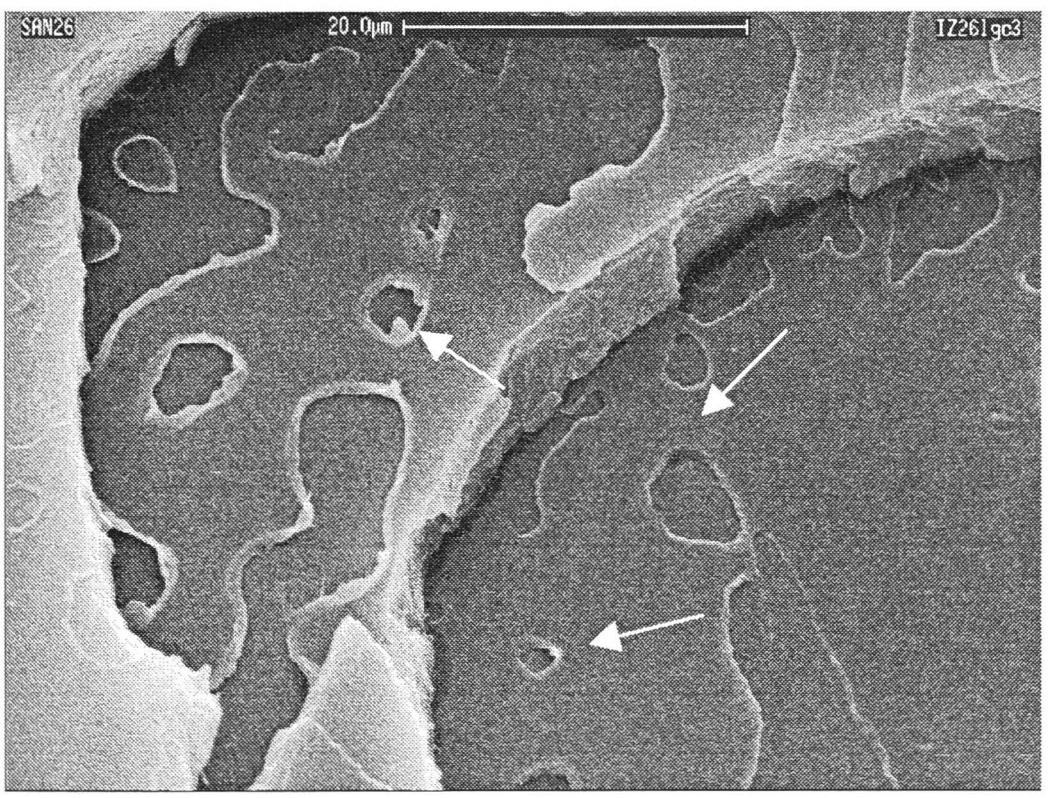

(b)

Figure 4. 17: Scanning electron micrographs of SAN copolymers under "normal" gold-coating condition (i.e. 1.2KV, 20mA for 3 min). Arrows indicate the destroyed whiskers. (a) SAN22; and (b) SAN26

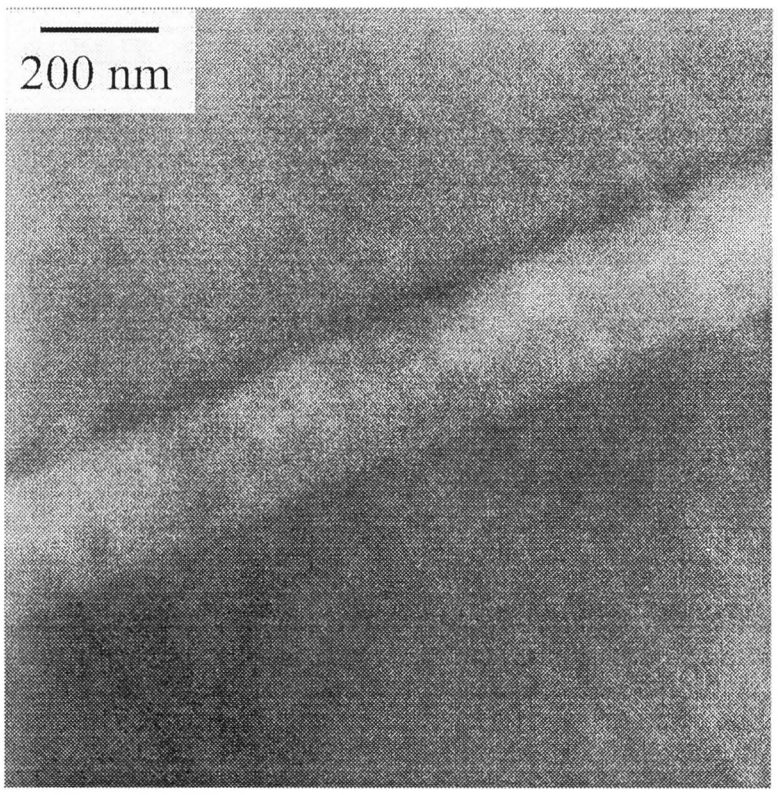

(a)

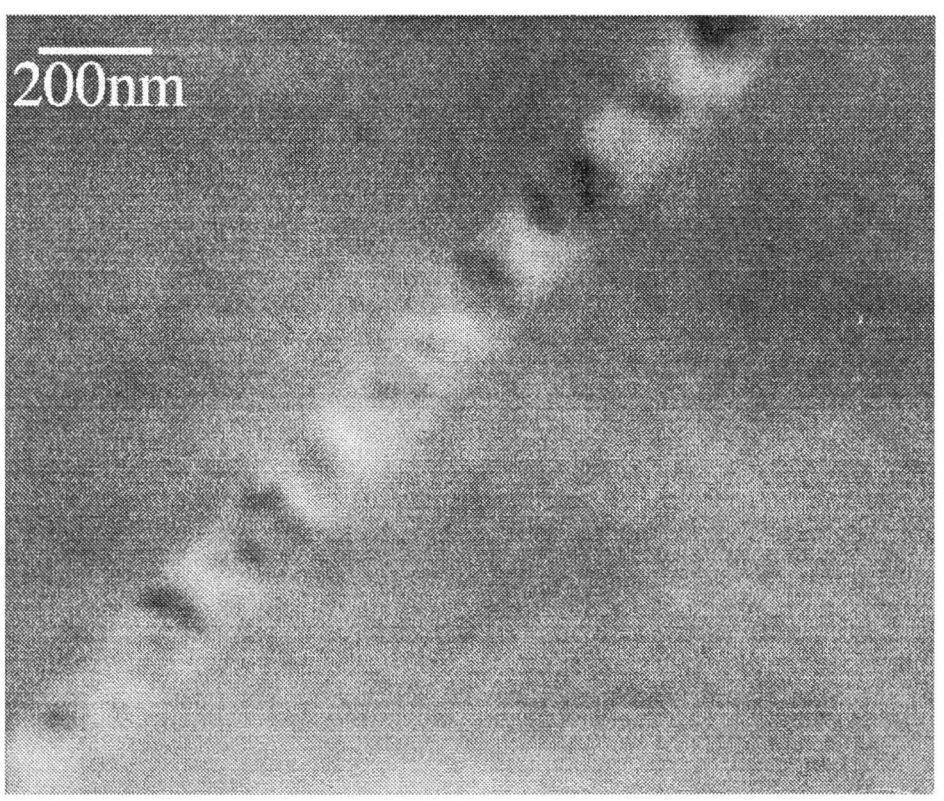

(b)

Figure 4. 18: Transmission electron micrographs of craze structures in (a) micro-crack (large craze); and (b) microscopic craze in SAN copolymer

This section discusses the attempt to identify micro-cracks with the help of electron microscopy. The TEM micrograph of micro-crack structure is shown in Figure 4.18(a). This structure is compared to a true craze structure in Figure 4.18(b), obtained from a bulk specimen. Image of the micro-crack shows dense fibril structure, compared to the true craze structure in Figure 4.18(b), which show fibril bundles. However, the fibril bundles in Figure 4.18(b), could be the damage caused by the direction of cutting.

It is speculated that the micro-cracks are an energy absorption mechanism, which has a toughening effect on the materials. However, the effects were not properly measured in the simple tensile test. The dispersed nature of the micro-cracks appearing on an individual specimen may be due to the amount of artifacts introduced into the specimen during processing.

4.7 Conclusive remarks of deformation mechanisms

Two major factors were discussed in this chapter. Firstly, that acrylonitrile (AN) content affects the toughness of both pure and binary blends of SAN. Secondly, a *high* strain rate conceals the toughness enhancement by the increase of AN content.

AN content influences the inherent ductility of the material. This is shown by the increase in mechanical properties with AN content, in both simple and SEN tensile results (see Figure 4.3 and Figure 4.9). Improved inherent ductility is also observed in Izod impact specimens in the form of whiskers. The length of the whiskers determines the degree of inherent ductility as illustrated in Figure 4.13, material of high AN content (SAN28a) has longer, and thus more stable whiskers than low AN content (SAN22) material. Under simple tension, the inherent ductility is exhibited in the stability of crazes, as shown in Figure 4.4 and Figure 4.6. Unstable crazes are seen in SAN22, in which multiple crazing forms. Stable crazes, and thus a higher inherent ductility are present in SAN28a.

The fracture energy recorded in the Izod impact test, is not effected by an increase in AN content. Since this trend is different from that of the tensile test, it is reasoned that the straining rate causes the fracture energy to remain constant, despite the increase in AN content. The straining rate of Izod impact was calculated to be several times greater than that of tensile test. Thus the *High* strain rate conceals the effect of AN content on mechanical properties but it generates an unusual formation of whiskers on the fracture surface of pure SAN, as shown in Figure 4.13. Gilbert and

Donald's[76] observation of a bridging ligament is used to postulate the formation of whiskers under Izod impact.

Also observed is the effect of high M_w. Considering that both pure and binary blends of SAN24 have high M_w compared to the other SANs, it is deduced that high M_w causes the high-energy absorption of SAN24 materials. Consequently, the M_w for other SANs is kept the same, so that the only variable between them is the AN content.

CHAPTER FIVE

The role of rubber toughening on high-thermal-resistant ABS

5.1 Introduction

Glassy polymers are usually subject to brittle failure, particularly under high straining rates or with the presence of notches. Therefore glassy polymers often have a rubbery phase incorporated to improve the ductility. The term "rubber-toughened" is used to refer to the addition of this rubbery phase, which enhances the mechanical behaviour of the matrix polymer. As glassy polymers can be toughened with dispersed and well-grafted rubber particles without significantly impairing their other desirable properties such as gloss and processibility, the development of rubber-toughened polymers was a great advance for the plastics industry. The addition of rubber also reduces the notch sensitivity.

The mechanical and deformation performance of SMI modified poly(acrylonitrile-butadiene-styrene) (ABS) is investigated in this chapter. It can be seen in Figure 5.1 that ABS has a higher energy absorption under notched Izod impact than its pure matrix counterpart, poly(styrene-N-phenyl maleimide) and poly(styrene-co-acrylonitrile) (SMI/SAN). In this study, the three types of ABS, named ABS1, ABS5, and ABS15, were examined. These ABS's differ in rubber particle size, particle size distribution and structure. Details of the materials can be found in Chapter 2. Rubber-toughened polymers have been studied for several decades. Much of this work was done by Bucknall[11, 23], and Paul[24, 29, 79, 80].

It is known that a material's toughness depends on its strain rate, deformation mode, and notch sensitivity. Therefore, to achieve a true evaluation of the ABS toughness, three tests in different loading modes were performed. In addition, rubber particles in ABS are generally known to have a Young's modulus three orders of magnitude lower than that of the glassy matrix. This difference in magnitude allows the build-up of stress at the interfaces of particles during mechanical loading, thus

affecting the deformation behaviours. These behaviours were compared with the mechanical properties. In this study, only the blends of SAN22 and SAN28a were examined in detail because they have the poorest and best mechanical properties respectively.

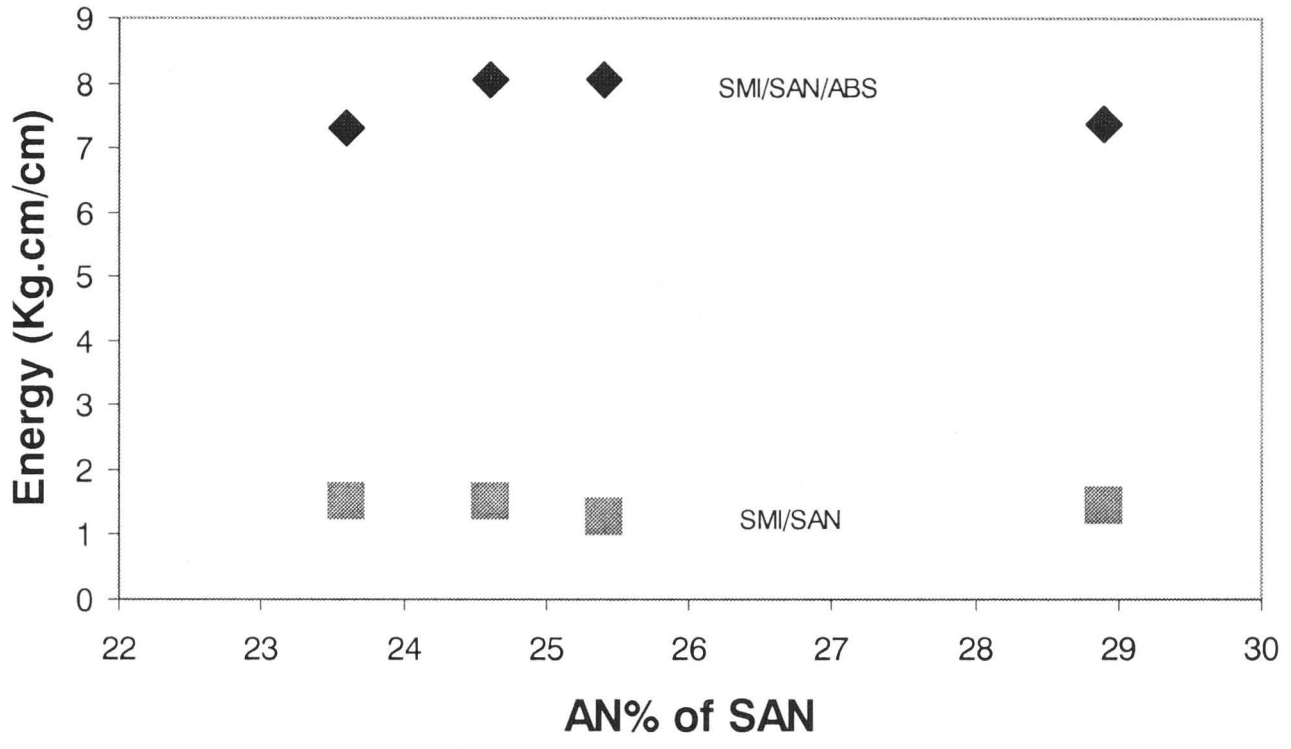

Figure 5. 1: Comparison of polymer and ABS toughness for notch sensitivity

The major theme in the present chapter is the comparison of morphology, mechanical properties and toughness of the ABS materials. The goal is to comprehend the toughening mechanisms in order to improve the fracture toughness.

5.2 Toughening mechanisms of ABS

One way to toughen a polymer is to incorporate a rubbery phase. The rubbery-phase-reinforced materials are subject to many influences that affect the toughening mechanisms. The rubbery phase initiates a deformation, which is responsible for the energy absorption of ABS before fracture. The energy absorbed by ABS is mostly through deformation in the matrix adjacent to the rubbery phase, rather than the deformation of the rubber particles. It is also believed that external factors, such as straining rate and notch-sensitivity, can affect the toughness enhancement of the materials. Other factors, such as the AN content, have been explained in the previous chapter. The effect of AN content is again discussed in this chapter, in relation to the AN content of ordinary ABS.

Apart from matrix crazing, particle cavitation was often observed in the deformed ABS. That raised a question of whether particle cavitation is a better toughening mechanism than crazing. Kozii and Rosenberg[81] concluded that particle cavitation absorbs the least energy. Bucknall et al.[82] also suggested that cavitation itself cannot be the main energy absorption mechanism. This conclusion is consistent with the discovery by Newman and Strella[17], reported more than three decades ago, that particle deformation alone cannot account for more than a small fraction of impact energy.

Another possible matrix deformation mechanism is shear yielding. Because shear yielding cannot be seen by electron microscopy, small angle X-ray scattering (SAXS) was used to demonstrate the presence of shear deformation[83]. The mechanics of crazing and shear deformation, and whether particle cavitation is the precursor of these deformations, are briefly discussed below. Full details of formation of craze and shear deformation can be found in reference[84].

5.2.1 Matrix crazing

Here the term "crazing" refers to the microscopic damage, which can occur in the polymeric materials. Crazing has been observed as the main toughening mechanism for some polymers, like polystyrene (PS). A craze is a microscopic crack bridged by fibrils. It reflects light off the base surfaces, causing opacity of the damaged zone. This makes crazing easy to identify as it occurs wherever stress whitening is seen. Crazes are usually nucleated at an imperfection caused by flaws, dust particles, and the like. When formed, a craze increases the specimen's volume, by creating inter-fibril space. The failure of fibrils introduces voids. These voids expand slowly by the rupture of the surrounding fibrils until the void becomes a crack of critical size. Fracture occurs when a crack propagates along the craze midrib, or along the root of the fibrils, as discussed in Chapter 4. The craze microstructure can be found in Figure 4.1.

Argon and Cohen[85] have shown in their model that butadiene (Bt) in rubber particles acts as plasticizer for craze fibrils. As the formation of craze creates a negative pressure in the surrounding materials, Bt was sucked from the rubber particles into the craze fibrils. Argon and Cohen's model was supported by results

presented in this study. Bt absorbed by the crazes was stained by osmium tetraoxide (OsO_4), and darkened the crazes.

5.2.2 Matrix shear yielding and particle cavitation

Shear yielding of the matrix also plays a major role in the toughening of rubber-toughened polymers. Shear yielding is a permanent deformation, which dominates in some polymer systems like epoxy blends, polycarbonate (PC) and nylon. Often, the deformed specimen can return to the original shape when heated above its glass transition temperature (T_g). Unlike crazing, shear yielding does not increase the specimen volume. Crazing and shear yielding can take place simultaneously[86]. Their occurrence depends upon the stress-state and the nature and speed of the applied stress.

It is generally accepted that rubber particles act as initiators for shear bands. Furthermore, it has been demonstrated that shear yielding usually accompanies rubber particle cavitation[11, 14, 16, 87-91]. Whether cavitation encourages shear yielding or vice versa is yet to be determined. In principle, when rubber particle cavitation occurs, hydrostatic tension is relieved, thereby reducing the tendency of crazing, and encouraging shear yielding. Generally, energy absorption is increased under shear yielding due to the volume involved.

5.3 Evaluation of mechanical results and deformation behaviours

Three types of mechanical testing were used to evaluate the strain rate effect. Results from these tests will be discussed in terms of loading conditions. Deformation behaviour on the fractured surfaces was evaluated using a scanning electron microscope (SEM). A transmission electron microscope (TEM) was used to determine the fracture behaviour immediately underneath the fractured surfaces. Small angle X-ray scattering (SAXS) was also used to verify the deformation that cannot be seen by the electron microscopy.

5.3.1 Mechanical results

The fracture energy of simple tensile test is shown in Figure 5.2. The result shows an increase in fracture energy with the increase in acrylonitrile (AN) content in SAN matrix (SAN_m). It also reveals the different toughness of ABS's in the order of ABS1>ABS15>ABS5, with the toughness of ABS15 closer to ABS5. ABS1 shows a greater increase in toughness trend as AN content increases, compared to ABS5 or ABS15's trend.

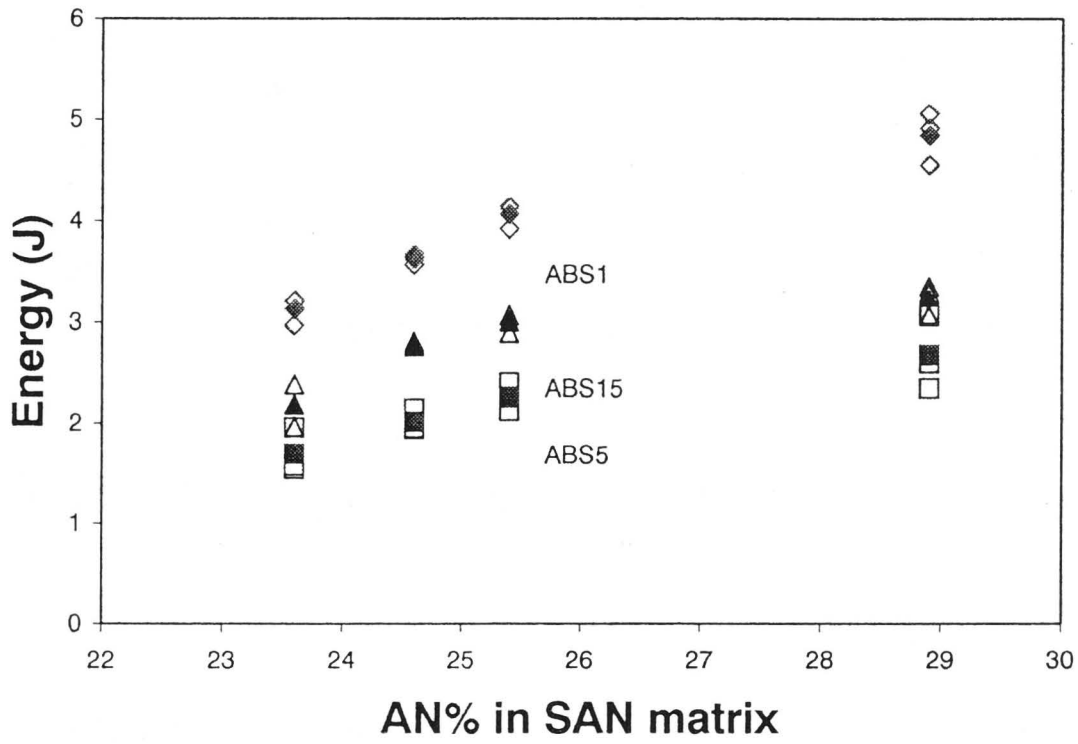

Figure 5. 2: Energy absorption of ABS under simple tensile test vs. acrylonitrile (AN) content (solid points represent the average value whereas open points represent individual data point)

The plot of stress intensity factor (K_I) is shown in Figure 5.3 with the K_I values of ABS's in the order of ABS1>ABS15>ABS5, which is in the same order as that in simple tensile test. Although the measuring unit of K_I is different from that of simple tensile, the result still shows the increase in toughness with the increase in AN content.

Results of the Izod impact test are shown in Figure 5.4, in which the energy for total fracture, energy to initiate crack and energy for crack propagation were plotted. The results suggest that the energy absorption for crack initiation is greater than for crack propagation, except in the case of low AN content in ABS15 systems (see Figure5.4(c)), where the two energy levels are almost the same. The plots also suggest that the energy absorption in ABS5 system is not affected by the variation in

AN content. However, ABS15 seems to be more sensitive to AN content variation, as shown in Figure 5.4(c). The sensitivity to AN content is ABS15>ABS1>ABS5.

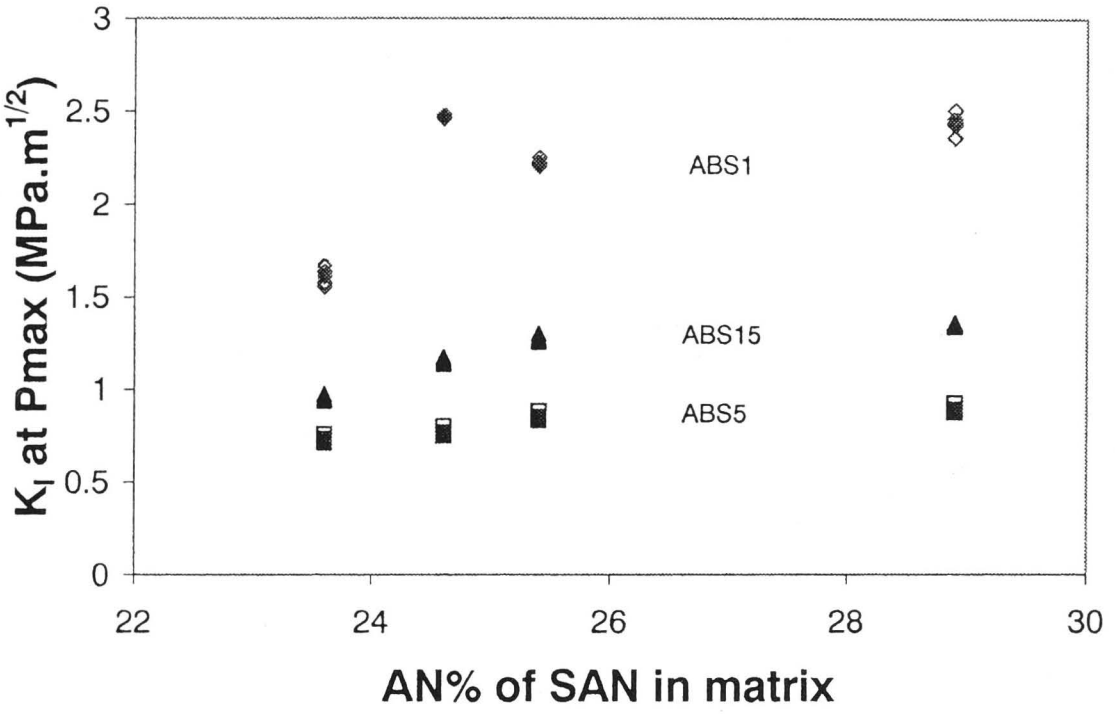

Figure 5. 3: Variation of stress intensity factor (K_I) vs. acrylonitrile (AN) content for ABS

5.3.2 Electron microscopy

The fracture behaviours of ABS with a constituent of SAN22 and SAN28a constituent, tested under simple tensile test, are shown in Figure 5.5 and Figure 5.6 observed under SEM and TEM, respectively. SEM micrographs in Figure 5.5 are used to examine the fracture behaviour on the fracture surfaces. Rubber particles debonding and fractured are indicated by (*D*) and (*F*), respectively, in Figures 5.5(a)-(b). The micrographs reveal that the materials in ABS1 were drawn into fibrils before fracturing. When the drawn fibrils fail, they snapped back, forming coarser surfaces as shown in Figures 5.5(c)-(d).

The fracture surfaces of ABS5 (see Figures 5.5(c)-(d)) are smoother than ABS1 (see Figures 5.5(a)-(b)). It appears that ABS5 was more brittle and thus fibril drawing could not occur. Figures 5.5(c)-(d) and Figures 5.5(e)-(f) also show that ductility of the materials increases with AN content.

Rougher surfaces on TEM micrographs show the ductility of ABS1 material (see Figures 5.6(a)-(b)). ABS5 (see Figures 5.6(c)-(d)), however, shows less deformed surfaces. Ductility increase with AN content is evident on the fracture

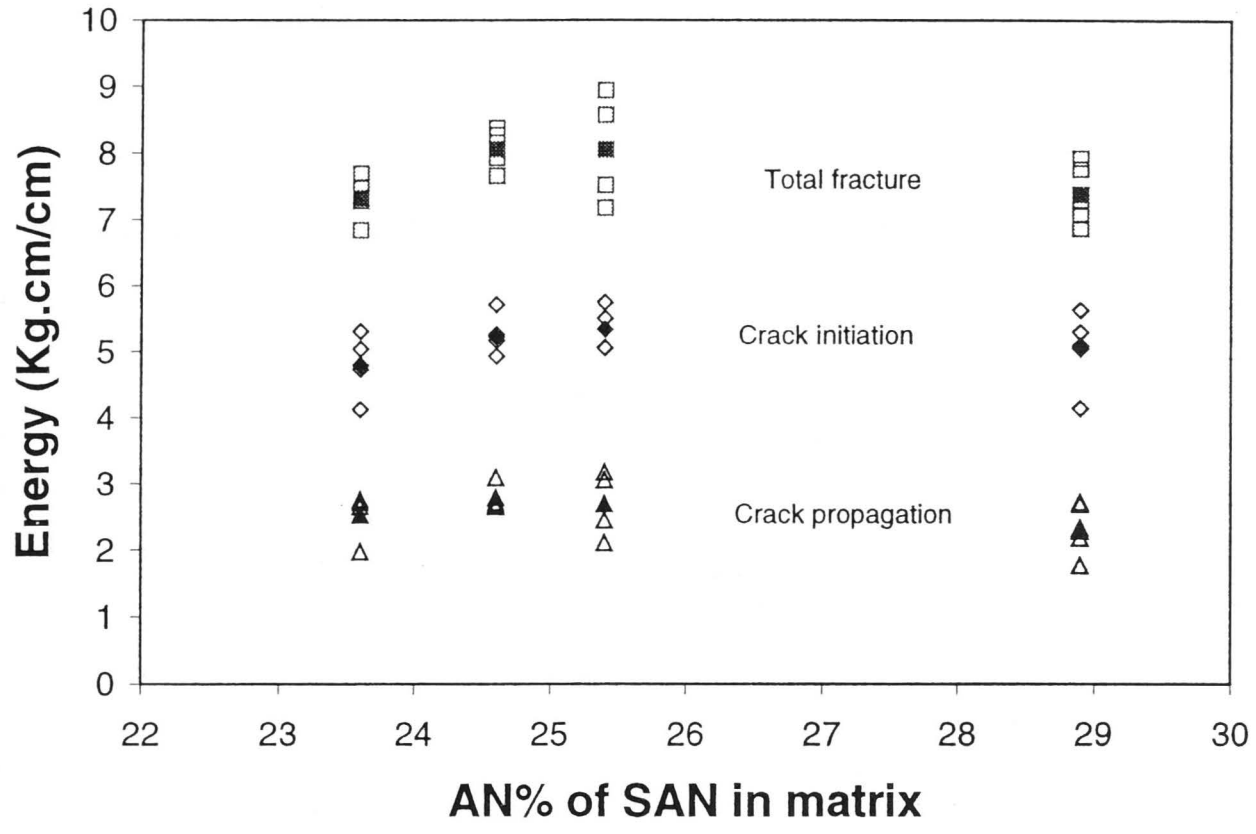

(a)

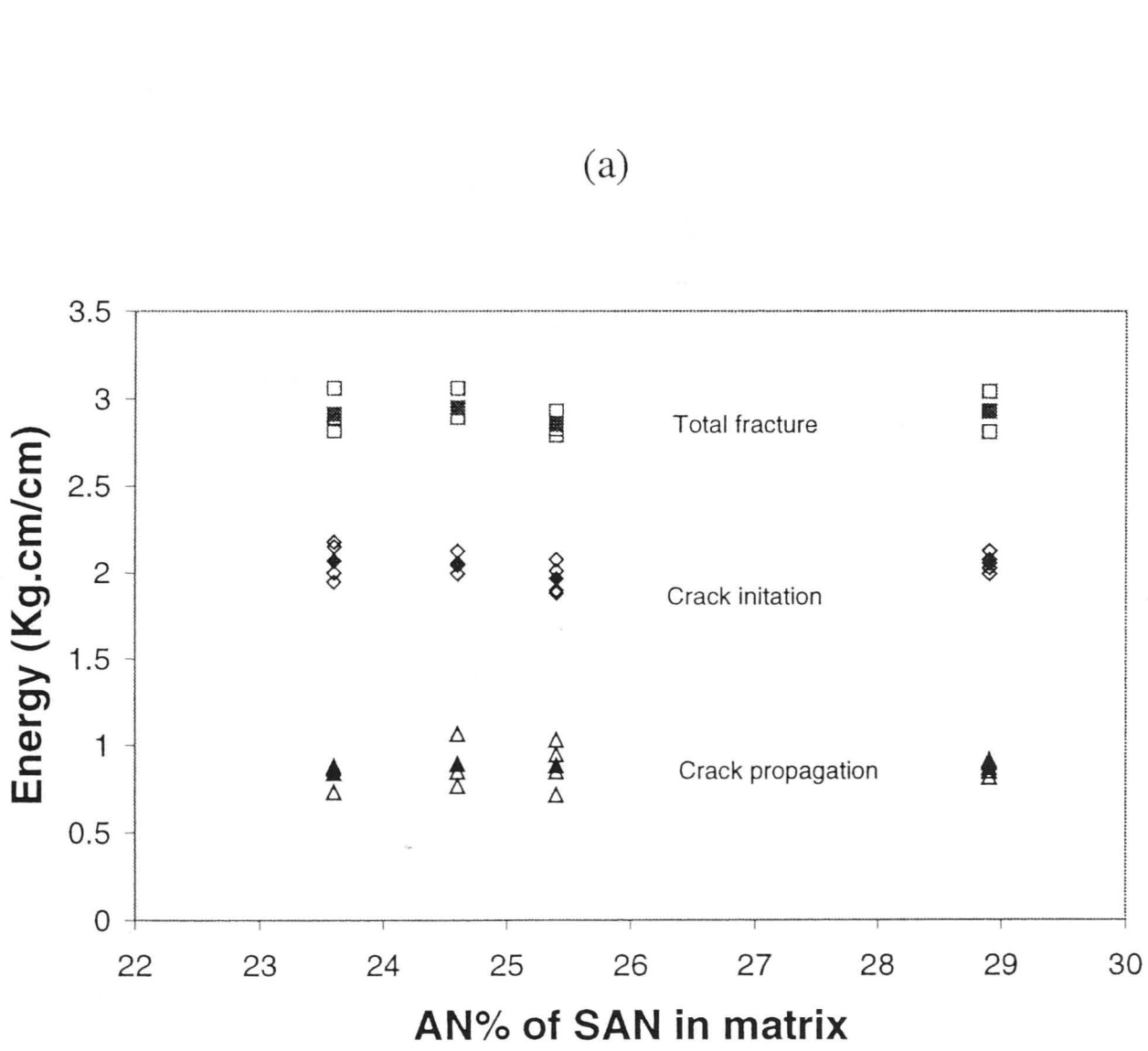

(b)

Figure 5. 4: Mechanical results of instrumented Izod impact vs. acrylonitrile (AN) content. (a) impact energy of ABS1; (b) impact energy of ABS5; and

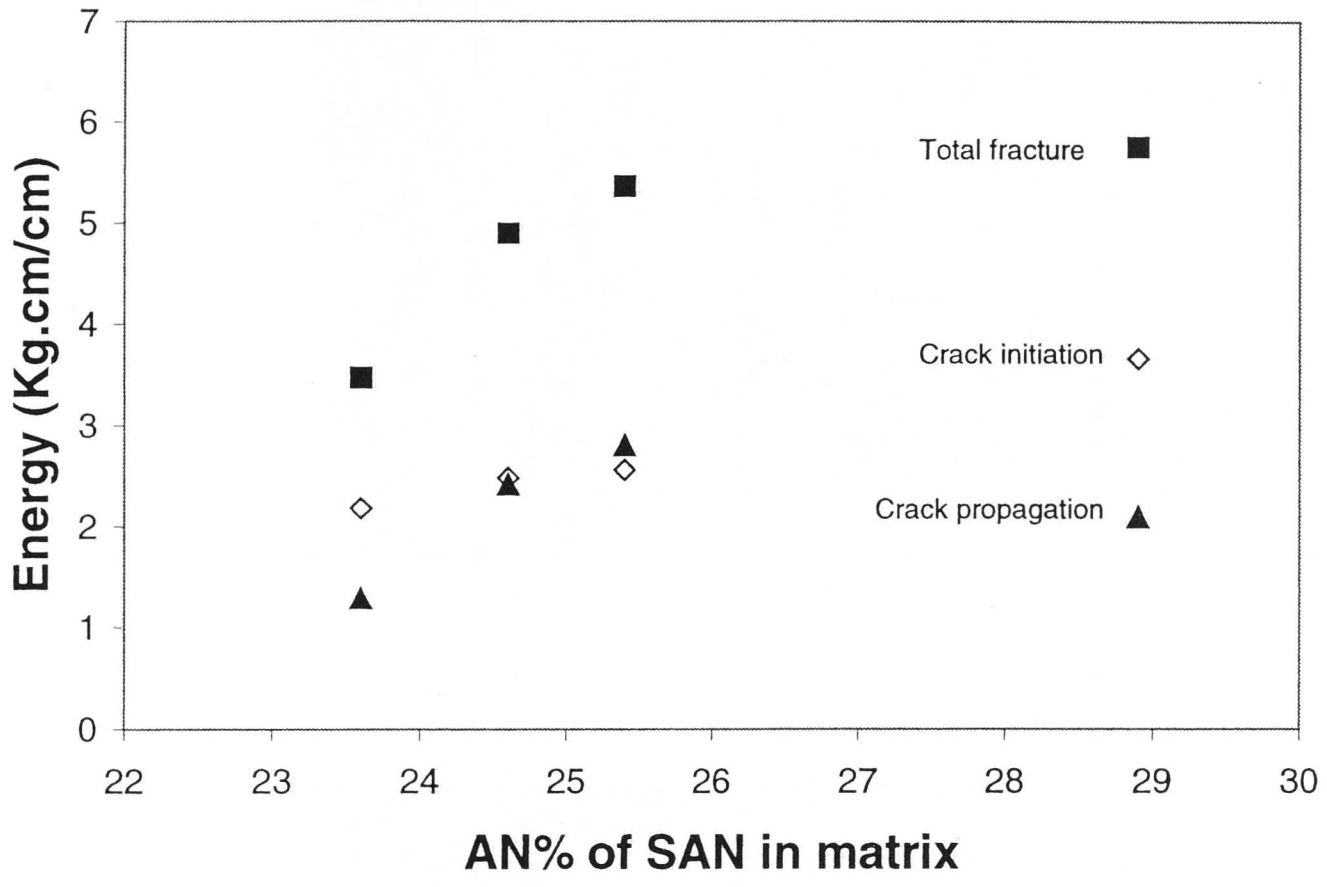

(c)

Figure 5. 4: (c) impact energy of ABS15

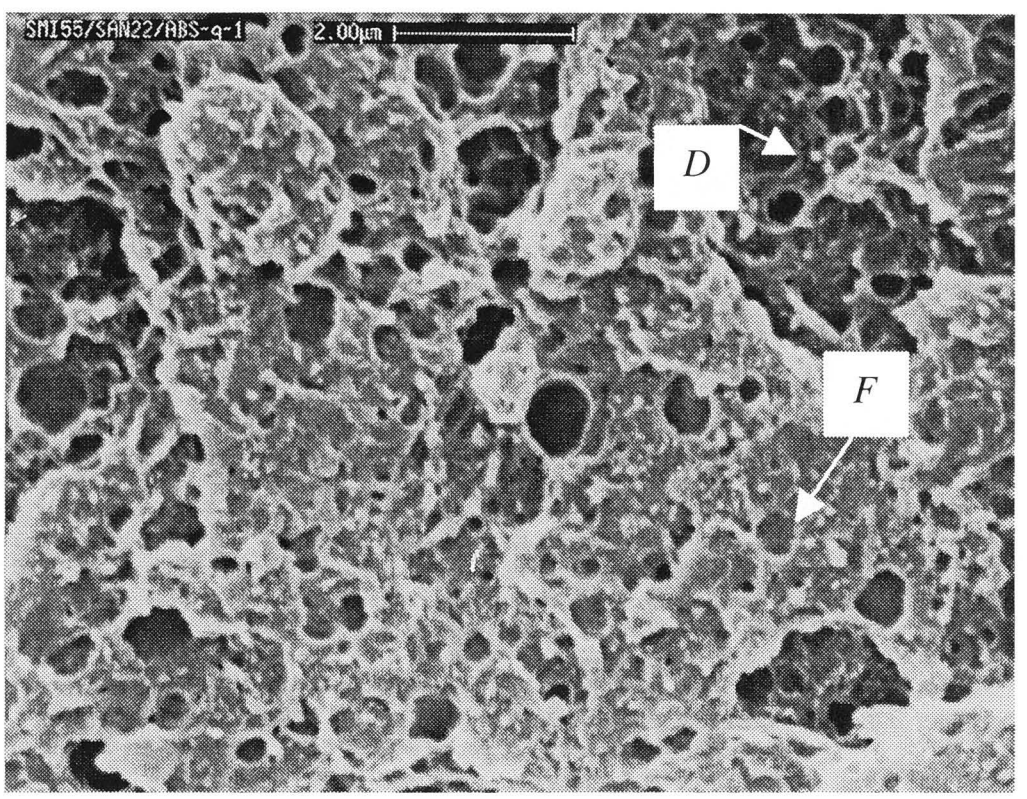

(a)

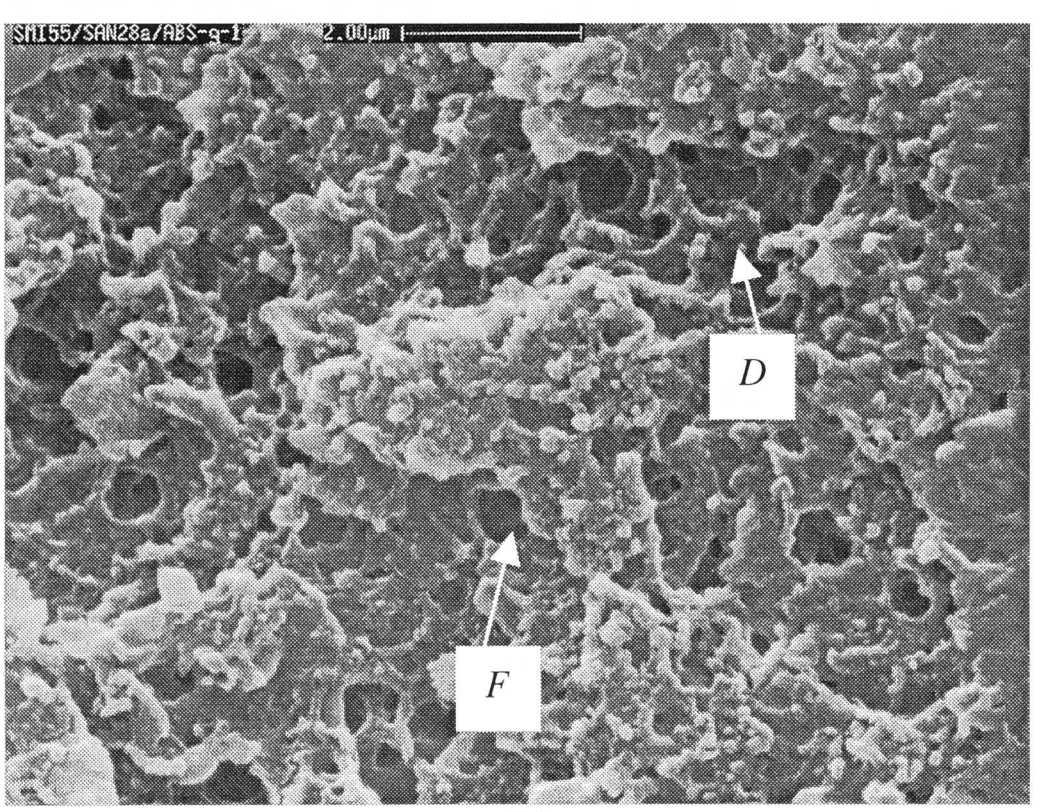

(b)

Figure 5. 5: Scanning electron micrographs of simple tensile fracture surfaces. Both *D* and *F* represent debonding and fracture of rubber particles, respectively. (a) ABS1 with SAN22; (b) ABS1 with SAN28a;

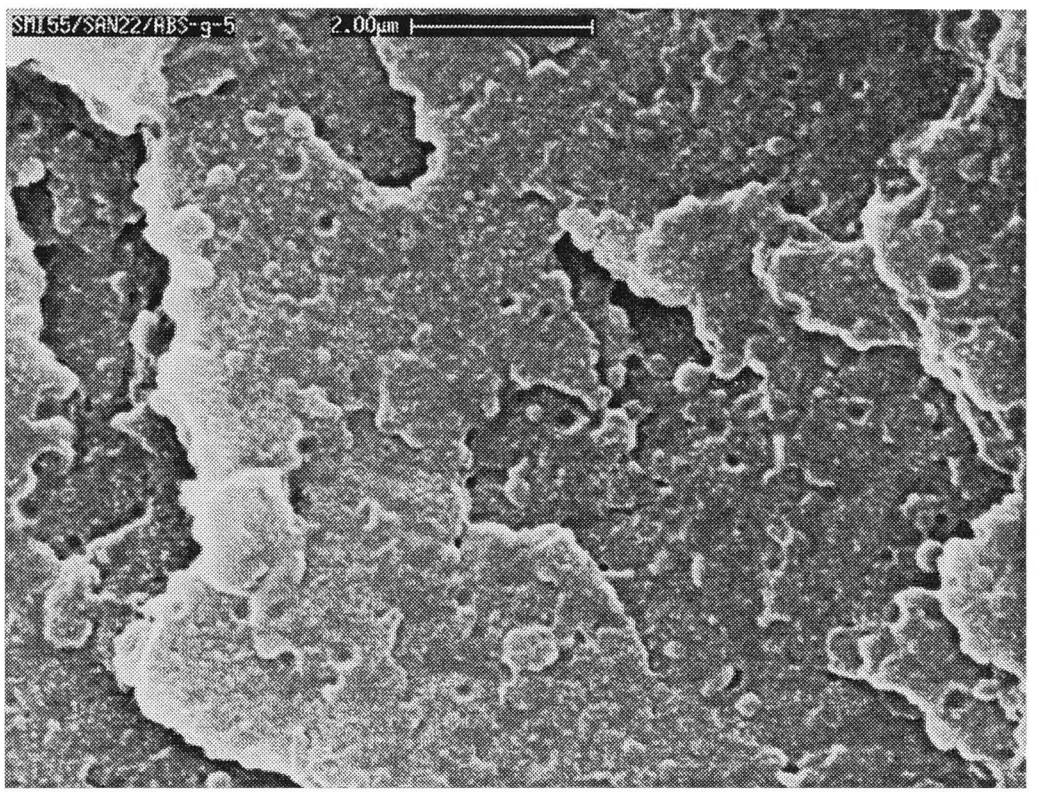

(c)

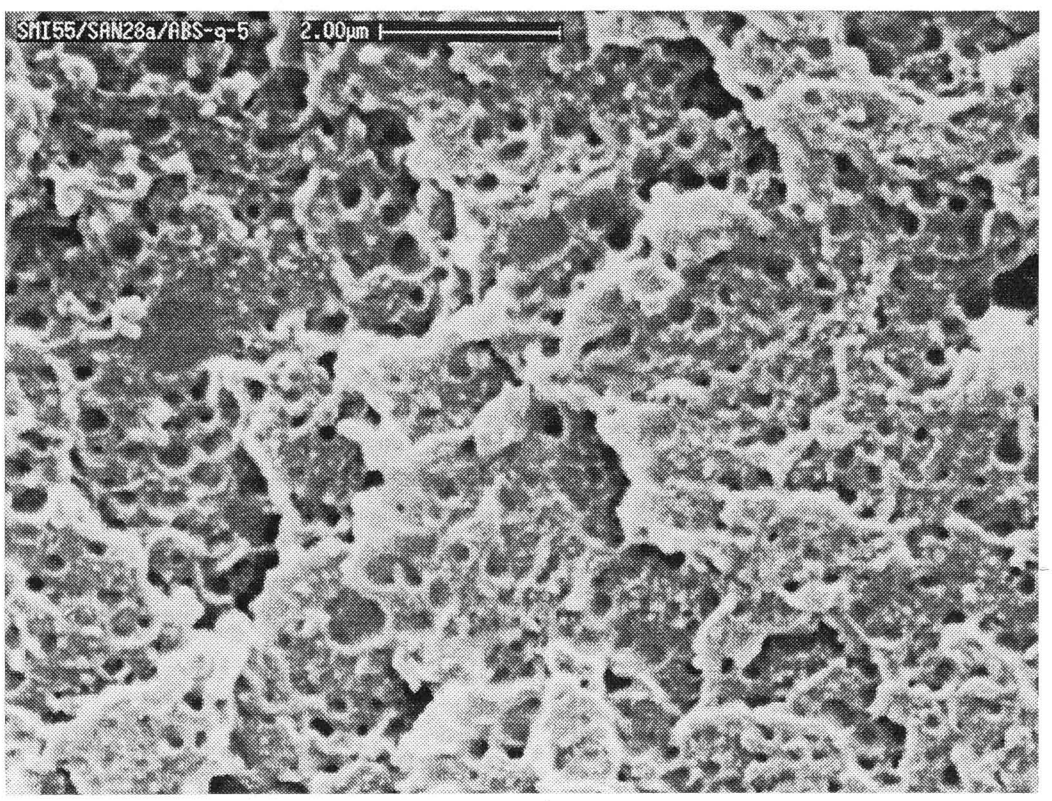

(d)

Figure 5. 5: (c) ABS5 with SAN22; (d) ABS5 with SAN28a;

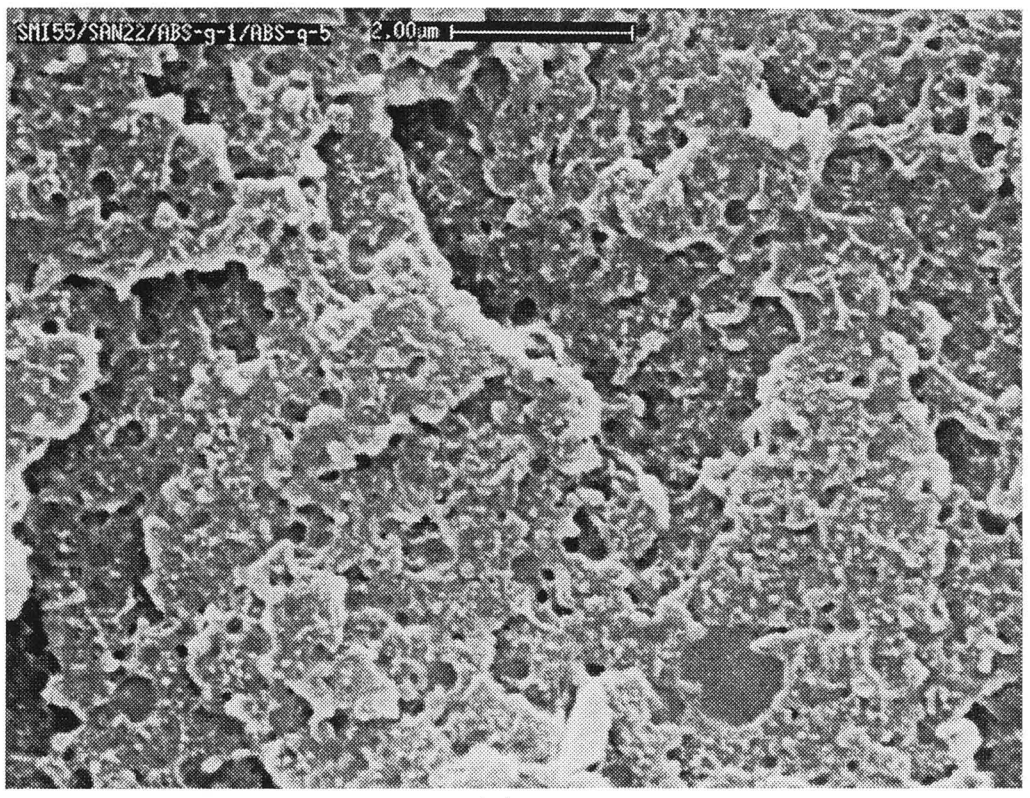

(e)

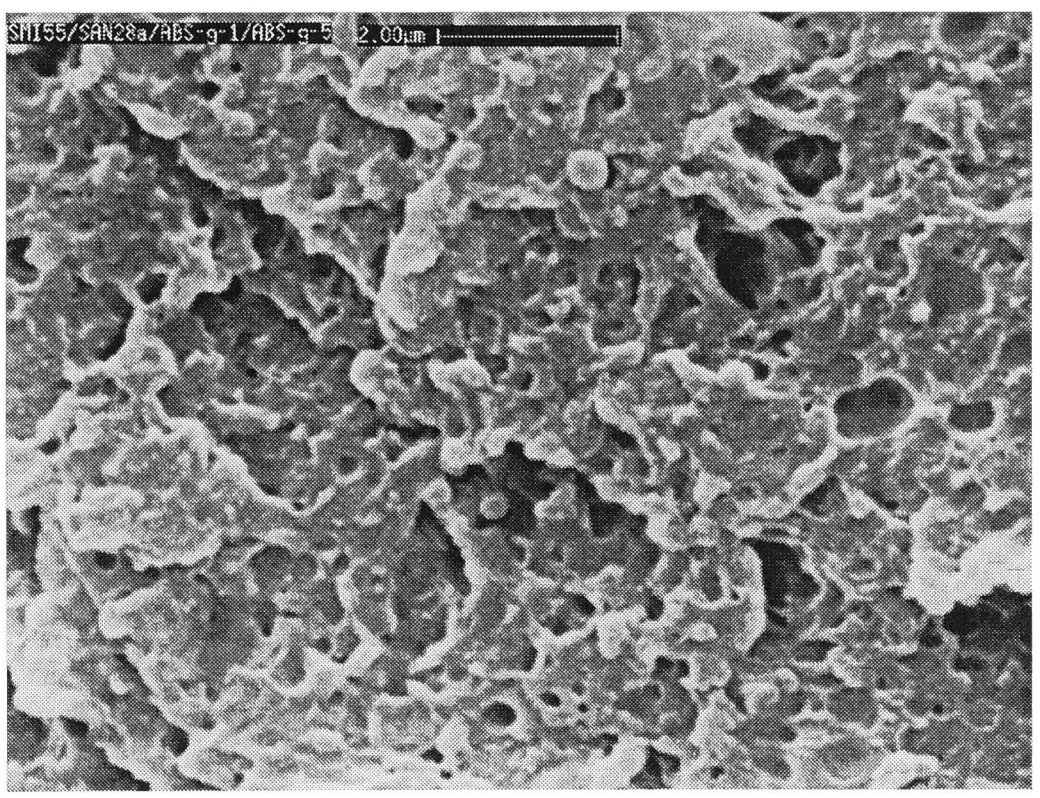

(f)

Figure 5. 5: (e) ABS15 with SAN22; and (f) ABS15 with SAN28a

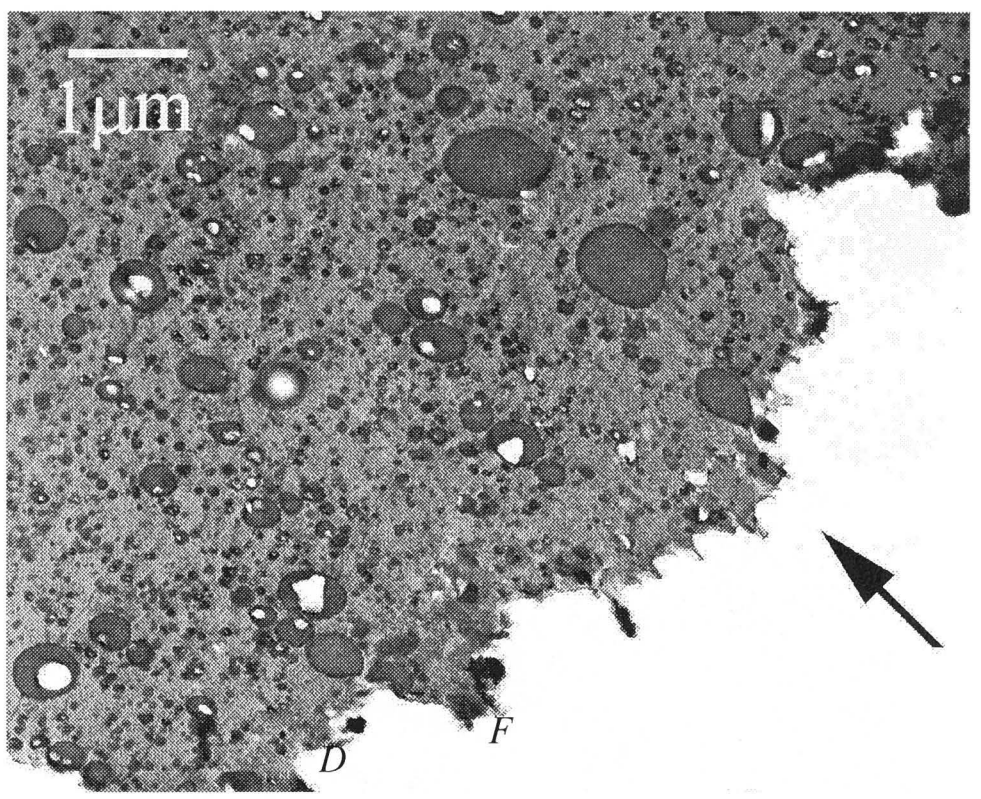

(a)

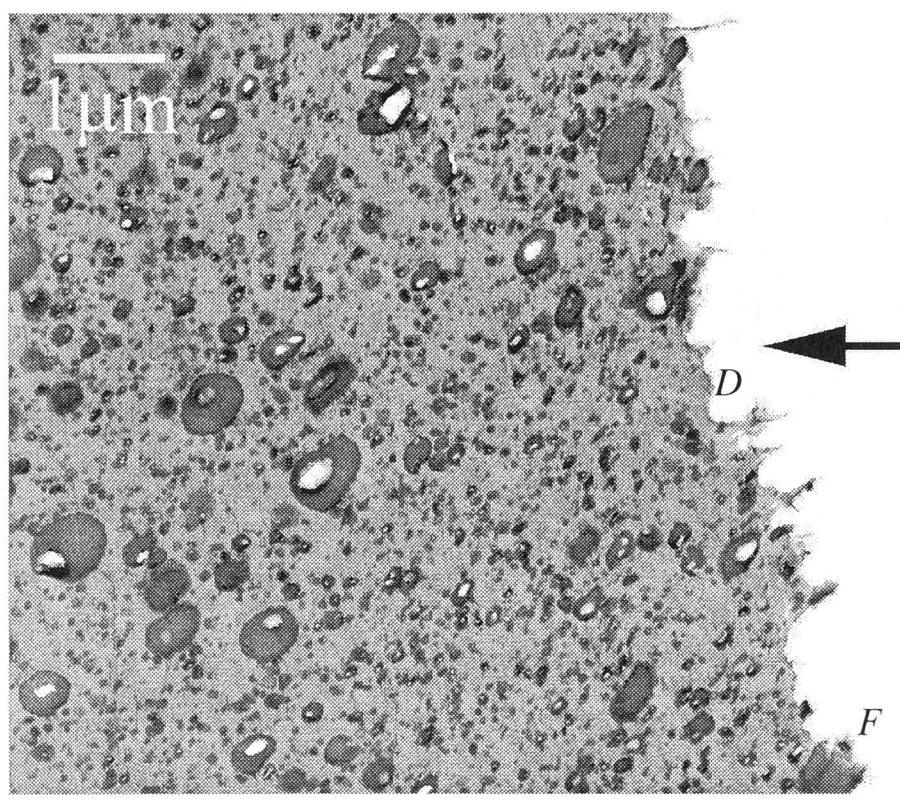

(b)

Figure 5. 6: Transmission electron microscopy of ABS under simple tension. Arrow indicates the fracture surface. Both and *F* represent debonding and fracture of rubber particles, respectively. (a) ABS1 with SAN22; (b) ABS1 with SAN28a;

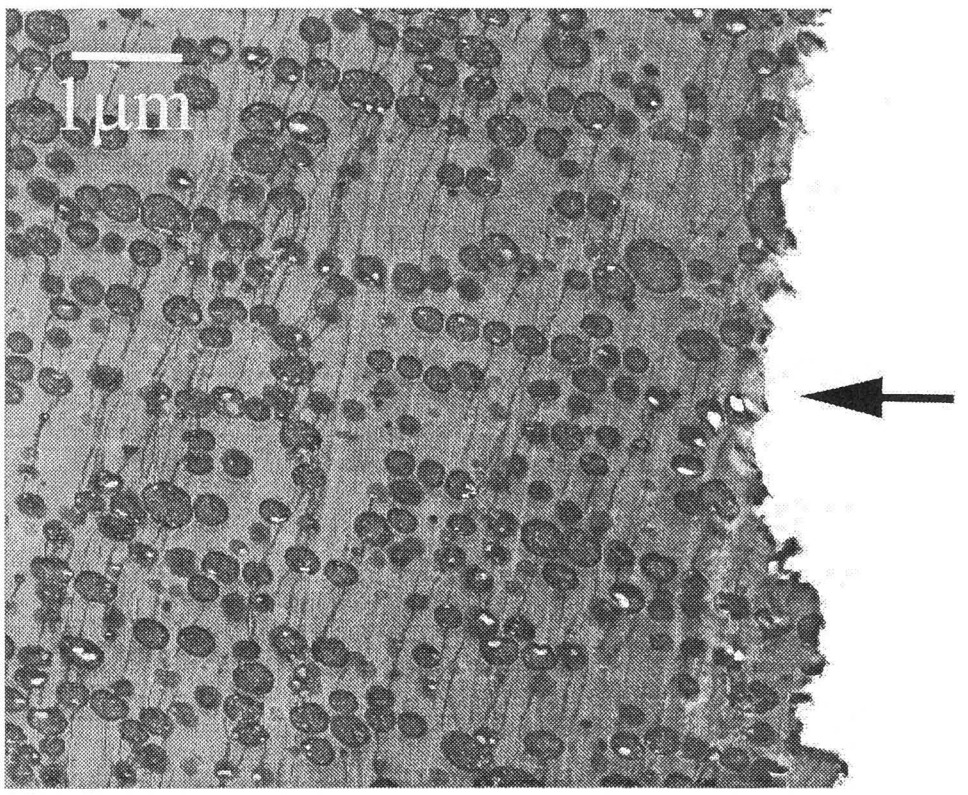

(c)

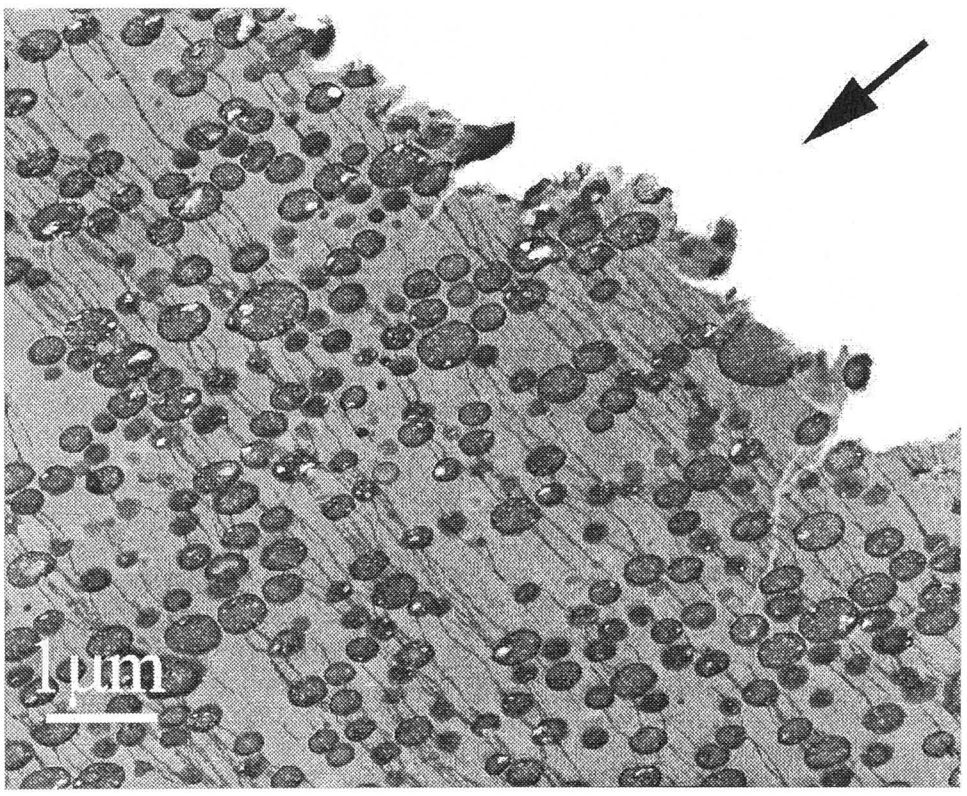

(d)

Figure 5. 6: (c) ABS5 with SAN22; (d) ABS5 with SAN28a;

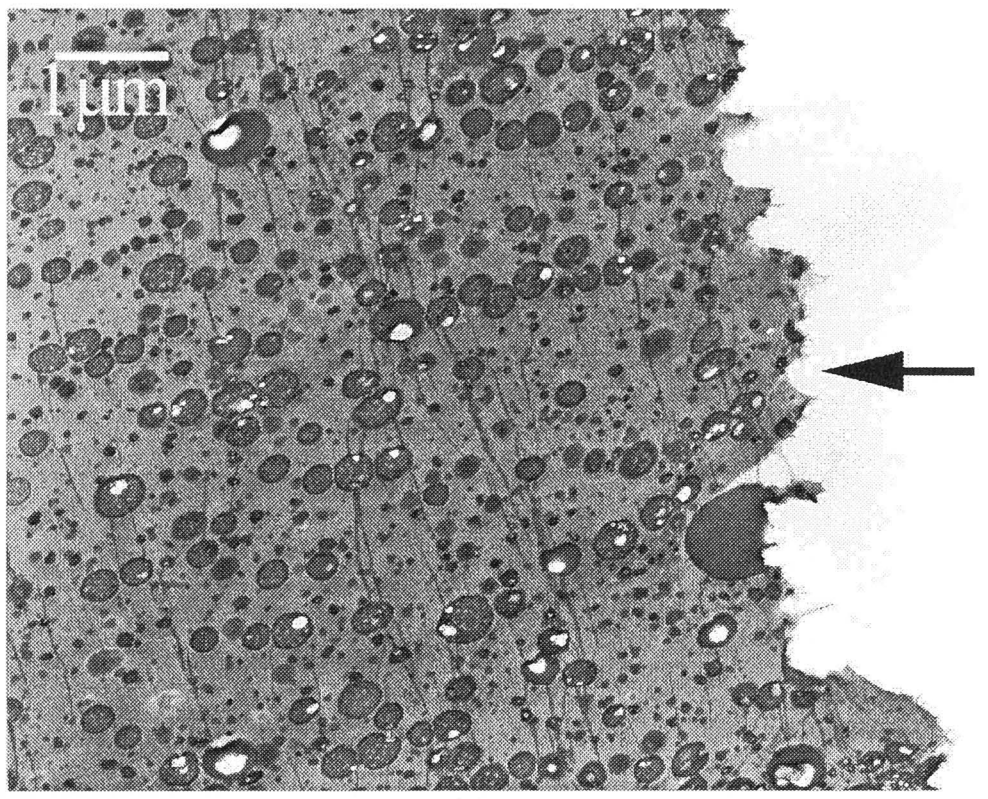

(e)

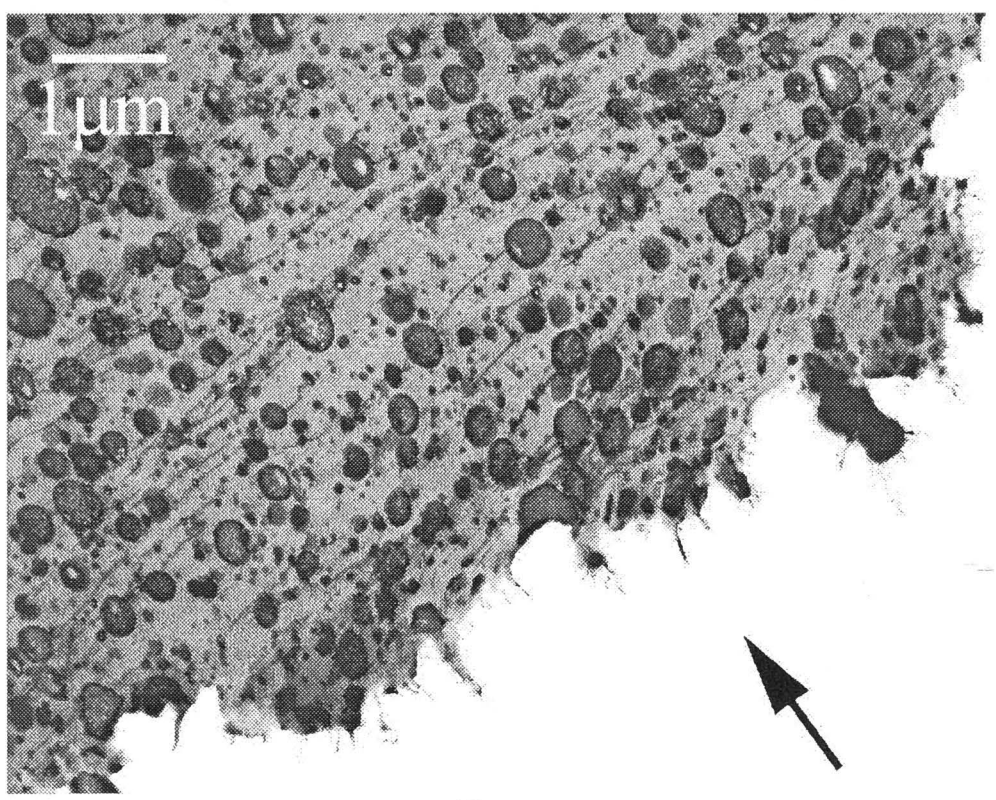

(f)

Figure 5. 6: (e) ABS15 with SAN22; and (f) ABS15 with SAN28a

surfaces of ABS5 and ABS15 in Figures 5.6(c)-(d) and Figures 5.6(e)-(f). Note also that ABS with SAN28a shows rougher fracture surfaces than ABS with SAN22.

TEM micrographs also reveal the deformation underneath the fracture surfaces. Figure 5.6 shows that crazes in ABS1 did not form readily as in ABS5. The density of crazes observed is in the order of ABS5>ABS15>ABS1, for blends with SAN22 and SAN28a constituents. Although crazes do not dominate in ABS1, particle cavitation is more extensive than in ABS5. The particle cavitation appears in both small (0.1 μm) and large (0.5 μm) particles.

Particle debonding and fracture were also observed in TEM micrographs. They correspond to those evident under SEM (see Figure 5.5) and are also labeled (*D*) and (*F*). However, these deformations were infrequent and were considered as minor energy absorption mechanisms.

SEM micrographs of SEN tensile specimens, taken near the starting notch, are shown in Figure 5.7. The micrographs did not show any difference in deformation behaviour from that of simple tensile test specimens. The main deformations observed on the fracture surface are particle debonding and particle fracture.

TEM micrographs of SEN tensile specimens are shown in Figure 5.8. The micrographs were taken near the fracture surface of the starting notch so that they correspond to SEM micrographs. Figure 5.8 shows extensive deformation in ABS1, with crazing and particle cavitation observed on the whole area covers by the micrographs. However, ABS5 and ABS15 show deformations that extent to a depth of around 3 μm from the fracture surfaces, with crazing as the major deformation and less severe particle cavitation.

The fracture surfaces of Izod impact specimens, examined under SEM, are shown in Figure 5.9. Plastic deformation is observed in the matrix of ABS1 in the form of tearing. Slight tearing can also be seen on ABS15 in Figure 5.9(f).

TEM micrographs of Izod impact specimens, shown in Figure 5.10(a)-(b), give evidence of tearing on the fracture surfaces of ABS1. Tearing, although less extensive, is also shown in ABS15, Figures 5.10(e)-(f). However, the major deformation mechanisms observed on the TEM micrographs are to be particle cavitation and crazing. The former dominates in ABS1 and ABS15; while the latter in ABS5.

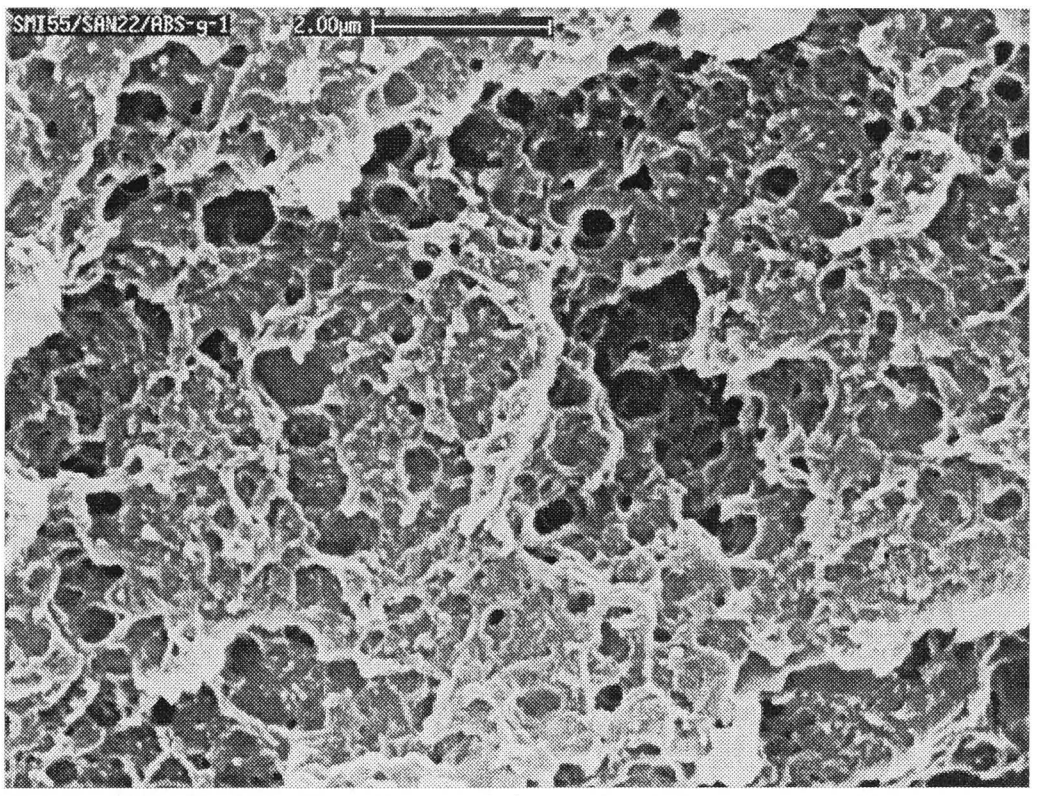

(a)

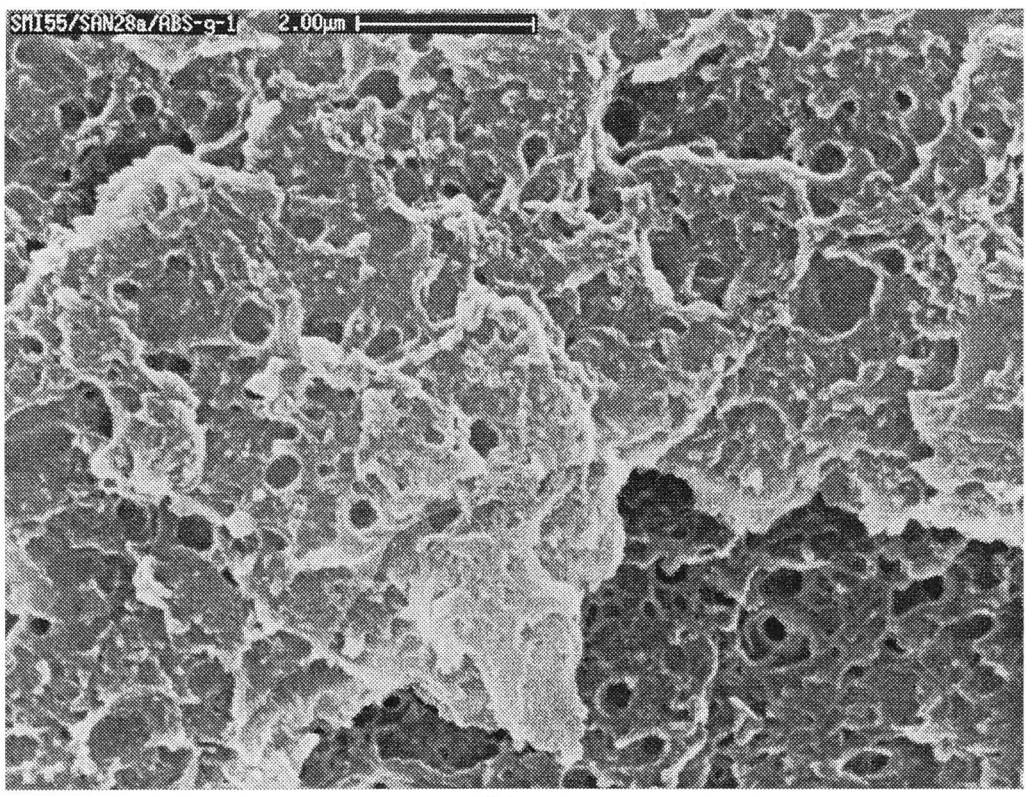

(b)

Figure 5. 7: Scanning electron micrographs of ABS under SEN tensile test. (a) ABS1 with SAN22; (b) ABS1 with SAN28a;

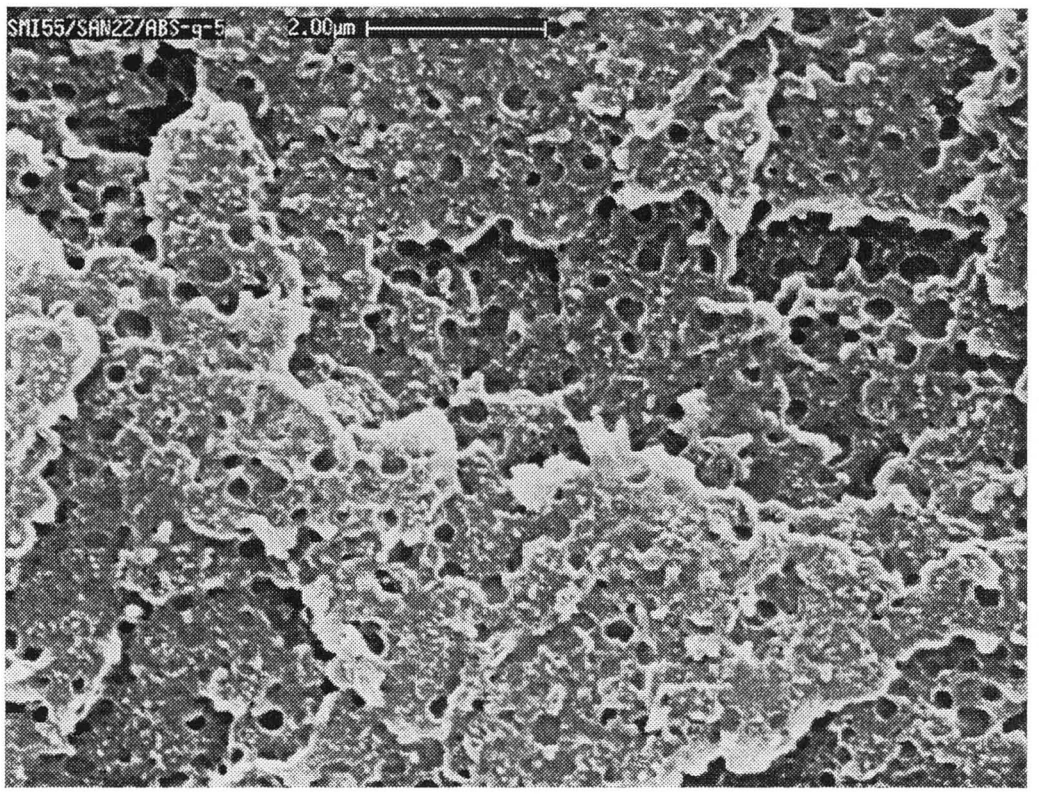

(c)

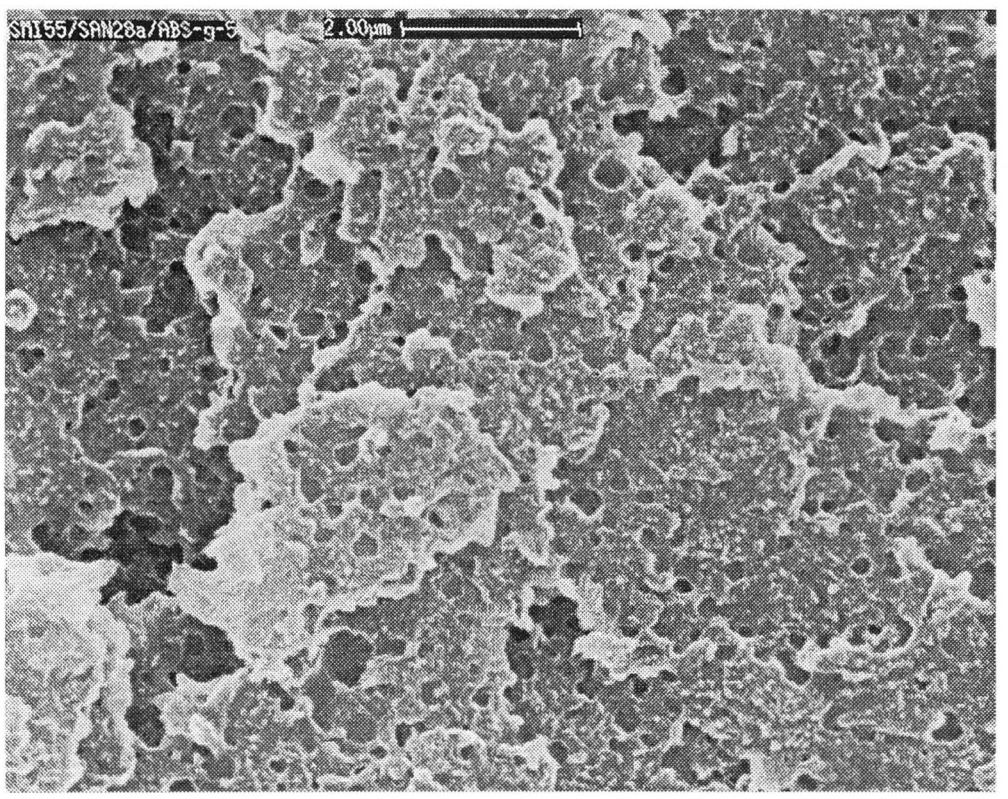

(d)

Figure 5. 7: (c) ABS5 with SAN22; (d) ABS5 with SAN28a;

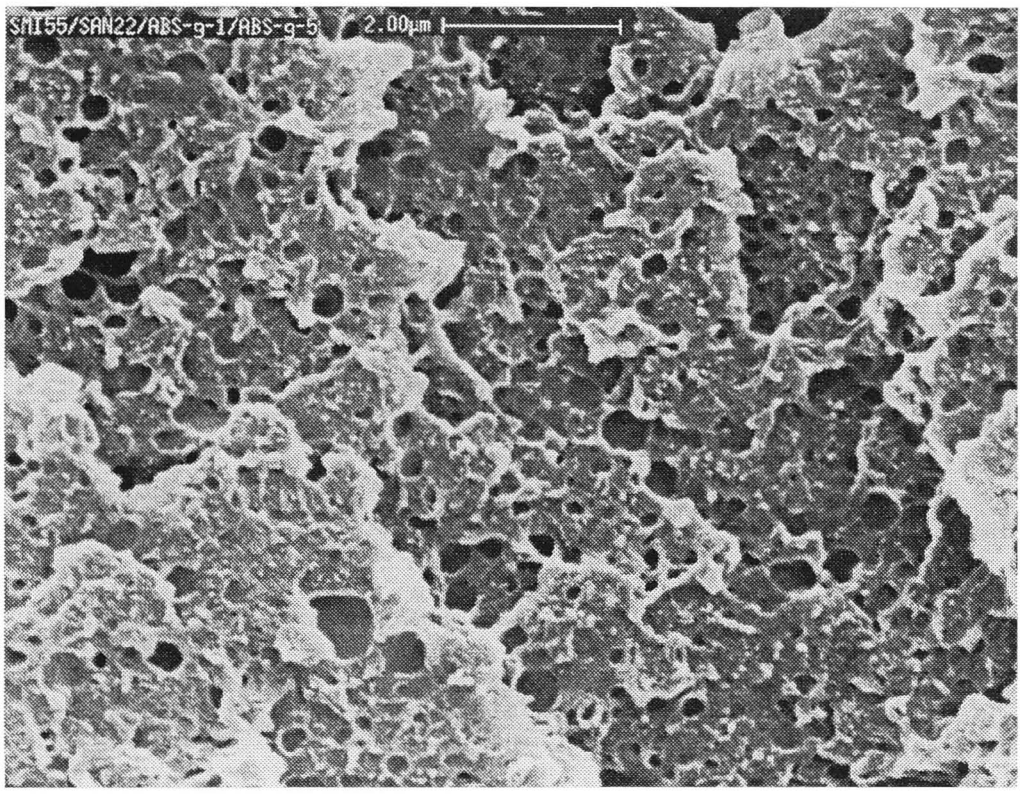

(e)

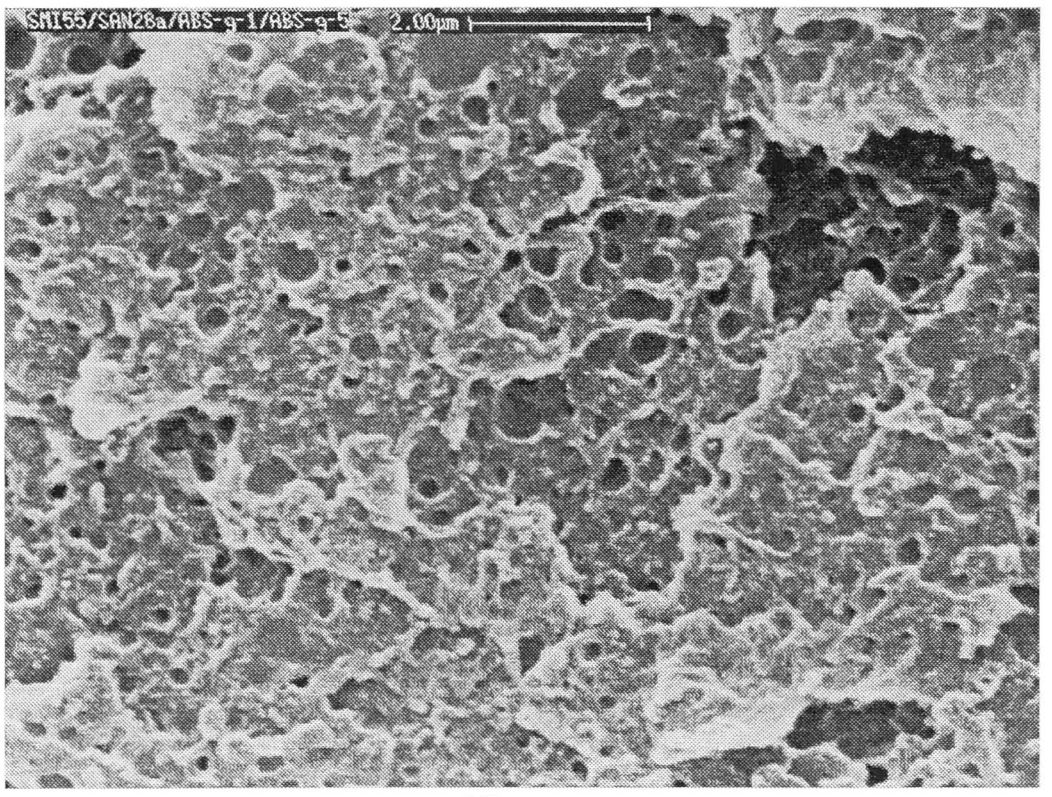

(f)

Figure 5. 7: (e) ABS15 with SAN22; and (f)ABS15 with SAN28a

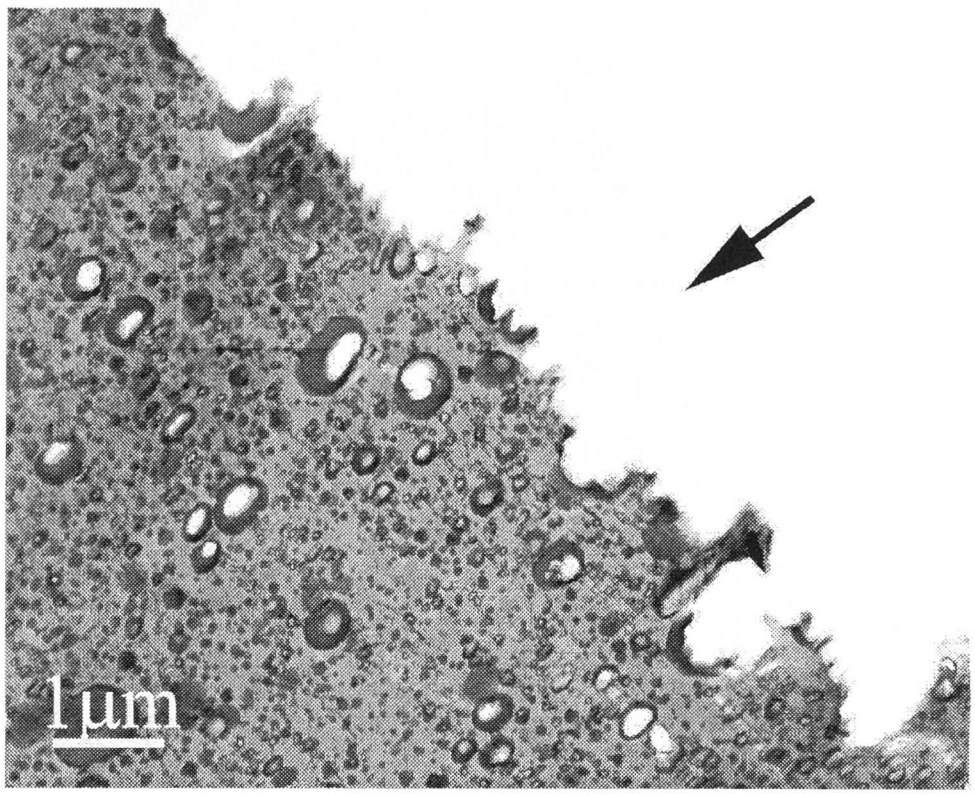

(a)

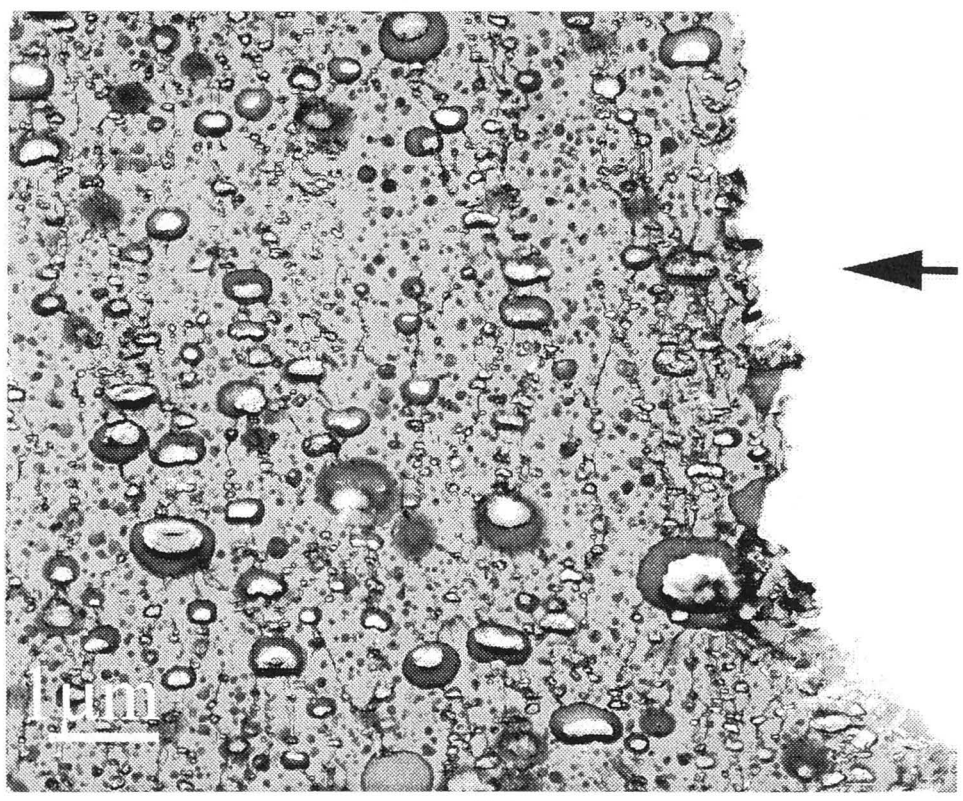

(b)

Figure 5. 8: Transmission electron micrographs of ABS under SEN tensile test. Arrow indicates the fracture surface. (a) ABS1 with SAN22; (b) ABS1 with SAN28a;

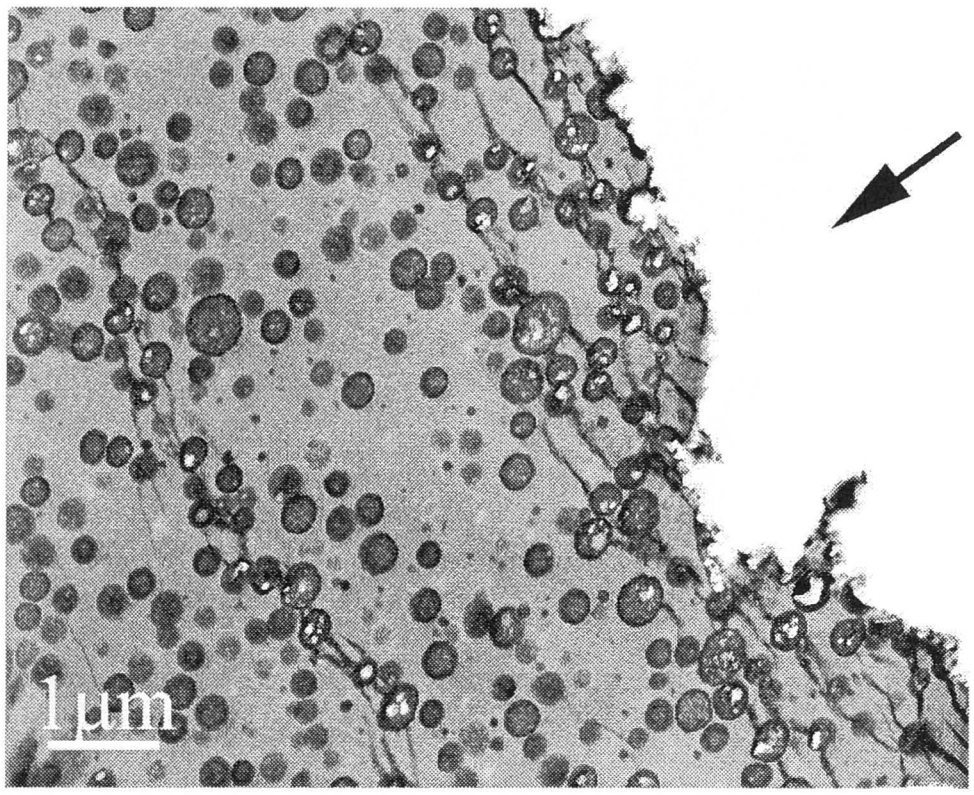

(c)

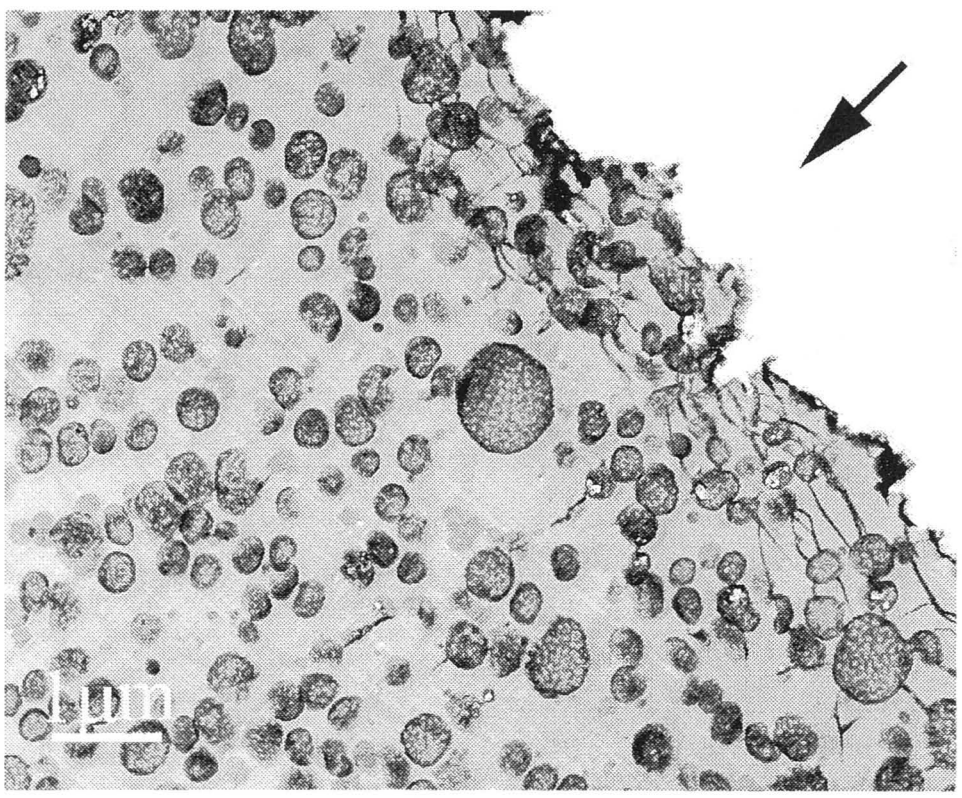

(d)

Figure 5. 8: (c) ABS5 with SAN22; (d) ABS5 with SAN28a;

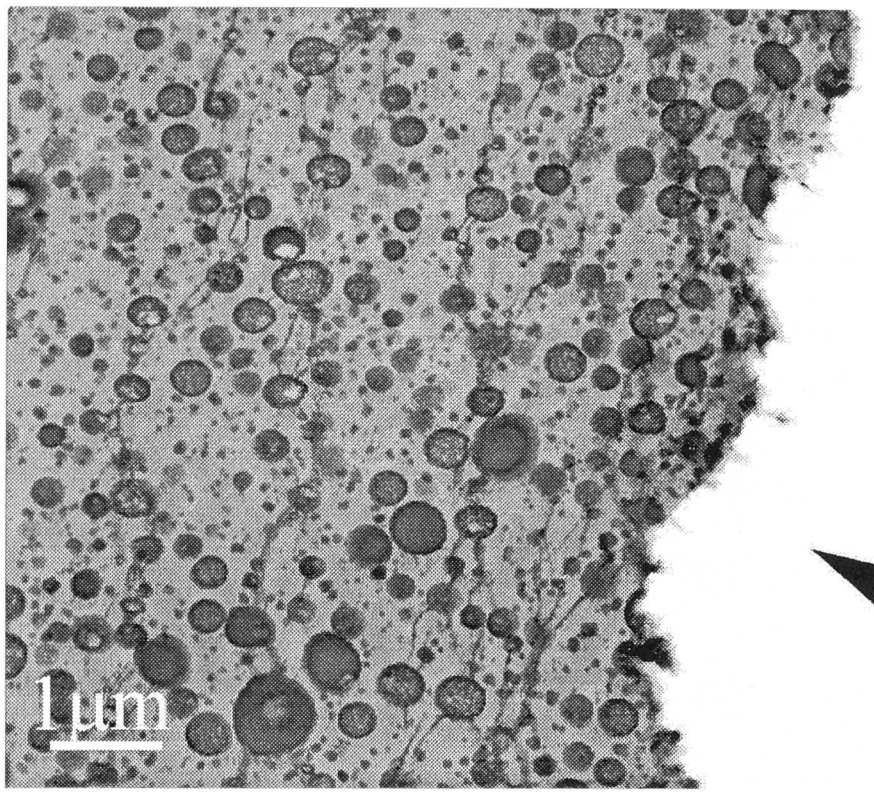

(e)

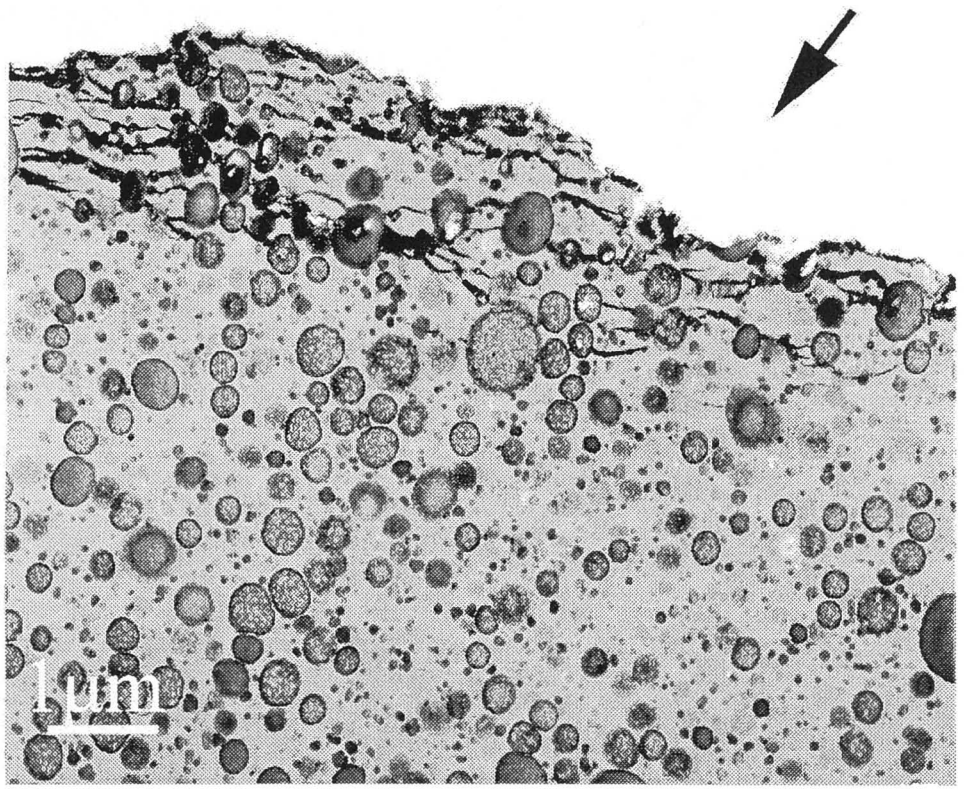

(f)

Figure 5. 8: (e) ABS15 with SAN22; and (f) ABS15 with SAN28a

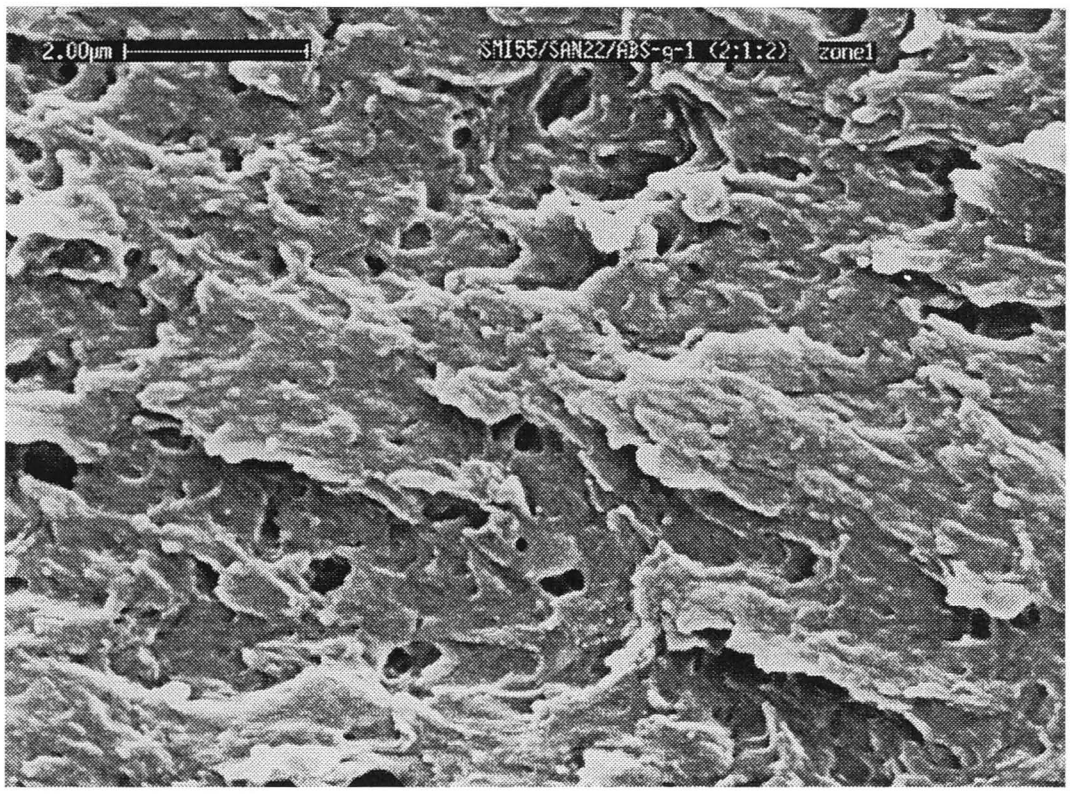

(a)

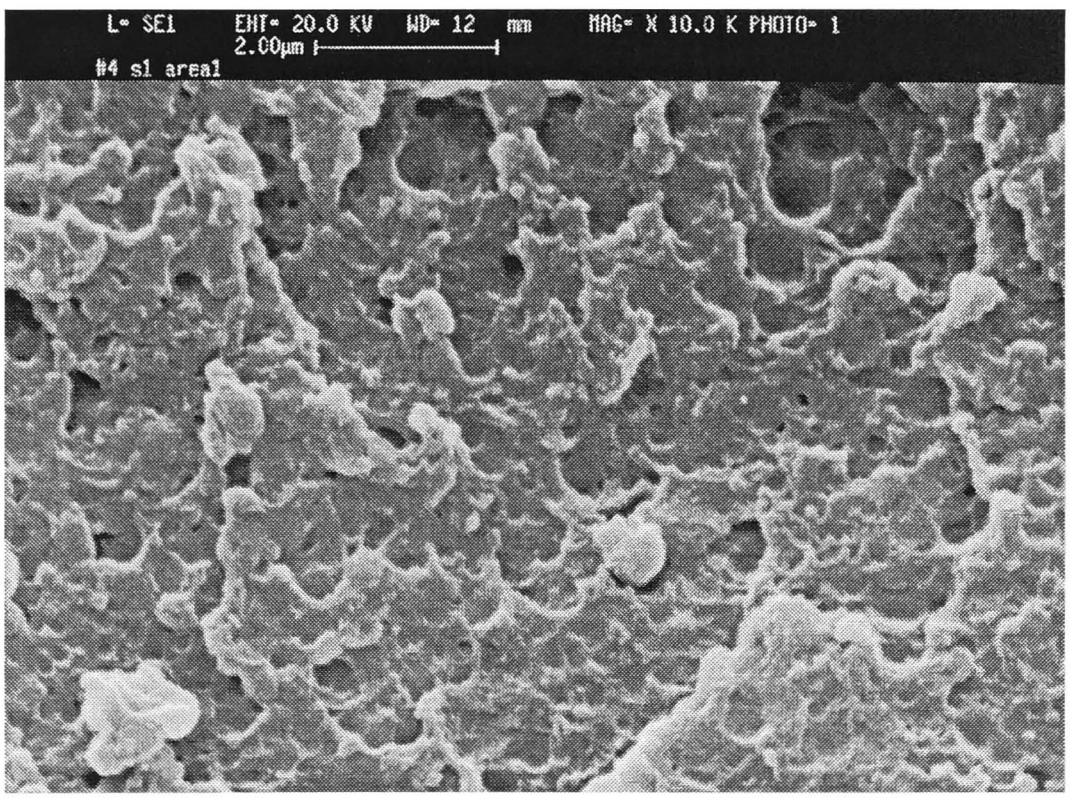

(b)

Figure 5. 9: Scanning electron micrographs on fracture surfaces of Izod specimens. (a) ABS1 with SAN22; (b) ABS1 with SAN28a;

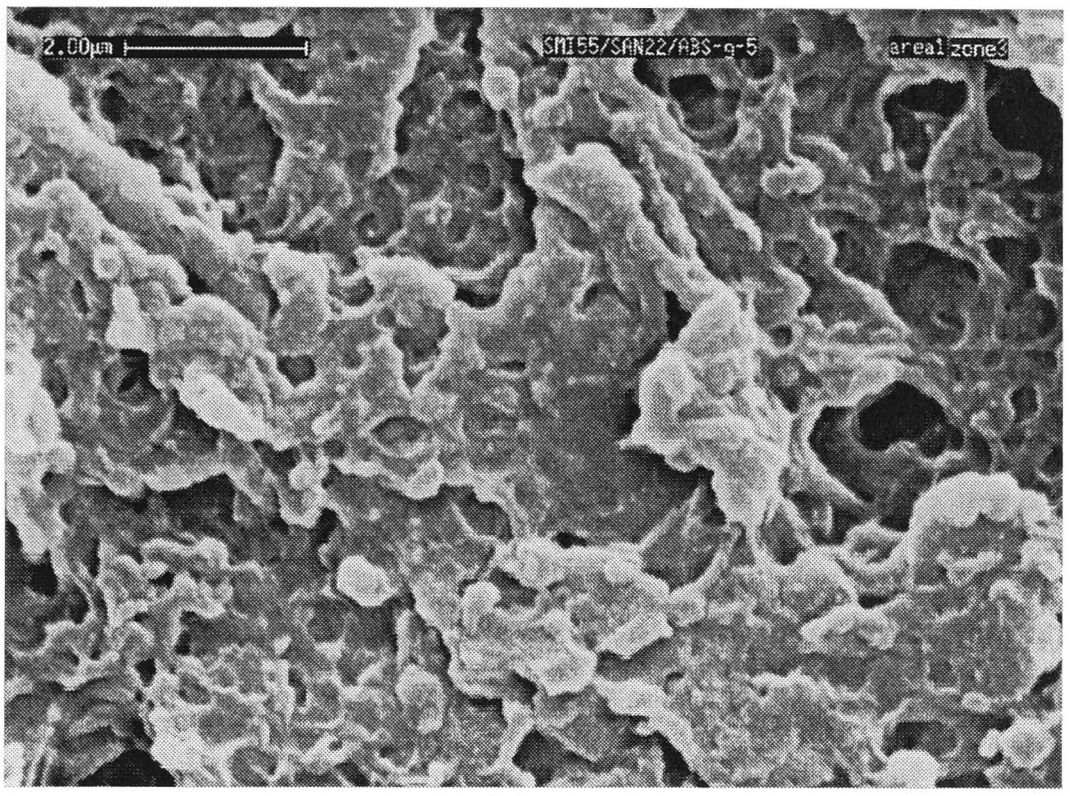

(c)

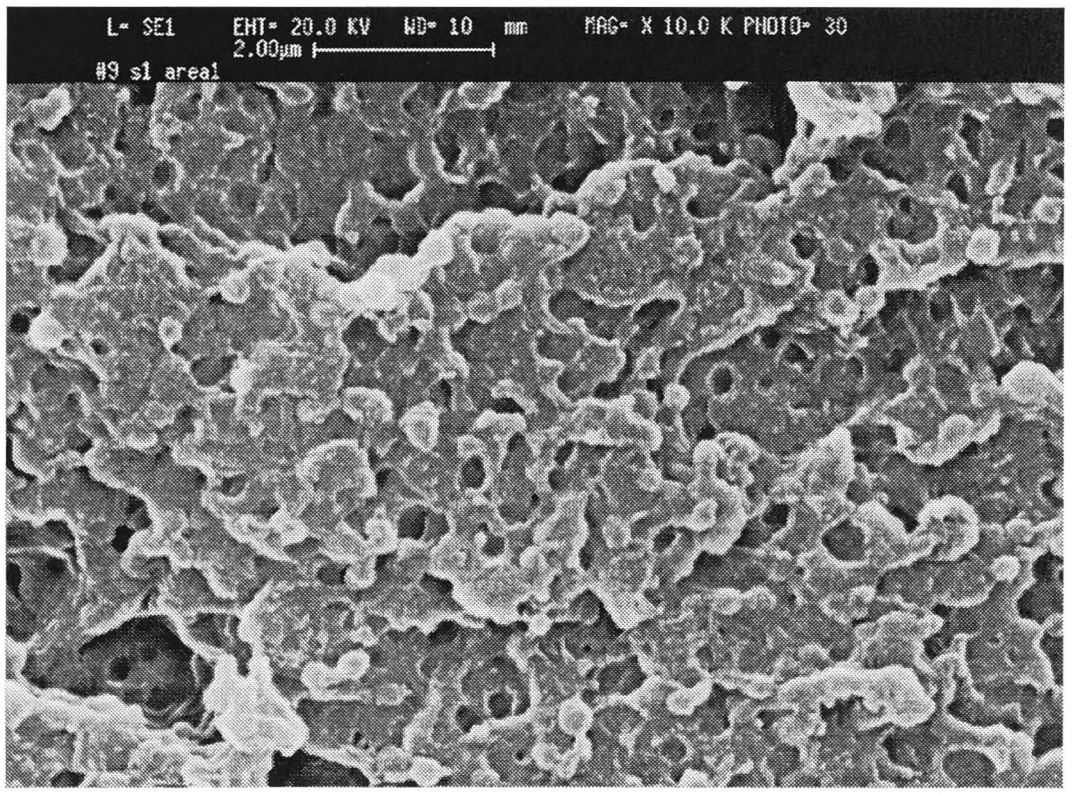

(d)

Figure 5. 9: (c) ABS5 with SAN22; (d) ABS5 with SAN28a;

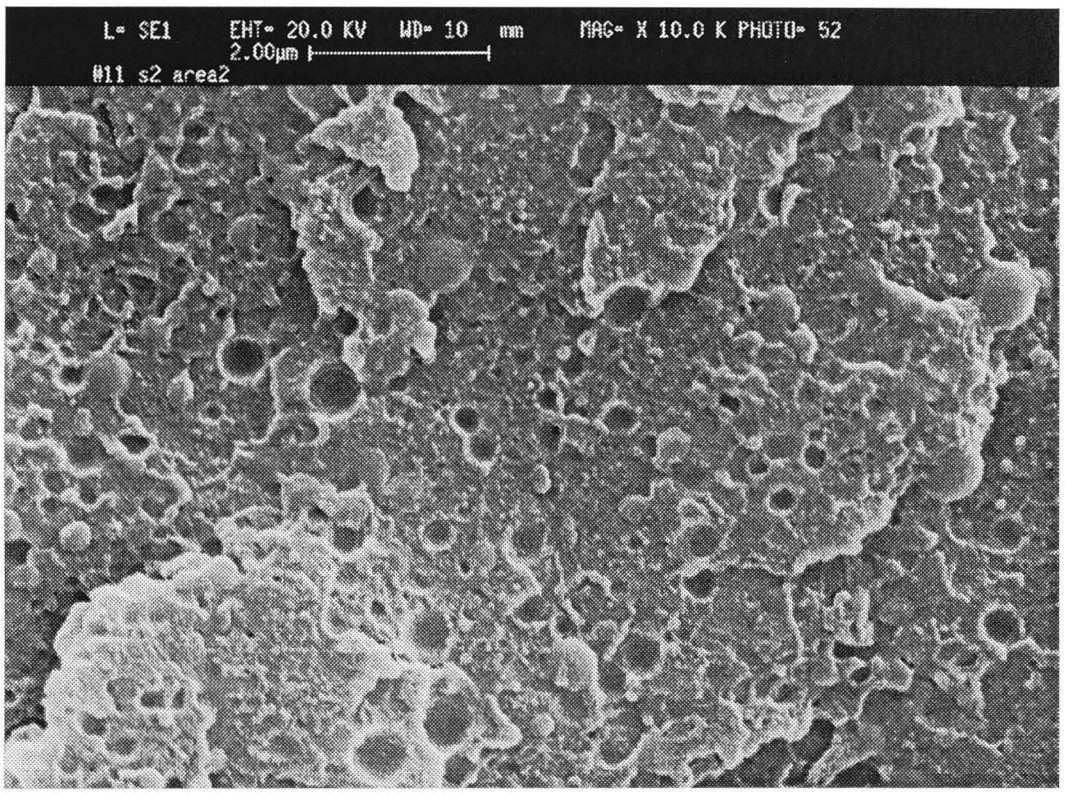

(e)

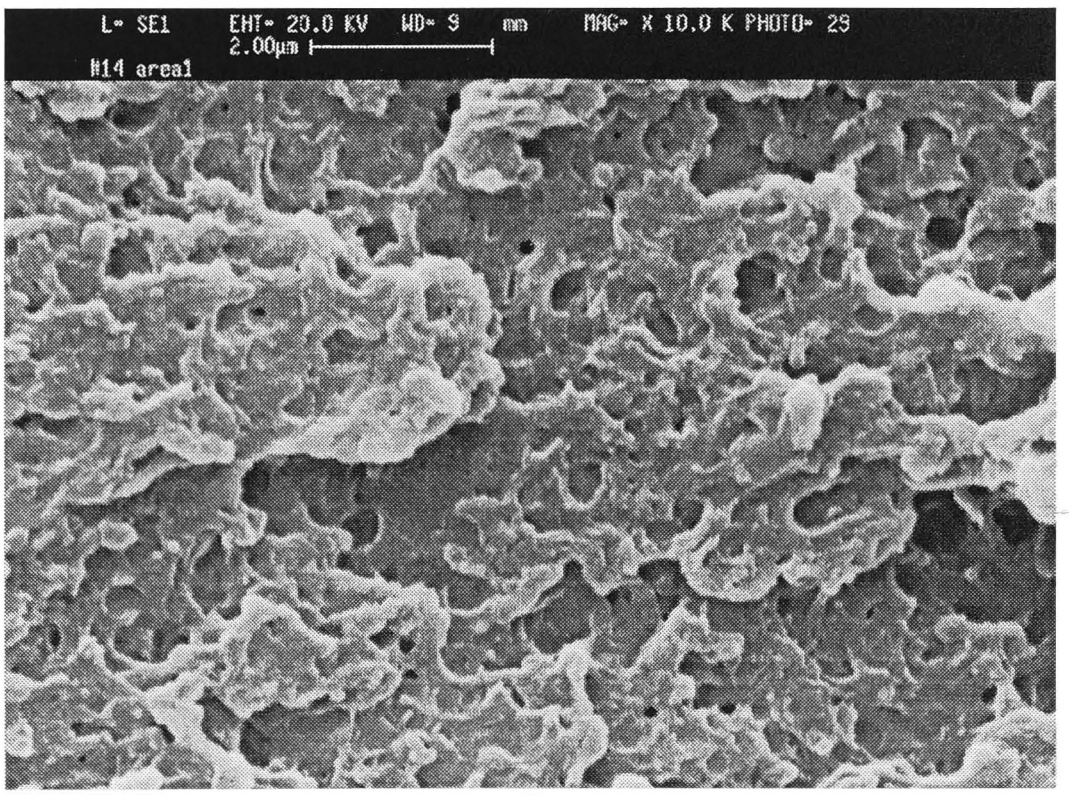

(f)

Figure 5. 9: (e) ABS15 with SAN22; and (f) ABS15 with SAN28a

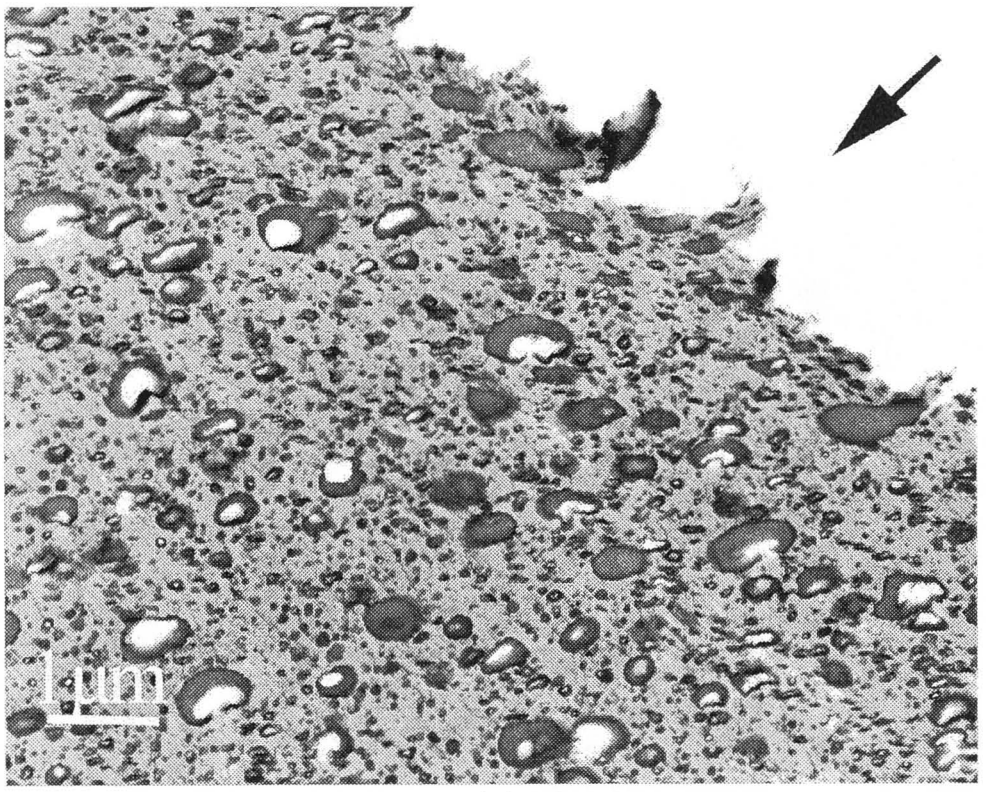

(a)

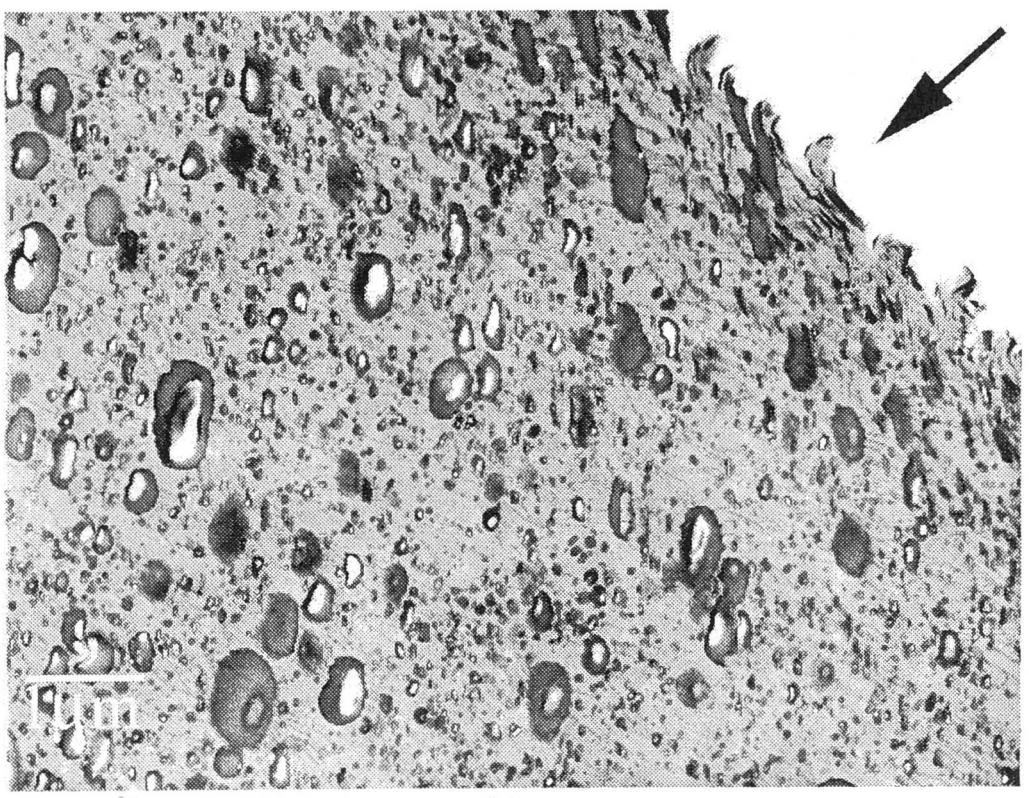

(b)

Figure 5. 10: Transmission electron micrographs of ABS under Izod impact test. (a) ABS1 with SAN22; (b) ABS1 with SAN28a;

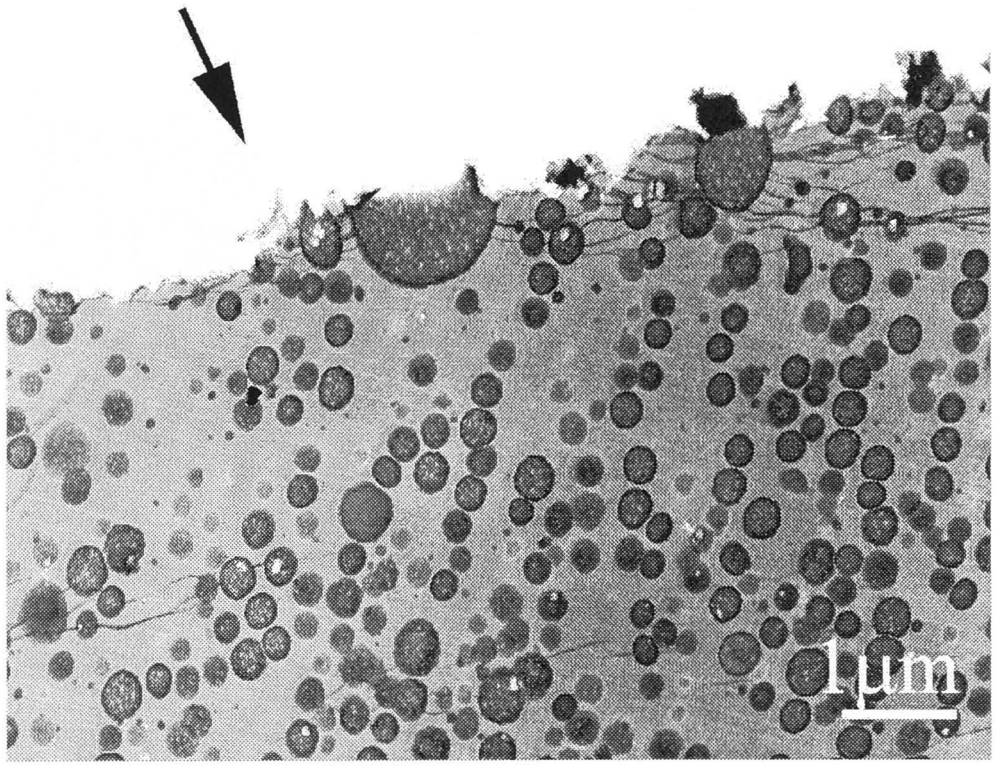

(c)

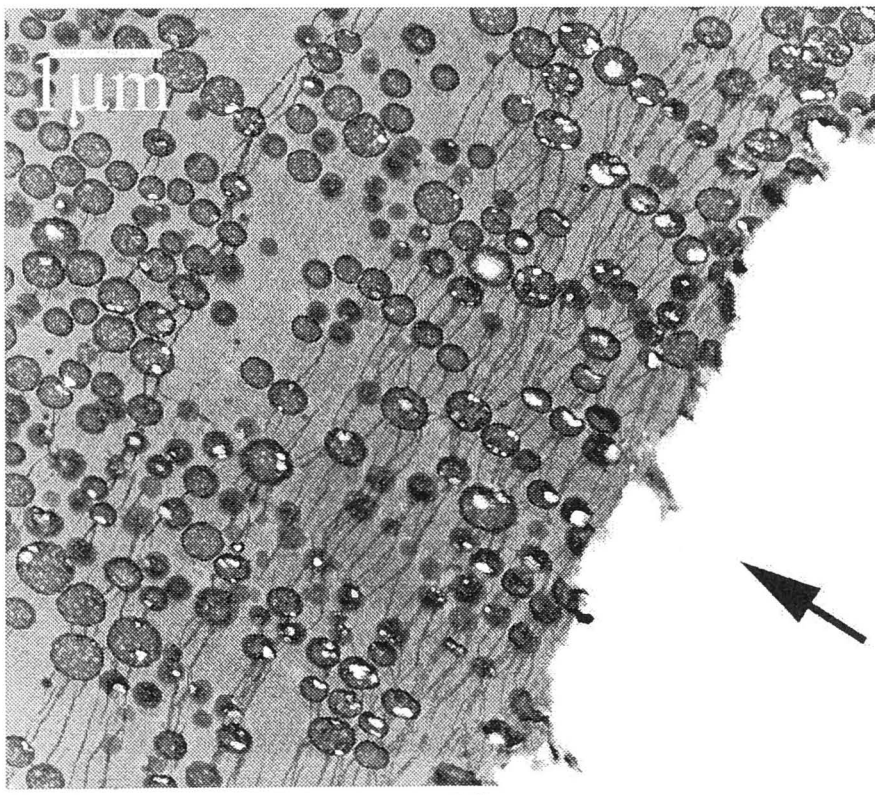

(d)

Figure 5. 10: (c) ABS5 with SAN22; (d) ABS5 with SAN28a;

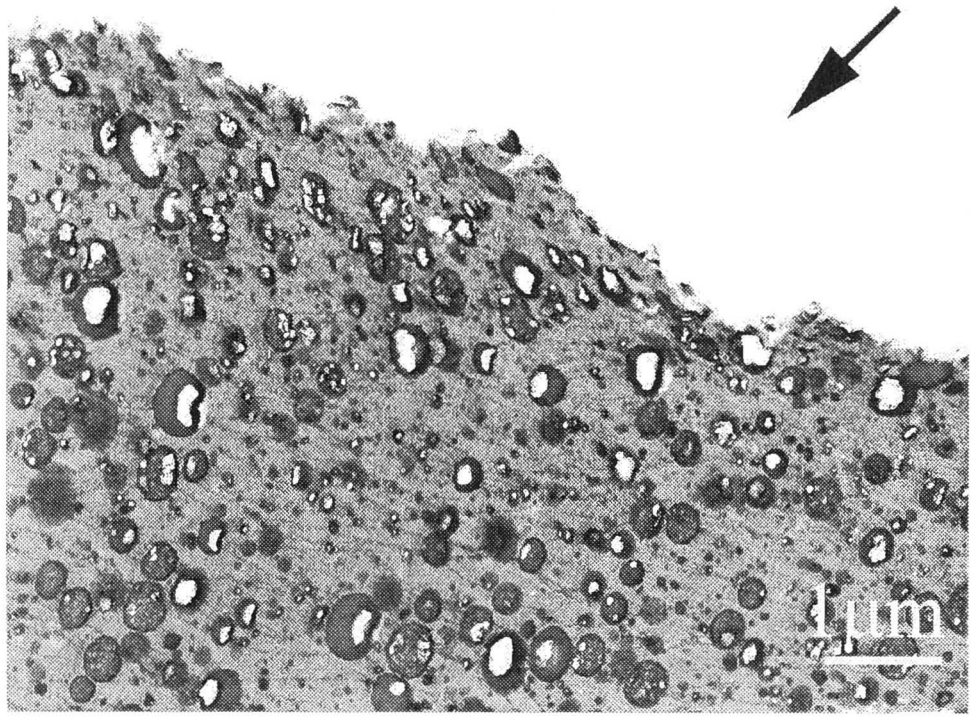

(e)

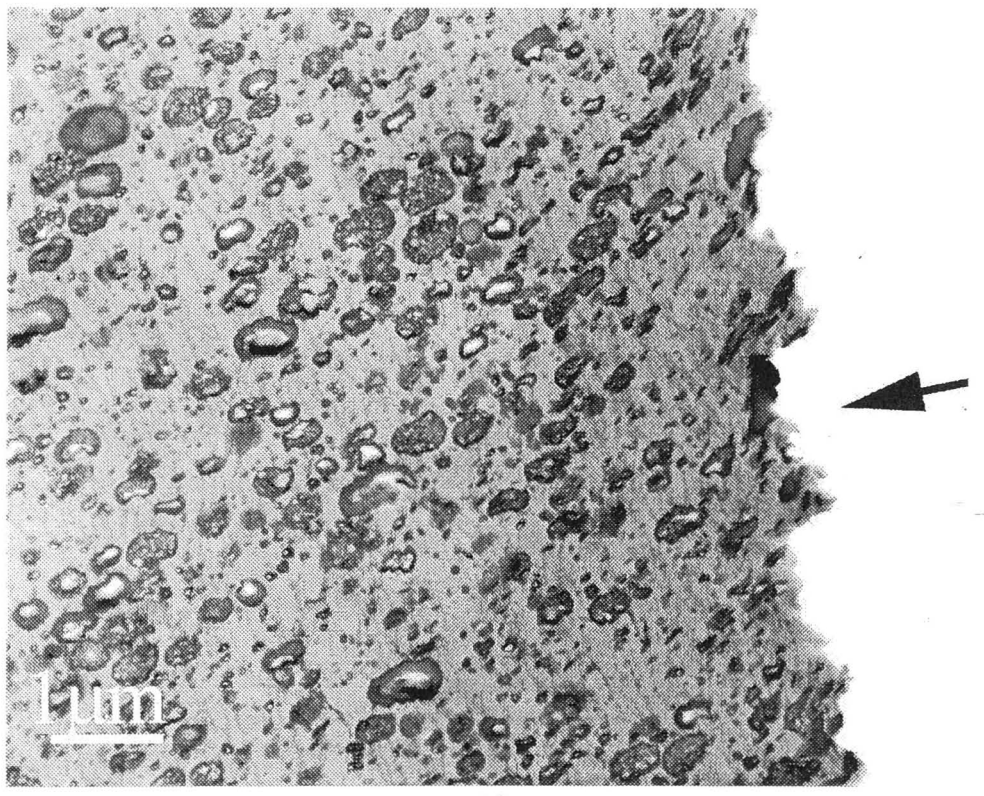

(f)

Figure 5. 10: (e) ABS15 with SAN22; and (f) ABS15 with SAN28a

5.3.3 Small angle X-ray scattering (SAXS)

SAXS was used to verify deformation types present in the ABS's. Two kinds of SAXS patterns from the ABS's are shown in Figure 5.11: circular and rhombus-shaped. The former was obtained from an ABS1 specimen and the latter from an ABS5 specimen. Both specimens consisted of SAN28a constituents and their TEM analyses are shown in Figures 5.6(b) and 5.6(d).

Figure 5.11(a) shows that overexposure of the X-ray beam did not cause the rhombus pattern. It shows that the rhombus shape does not change with the exposure time at *location 2*, thus confirming that the rhombus pattern was caused by true deformation of the specimen.

SAXS examination of simple tensile specimens in Figure 5.12 shows a rhombus pattern in ABS1 and circular patterns in ABS5 and ABS15. The same SAXS patterns were observed in Izod impact specimens for both ABS1 and ABS15 (see Figure 5.13). The extent of the deformation in ABS1 with SAN22 was extended to *location 3* in Figure 5.13(a).

5.4 Crazing and shear deformations examined by small angle X-ray scattering (SAXS)

Early work by Okamoto et al.[83] showed that the *in situ* SAXS pattern for crazing consists of a pair of streaks parallel to the crazes and that for shear yielding, a pair of streaks perpendicular to the crazes. After the load is removed the intensity of the streaks is drastically reduced as shown by Brown and Kramer[92]. A small compressive force will even make the streaks disappear. Specimens used in the SAXS work were after loading was removed, therefore the craze diffraction pattern is expected to be different to that of Okamoto's.

The SAXS patterns in Figures 5.12 and Figure 5.13 are used to correlate to the deformation behaviour revealed by TEM micrographs in Figure 5.6 and Figure 5.10. The SAXS pattern at *location 2* of the sample was used for the comparison unless otherwise stated.

The circular SAXS patterns of ABS5 and ABS15 indicate from the TEM micrographs that the mechanism involved is crazing. However, the rhombus pattern in ABS1 was not crazing. The other deformation that could occur in ABS is shear

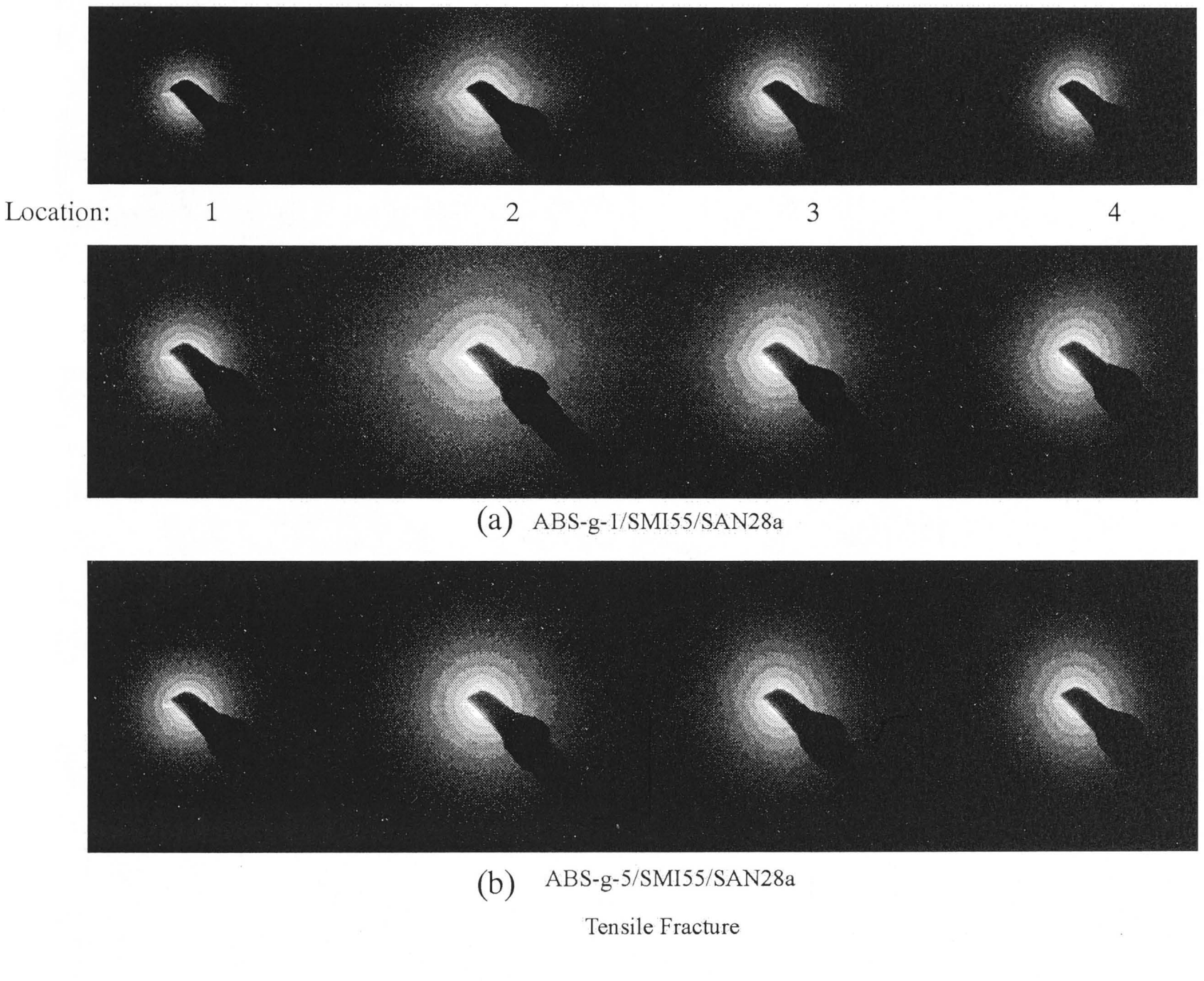

Figure 5. 11: Small angle X-ray scattering patterns representing different deformation behaviours, taken at different locations. (a) rhombus pattern for ABS1 at different exposure times; (b) circular pattern for ABS5 (courtesy of Jar)

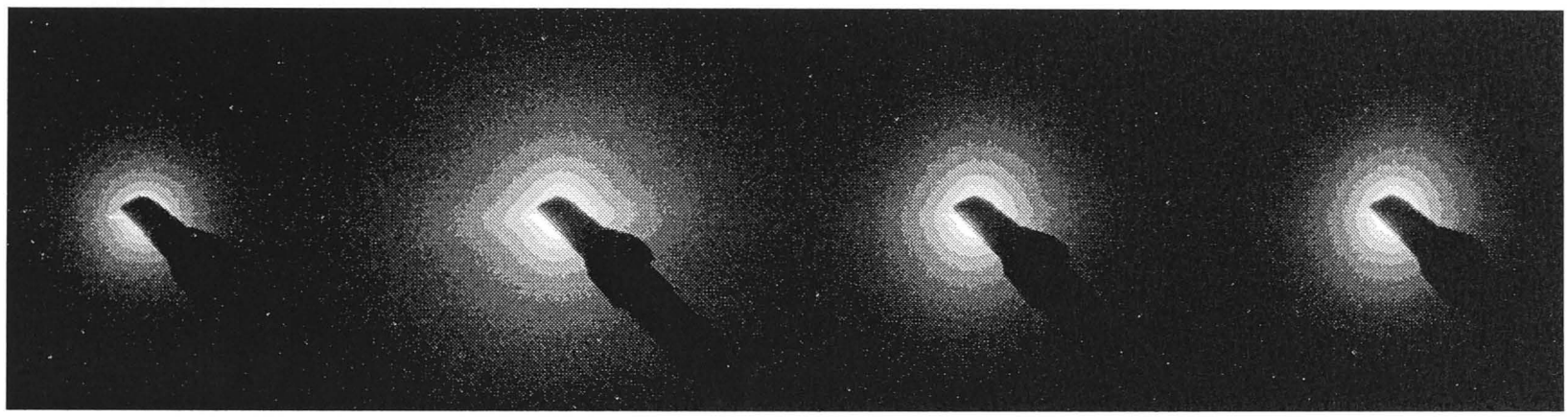

(a) ABS-g-1/SMI55/SAN28a

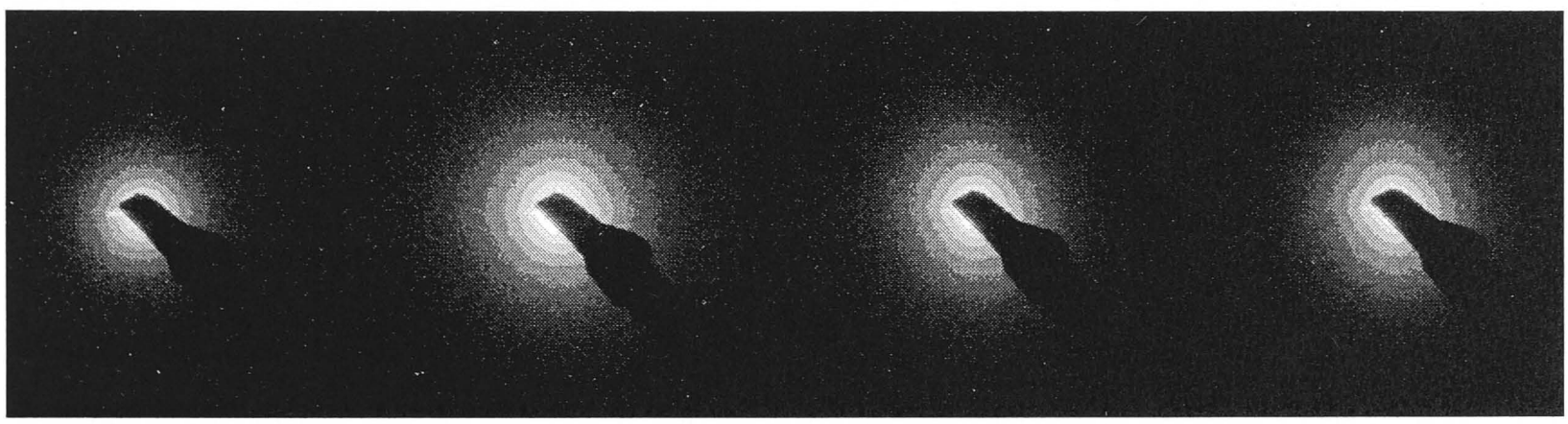

(b) ABS-g-5/SMI55/SAN28a

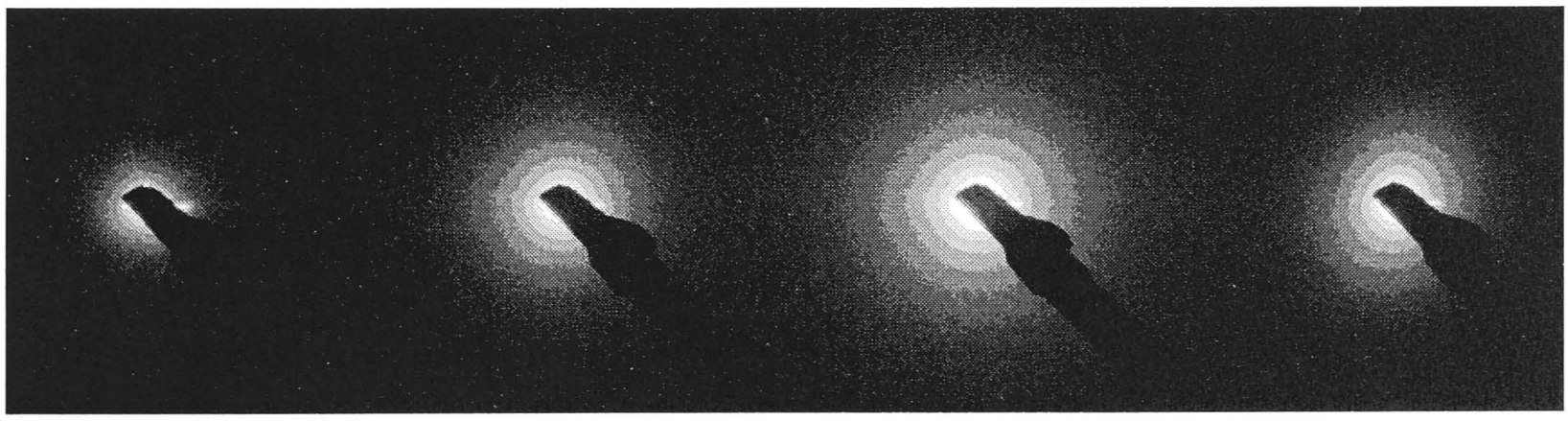

(c) ABS-g-1/ABS-g-5/SMI55/SAN28a

Tensile Fracture

Figure 5. 12: Small angle X-ray scattering of ABS with SAN28a under simple tensile test. (a) ABS1 with SAN28a; (b) ABS5 with SAN28a; and (c) ABS15 with SAN28a (courtesy of Jar)

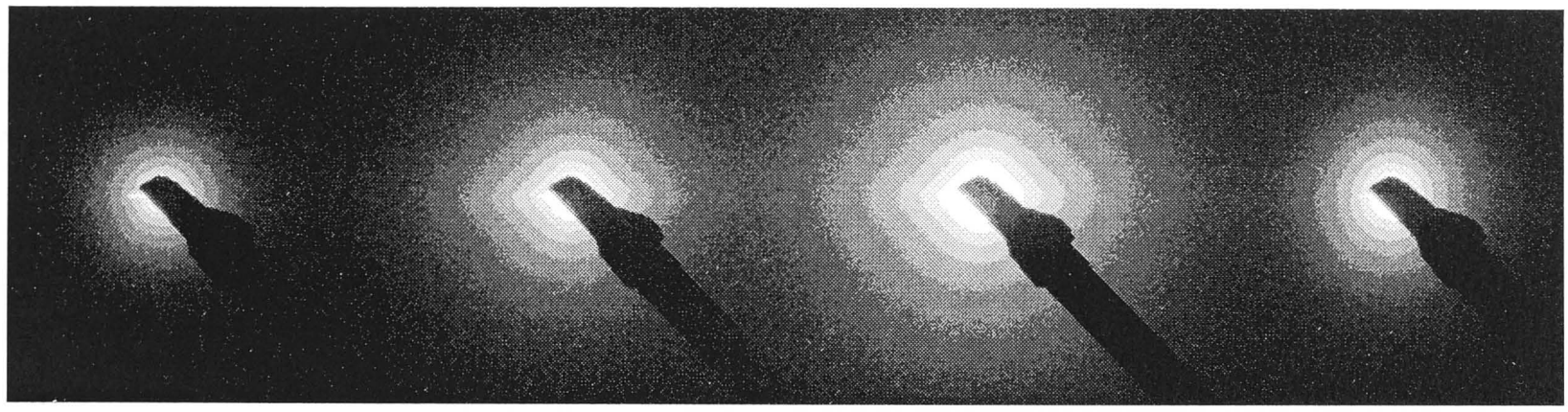

(a) ABS-g-1/SMI55/SAN22

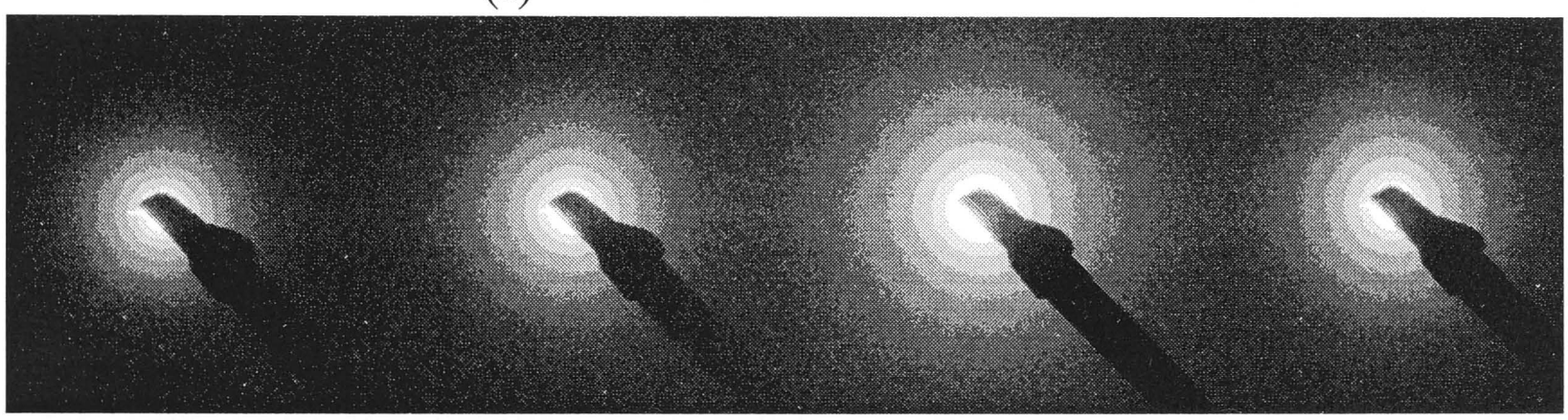

(b) ABS-g-5/SMI55/SAN22

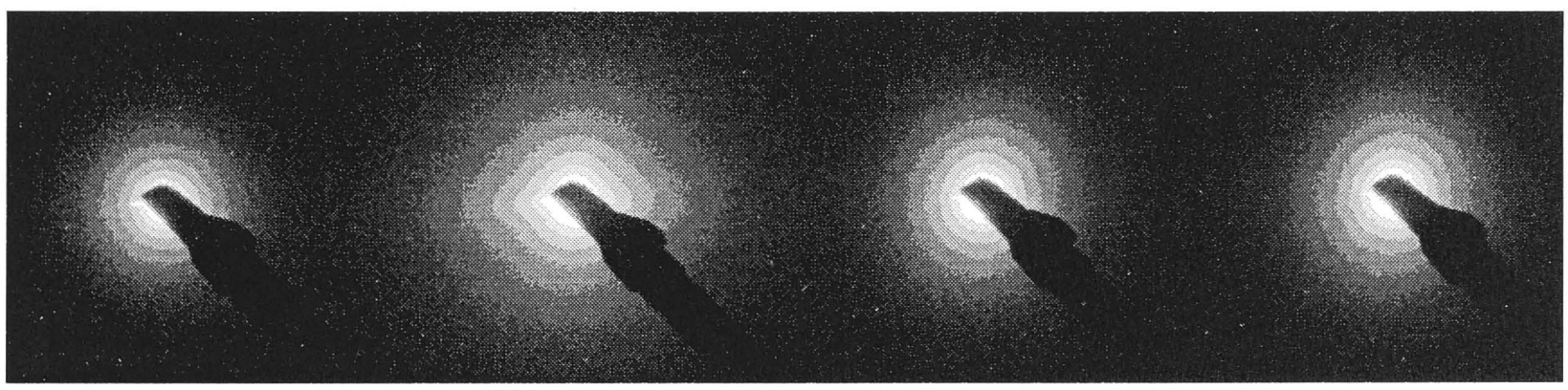

(c) ABS-g-1/SMI55/SAN28a

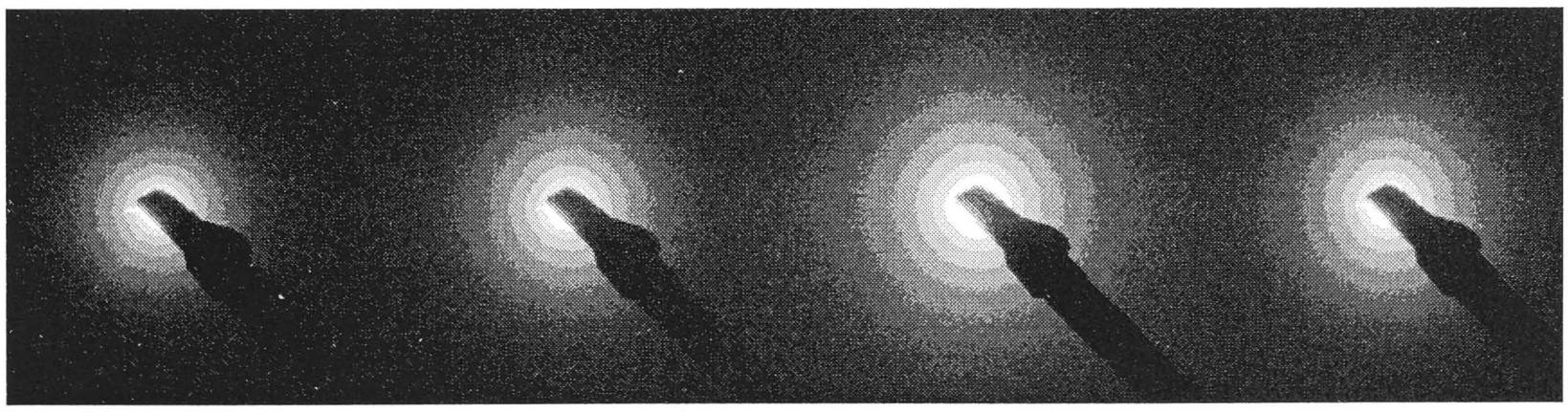

(d) ABS-g-5/SMI55/SAN28a

Izod Impact

Figure 5. 13: Small angle X-ray scattering of ABS under Izod impact test. (a) ABS1 with SAN22; (b) ABS5 with SAN22; (c) ABS1 with SAN28a; and (d) ABS5 with SAN28a (courtesy of Jar)

yielding[25, 93]. Particle cavitation was eliminated as a cause of the rhombus SAXS pattern because ABS5 with SAN28a (see Figure 5.10(d)) shows extensive particle cavitation, but does not show rhombus pattern (see Figure 5.13(d)) under SAXS. It is therefore believed that shear yielding, which could have occur in a polymeric material and could not be observed by electron microscopy, is present in ABS1 material.

It is therefore concluded that crazing dominates the deformation behaviour in ABS5 and ABS15 materials and shear yielding dominates in ABS1. This would explain the mechanical results shown in Figure 5.2 and Figure 5.3, that ABS15 material has toughness closer to ABS5 material because both have crazing as the major deformation mechanism.

5.5 The effects of acrylonitrile (AN) content

The effect of AN content on the mechanical properties of the materials was discussed in Chapter 4. The present chapter goes further to show the effect of AN content in term of compatibility among the constituents of the blends.

The mechanical test results in Figures 5.2-5.4 show an increase in toughness with the increase in AN content. This trend was similar to that observed in pure SMI/SAN blends in Chapter 4. The increase of toughness with AN content is attributed to the inherent ductility of the polymeric matrix in the ABS's. As in the previous chapter, these mechanical properties could be masked by a *high* strain rate, shown in Figure 5.4(b). However, the addition of rubber particles could assist in magnifying the effect of AN content under higher strain rate, as observed in Figures 5.4(a) and 5.4(c).

Another cause of the toughness increase with AN content of the ABS's is the AN content mismatch. Each of the ABS's consists of two SANs of different AN content; matrix SAN (SAN_m) and grafted SAN (SAN_{ABS}). Early study by Quintens et al.[60] on one-SAN-system showed that AN content could affect miscibility in PC/SAN blends. They have shown that AN content of 24 wt% and 29wt% (from a set of 0–34 wt%) gave PC/SAN blends better mechanical properties. This was attributed to the finer morphologies exhibited in these blends. Blends containing two types of SAN were studied by Molau[55], who proposed that the separation of grafted SAN (SAN_g) and SAN_m occurred when AN content difference reaches 4-5 wt%. This immiscibility between the SANs could reduce the toughness of the blends.

The miscibility of two SANs in ABS systems, due to AN content mismatch, was studied by Kim et al.[29, 30]. They showed that a slight offset in miscibility provides the best toughness. They attributed the high toughness to particle agglomeration, caused by AN content mismatch, as shown in Figure 5.14, reprinted from Kim et al.[29] They have shown that at AN content mismatch of 11.5 wt% could cause significant particle agglomeration.

Other factors that can affect rubber particle agglomeration are particle size, degree of rubber content, molecular weight, and the grafting level between SAN_m and the particles[27, 28, 94, 95].

In this study, the grafted SAN (SAN_{ABS}) has an acrylonitrile level of 23.0 wt%. The effect of AN content mismatch between grafted SAN and matrix SAN is shown in Table 5.1. The AN content mismatch is not significant. Our results as seen by comparison of Figures 5.14 and 5.15, do not support those reported by Kim and Chang[29, 30, 95], although the AN content mismatch was relatively small to cause severe particle agglomeration. Kim and Chang have suggested that the slight AN content mismatch, which induces the rubber particle agglomeration, improves mechanical toughness of the materials.

Table 5. 1: Acrylonitrile (AN) content mismatch between matrix SAN and grafted SAN

SAN_x	AN content in SAN_m (wt%)	AN content in SAN_g (wt%)	AN content mismatch (wt%)
SAN22	23.6	23	0.6
SAN25	24.6	23	1.6
SAN26	25.4	23	2.4
SAN28a	28.9	23	5.9

5.6 The effect of particle type

The addition of rubbery particles into glassy polymers can enhance the capacity of the glassy matrix for energy absorption. Variation in particle size, rubber content, and grafting ratio present are just a few of many parameters affecting the toughness of the materials.

This section will show that rubber particle type has an impact on toughness, as well as on the deformation behaviours. First of all, the particle size used in ABS1 and ABS5 was different. Particle size was noticed to have an influence in high impact polystyrene (HIPS) by Bucknall and Donald[96, 97], who suggested that a particle size of

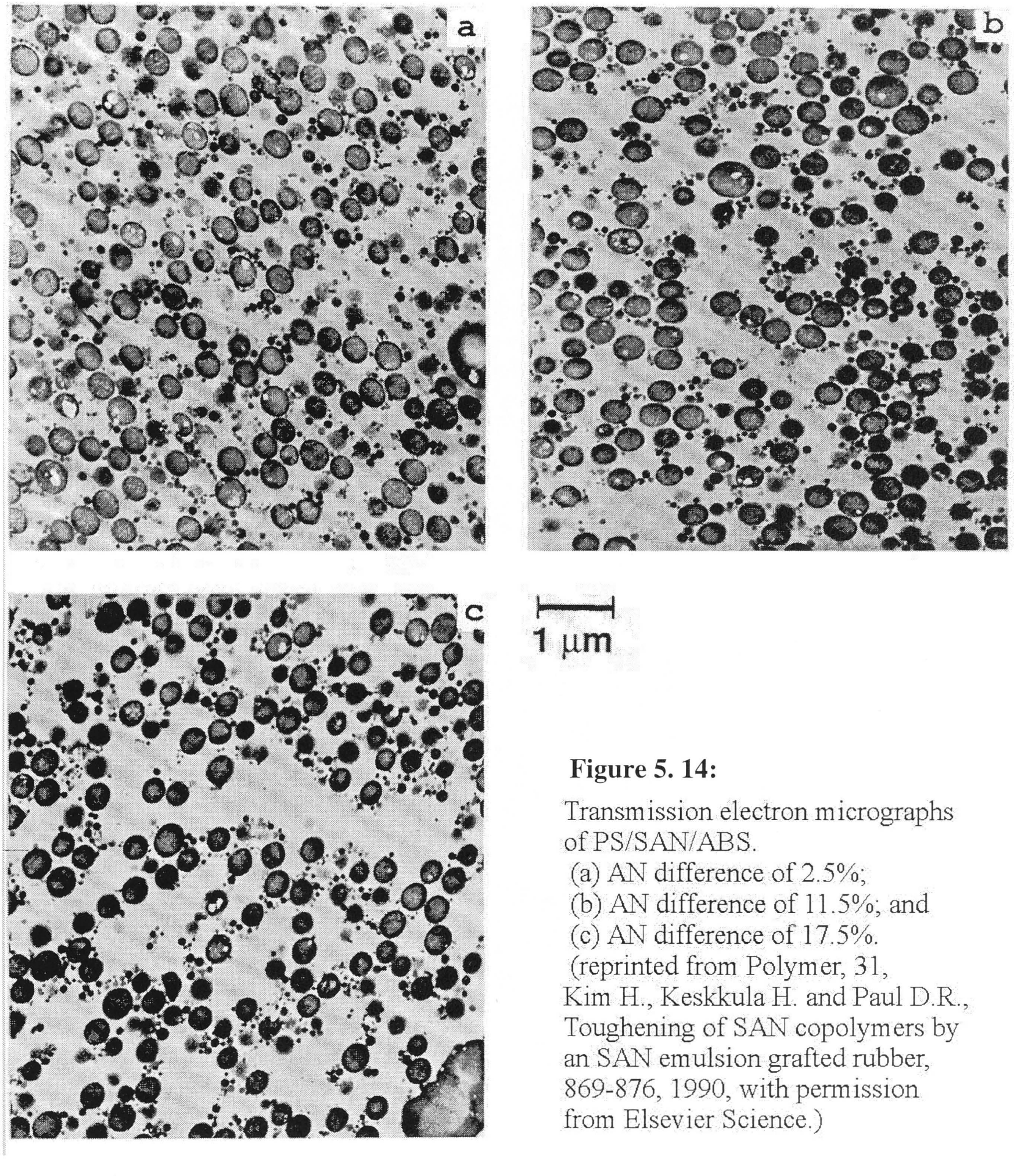

Figure 5. 14:

Transmission electron micrographs of PS/SAN/ABS.
(a) AN difference of 2.5%;
(b) AN difference of 11.5%; and
(c) AN difference of 17.5%.
(reprinted from Polymer, 31, Kim H., Keskkula H. and Paul D.R., Toughening of SAN copolymers by an SAN emulsion grafted rubber, 869-876, 1990, with permission from Elsevier Science.)

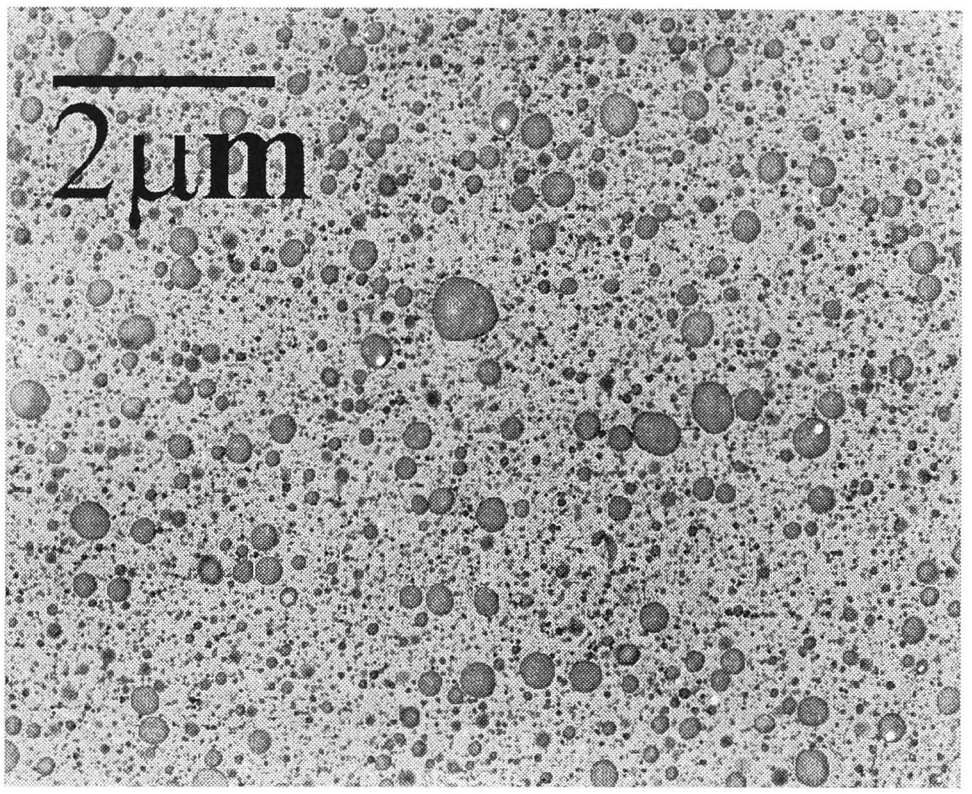

(a)

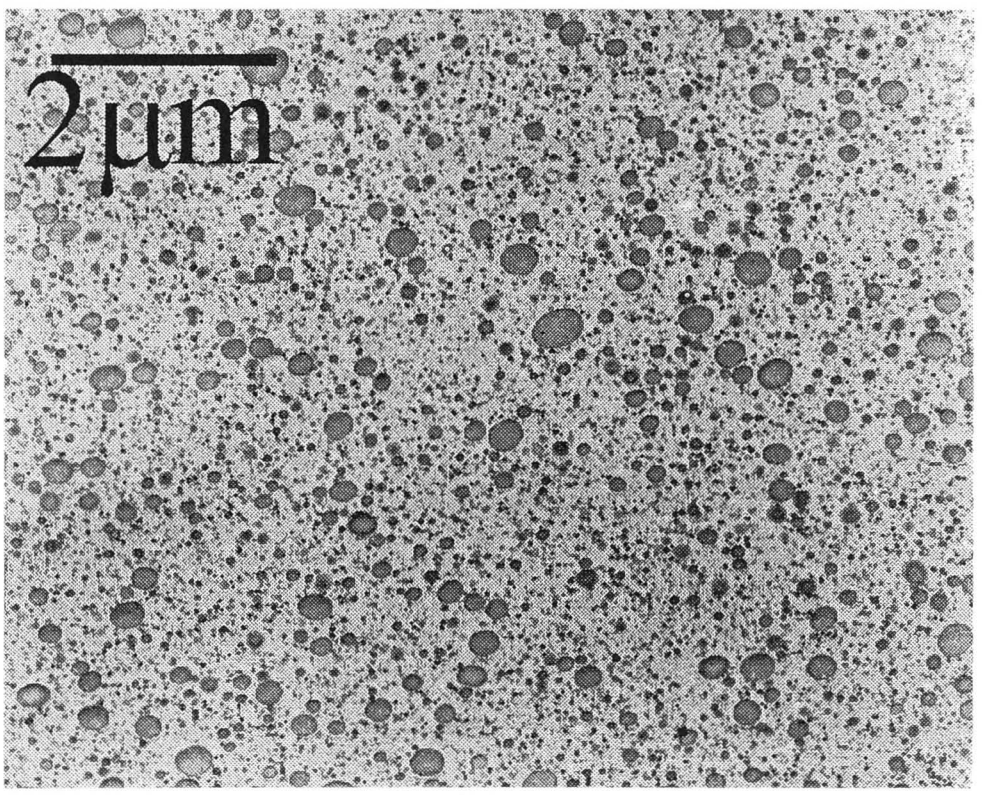

(b)

Figure 5. 15: Transmission electron micrographs of ABS1 and ABS5 for particle agglomeration comparison. (a) ABS1 with SAN22; (b) ABS1 with SAN28a;

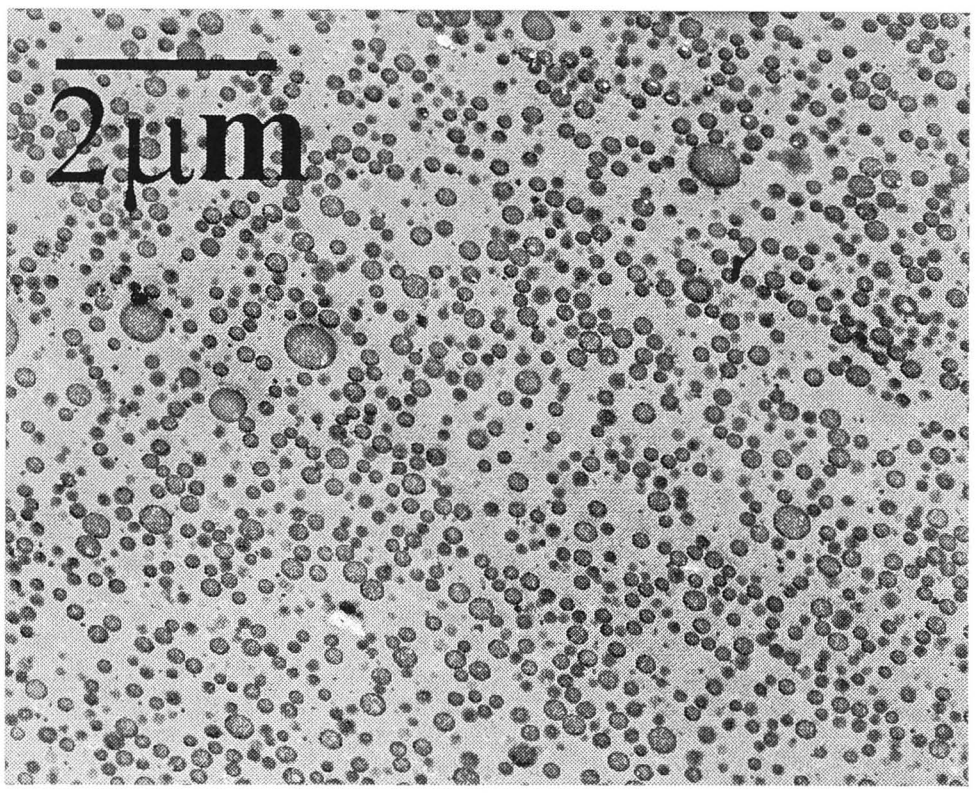

(c)

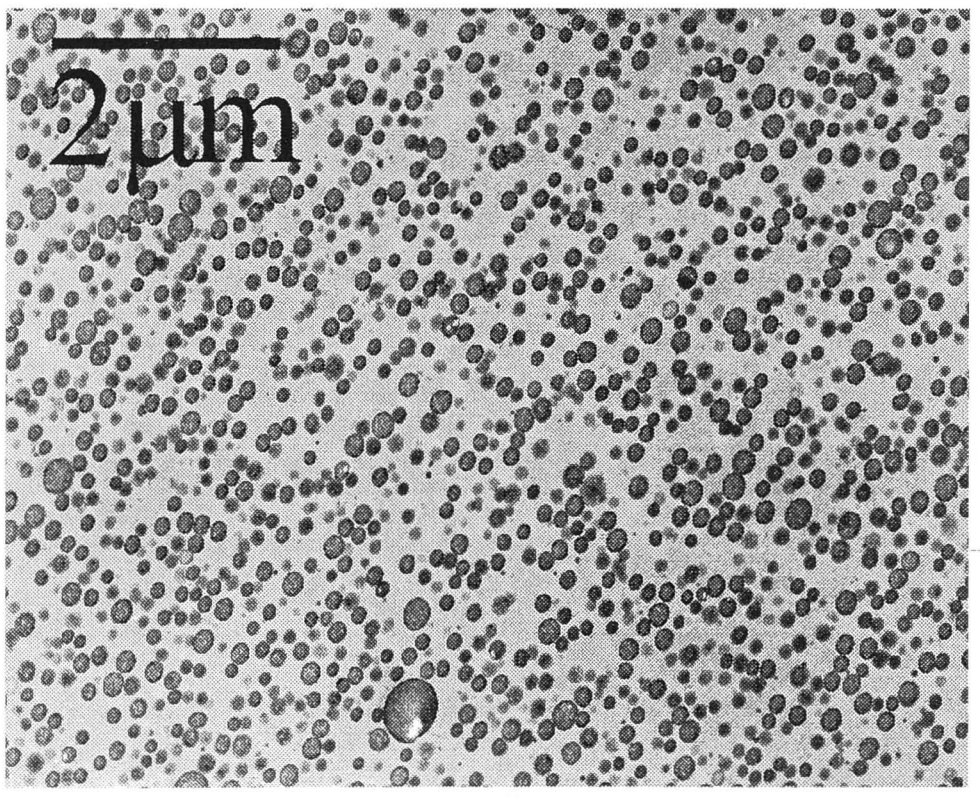

(d)

Figure 5. 15: (c) ABS5 with SAN22; and (d) ABS5 with SAN28a

1-2 μm could provide the optimum toughness in HIPS, for monomodal distributed particles. Subsequently, bimodal distributed particles were also found to significantly increase the toughness, compared to monomodal distributed particles of the same rubber content[98].

Despite the potential effect of rubber particle size on particle cavitation[15, 25, 99, 100], such an effect was not evident in this study. Particle cavitation occurred in ABS1-type particles regardless of whether the particles were 0.1 μm or 0.5 μm in diameter. On the other hand, ABS5-type particles (0.3 μm in diameter) did not generally cavitate as easily as ABS1-type particles. The next question is whether particle size distribution plays a part in toughening of the materials.

Okamoto and coworkers[101] have shown using finite element (FE) modeling that HIPS with bimodal particle size distribution have better toughness. They noticed that the greater the difference between the particle sizes in the bimodal HIPS, the better the impact strength. This is because the stress concentration caused by large particles (4.9 μm) on the surface of small particles (0.2 μm) is higher than that caused by medium-sized particle (1.0 μm). Both large and small particles nucleate crazes, but only crazes initiated from the large particles grow to catastrophic size.

The bimodal particle size distribution ratio in ABS1 corresponds to that of Okamoto's model with rubber particle diameter ratio of 1:5. They have observed that HIPS with rubber particle diameter ratio of 1:5 showed only a minute increase in impact strength compared to monomodal distributed particles. A significant increase in impact strength is noticeable only when the ratio reaches 1:25. Therefore we believe that for our ABS1 system, the rubber particle diameter ratio of 1:5 has little effect on the toughness.

The relationship between good mechanical properties of ABS1 and the extensive particle cavitation observed in the micrographs generates a speculation that particle cavitation yields better mechanical results in rubber-toughened polymers. However, particle cavitation itself cannot be the main influence on the mechanical properties[17, 81, 82]. Rather, it was shear yielding, present in ABS1, in conjunction with the extensive rubber particle cavitation, that increases its toughness. ABS5-type particles, which lack extensive particle cavitation, did not show shear deformation and had lower toughness. However, ABS15 did not show any sign of matrix shear yielding, even though there was reasonable amount of particle cavitation.

Wu[102] acknowledged that ligament thickness contributes to the toughening effects. Judging from the equation derived by Wu, the ligament thickness of monomodal ABS5 is proportional to the particle size. Bimodal ABS1, with a number of smaller particles, would result in a thin ligament thickness. However, based on Wu's observation, the ductile-brittle transition occurs in a shear-dominant material, with ligament thickness as a critical parameter. Since ABS1 and ABS5 did not have the same deformation mechanisms, the ligament thickness effect can not be the main cause of toughness difference.

A recent study by Argon and Cohen[85] showed that butadiene molecules were absorbed into crazes by a pressure differential. This could provide a cause for the cavitation of particle in the ABS. However, it was noted that ABS1 has less crazing and more cavitation than ABS5. Therefore, crazing is not the main reason for particle cavitation in ABS1. The remaining possibility that may cause particle in ABS1 to cavitate more easily than ABS5-type particles is particle structure. The difference in particle structure, homogeneous versus salami-type, may cause difference in Poisson's ratio of the particles, thus affecting the deformation mechanism. This speculation is supported by Narisawa et al.[22] who used FE modeling to show a dramatic increase in the particles' dilatational stress for Poisson's ratio (ν) from 0.4990 to 0.4999. If different particle structure relates to a difference in Poisson's ratio, it is believed that the variation in the dilatational stress caused the different deformation mechanisms, thus toughness. ABS1-type particles, with a homogeneous structure, inherit a higher ν than the SAN-occluded ABS5-type particles. Under the same loading condition, ABS1-type particles have higher stresses. This generates cavitation in ABS1-type particles, possibly before exceeding the maximum yield strength. This idea is also indirectly supported by the finding of Bucknall et al.[103], that the addition of sulfur decreases the toughness of rubber toughened polymers, because of the increase of cross-link density in the particles and thus decrease of the Poisson's ratio.

It should be noted that the above explanation was different from that made by Donald and Kramer[25], who observed, in solution-cast thin-film specimens, that small particles (0.1 μm) in diameter showed little tendency to craze but cavitated more easily. Since the solution-cast thin-film can represent bulk deformation behaviour[104], Donald and Kramer suggested that in an ABS with a bimodal particle size distribution of 0.1 μm and 1.5 μm diameter the large particles nucleate craze and the small

particles cavitate and promote matrix shear yielding. It should also be noted that in Donald and Kramer's system the small particles were of uniform structure and the large particle has a salami structure, as those in the ABS1 and ABS5 used in this study.

5.7 Concluding remarks

This work involves two types of rubber particles. The main influence affecting the deformation behaviour, and therefore the toughness, is the structure of the particles. It shows that different deformation behaviours were induced by these particles. Ligament thickness, particle size and size distribution are considered to be secondary influences.

AN content effect was examined and was found to affect only the inherent ductility of the materials, as discussed in Chapter 4. AN content mismatch was not found to cause agglomeration of the rubber particles. This could be due to the insignificant AN content mismatch (5.9 wt%), compared to that studied by Kim and Chang (11.5 wt%).

The toughening mechanisms observed by electron microscopy consist of crazing and particle cavitation. It is concluded that ABS1-type particles, regardless of particle size, are vulnerable to cavitation, whereas ABS5-type particles initiate crazes. An ABS1-type particle, with its homogeneous structure, is thought to induce shear yielding in the matrix whereas the salami structured ABS5-type particle initiates crazing. The factor affecting the deformation behaviours of these particles is suggested to be the Poisson's ratio. However, strain rate may also influence the deformation behaviours.

When considering the results from SAXS and electron microscopy, the circular pattern of SAXS corresponds to crazing, and the elliptical shape to shear yielding. The circular pattern appears in both ABS5 and ABS15 materials and the elliptical pattern only in ABS1 materials. It is concluded that crazing dominates in both ABS5 and ABS15. This helps to explain why the toughness of ABS15 is closer to the toughness of ABS5, than to that of ABS1 in which shear yielding dominates.

CHAPTER SIX

Conclusions

The main objective of this work was to determine the effect of different rubber particle structures on the mechanical properties of polymers. The effects of the miscibility of polymer blends, particle size and particle distribution have also been elucidated. The conclusions reached from this work are as follows:

1. All blends measured with differential scanning calorimeter (DSC) show a single glass transition temperature (T_g), therefore SMI is relatively miscible with SAN. However, the degree of miscibility decreases with the increase in the acrylonitrile (AN) content of SAN. The high molecular weight (M_w) of SAN also decreases the miscibility of the blends. The miscibility of SAN and SMI increases when SMI is blended with two SANs of a high AN content mismatch. It is believed that the repulsion force between the two SANs makes them more miscible with SMI.

2. The study of pure polymer blends shows that AN content effects toughness of the polymer by affecting stability of craze growth. Crazing is the dominant toughening mechanism for pure polymer blends. Stable craze growth was observed in the pure SAN28a copolymer, which correspondingly has better toughness than other copolymers. The inherent toughness increases with the increase in acrylonitrile content.

3. Significant differences in the mechanical properties at *low* and *intermediate* strain rates are evident with an increase in AN content. However, at a *high* strain rate there is no change in the toughness with AN content in the case of SAN copolymers. The only difference that is observed following the application of a *high* strain rate, is in the formation of whiskers in SAN copolymers. The length of these whiskers depends on the AN content of the materials. High AN content

causes longer whiskers than low AN content. The whiskers observed in Izod specimens reveal that the Izod impact test is a Mode I test.

4. The mismatch between AN content in SAN_m and SAN_g did not cause particle agglomeration, although the mismatch in this work may be too small to show a significant effect.

5. TEM micrographs show that both large (0.5 μm) and small (0.1 μm) homogeneous particles in ABS1 cavitate more readily than salami-structured particles in ABS5 of 0.3 μm. ABS5 particles initiate crazes more easily than ABS1 particles. Therefore, the deformations were not caused by the size of the particle, but by the particle structure.

6. In small angle X-ray scattering (SAXS) the rhombus patterns correspond to shear deformation and circular patterns to no deformation or crazing. SAXS results confirm that shear yielding is dominant in ABS1, and crazing in ABS5 and ABS15.

7. The difference in deformation between ABS1 and ABS5 is attributed to the difference in particle structures. Homogeneous particles in ABS1 have a higher Poisson's ratio than salami structured particles in ABS5. The high Poisson's ratio in homogeneous particles is believed to cause shear yielding in ABS1. The high Poisson's ratio induces a high bulk modulus, and thus causes ABS1-type particles to cavitate more easily than ABS5-type particles.

8. The mechanical properties of ABS15 material were closer to ABS5 than ABS1, because of uneven distribution of the rubber particles in ABS15. It was found that the mixture of ABS1 and ABS5 induced ABS1- and ABS5-rich regions in ABS15. The weaker ABS5-rich region in ABS15 fails before the ABS1-rich region fractures, hence crazing is the main deformation mechanism in ABS15 material.

CHAPTER SEVEN

Recommendations for future research

1. Rubber particles have been shown[29, 30, 95] to agglomerate if the acrylonitrile (AN) content mismatch between the matrix and grafted SANs is great. However, this effect was not observed in this work. It is believed that the AN content mismatch used in this study was too small to allow particle agglomeration to take effect. To determine the effect of particle agglomeration, higher AN content mismatch should be used.

2. It has been shown in this thesis that ABS15 has mechanical properties closer to ABS5 than to ABS1. The examination shows that ABS15 consisted of ABS1- and ABS5-rich regions. It was the weaker ABS5-rich regions that fail before the ABS1-rich regions fail, thus giving ABS15 similar deformation behaviour to ABS5. Future study may uncover a way to uniformly distribute the particles during processing, thus eliminating early failure due to a particular rich region.

3. Particle structures play an enormous role in the fracture behaviour of the materials. By varying the Poisson's ratio in the rubber particles, different types of deformation can be obtained and thus different mechanical results. Further studies could be conducted to determine the effect of SAN occlusion in the particles rather than focusing on the Poisson's ratio, perhaps incorporating the use of core-shell rubber to examine whether this phenomenon occurs.

References

1 P. R. Couchman, Macromolecules **11**, 1156 (1978).

2 H. R. Brown, A. S. Argon, R. E. Cohen, *et al.*, Macromolecules **22**, 1002 (1989).

3 A. M. Donald and E. J. Kramer, Philosophical Magazine A **43**, 857 (1981).

4 A. M. Donald and E. J. Kramer, Journal of Polymer Science **20**, 899 (1982).

5 I. Narisawa, T. Kuriyama, and A. Takaki, in *International Symposium on Polymer Alloys and Composites*, edited by C. L. Choy and F. G. Shin (Hong Kong Polytechnic, Hong Kong, 1992), p. 80.

6 D. Dompas and G. Groeninckx, Polymer **35**, 4743 (1994).

7 D. Dompas, G. Groeninckx, M. Isogawa, *et al.*, Polymer **35**, 4750 (1994).

8 A. Takaki, H. Yasui, and I. Narisawa, Polymer Engineering & Science **37**, 105 (1997).

9 K. Dijkstra, J. Terlaak, and R. J. Gaymans, Polymer **35**, 315 (1994).

10 K. Dijkstra and R. J. Gaymans, Polymer **35**, 332 (1994).

11 C. B. Bucknall, P. S. Heather, and A. Lazzeri, Journal of Materials Science **16**, 2255 (1989).

12 A. J. Kinloch, S. J. Shaw, D. A. Tod, *et al.*, Polymer **24**, 1341 (1983).

13 A. J. Kinloch and D. L. Hunston, Journal of Materials Science: Letter **6**, 131 (1987).

14 F. J. Guild and A. J. Kinloch, Journal of Materials Science **30**, 1689 (1995).

15 R. A. Pearson and A. F. Yee, Journal of Materials Science **26**, 3828 (1991).

16 A. F. Yee, D. M. Li, and X. W. Li, Journal of Materials Science **28**, 6392 (1993).

17 S. Newman and S. Strella, Journal of Applied Polymer Science **9**, 2297 (1965).

18 A. F. Yee and R. A. Pearson, Journal of Materials Science **21**, 2462 (1986).

19 H.-J. Sue and A. F. Yee, Journal of Materials Science **24**, 1447 (1989).

20 C. B. Bucknall and A. Lazzeri, in *37th International Symposium on Macromolecules*, Gold Coast, (1998), p. 580.

21 I. Narisawa, T. Kuriyama, and K. Ojima, Makromolecular Chemistry, Macromolecular Symposium **41**, 87 (1991).

22 I. Narisawa and T. Kuriyama, Macromolecular Symposium **101**, 273 (1996).

23 C. B. Bucknall, *Toughened plastics* (Applied Science, 1977).

24 B. S. Lombardo, H. Keskkula, and D. R. Paul, Journal of Applied Polymer Science **54**, 1697 (1994).

25 A. M. Donald and E. J. Kramer, Journal of Materials Science **17**, 1765 (1982).

26 C. C. Chen, in *Mechanics and Material Science* (The State University of New Jersey, New Brunswick Rutgers, 1983).

27 Y. Aoki, Macromolecules **20**, 2208 (1987).

28 M. C. O. Chang and R. L. Nemeth, Journal of Applied Polymer Science **62**, 553 (1997).

29 H. Kim, H. Keskkula, and D. R. Paul, Polymer **31**, 869 (1990).

30 H. Kim, H. Keskkula, and D. R. Paul, Polymer **32**, 1447 (1991).

31 P. Beguelin and H. H. Kausch, Journal of Materials Science **29**, 91 (1994).

32 T. Kuboki, Ph.D. Thesis, (Kyushu University, 1999).

33 T. Vu-Khanh, Theoretical and Applied Fracture Mechanics **29**, 75 (1998).

34 Y. Aoki, in *Mechanical Behaviour of Materials - VI*, edited by M. a. I. Y. Jono (Pergamon Press, Oxford, England, 1991), Vol. 3, p. 269.

35 Y. Aoki, Macromolecules **21**, 1277 (1988).

36 S. Havriliak, C. A. Cruz, and S. E. Slavin, Polymer Engineering & Science **36**, 2327 (1996).

37 P.-Y. B. Jar and D. Creagh, (Report to the Australian National Beamline Facility, Australian Synchrotron Research Program, Canberra, 1999).

38 S. Rostami, in *Multicomponent polymer systems*, edited by I. S. Miles and S. Rostami (Longman Scientific and Technical, Essex, 1992), p. 63.

39 L. A. Utracki, *Polymer alloys and blends - thermodynamics and rheology* (Hanser publishers, New York, 1989).

40 O. Olabisi, L. M. Robeson, and M. T. Shaw, *Polymer-polymer miscibility* (Academic press, New York, 1995), p. 55.

41 P. J. Flory, *Principles of polymer chemistry* (Cornell university press, New York, 1953), Chapter 11

42 T. Kaneko and T. Shinmura, New Materials Technology and Applications **5**, 60 (1994).

43 W. J. MacKnight, F. E. Karasz, and J. R. Fried, in *Polymer Blends*, edited by D. R. Paul and S. Newman (Academic press, New York, 1978), Vol. 1, p. 185.

44 S. Kole, A. Bhattacharya, D. K. Tripathy, *et al.*, Journal of Applied Polymer Science **48**, 529 (1993).

45 P. J. Flory, Journal of Chemical Physics **10**, 51 (1942).

46 M. L. Huggins, Journal of Physical Chemistry **46**, 151 (1942).

47 R. L. Scott, Journal of Chemical Physics **17**, 279 (1949).

48 S. Krause, in *Polymer blends*, edited by D. R. Paul and S. Newman (Academic press, New York, 1978), Vol. 1, p. 15.

49 M. Nishimoto, H. Keskkula, and D. R. Paul, Polymer **30**, 1279 (1989).

50 K. Takakuwa, S. Gupta, and D. R. Paul, Journal of Polymer Science Part B-Polymer Physics **32**, 1719 (1994).

51 P.-Y. B. Jar, K. Takahashi, and T. Shinmura, Unpublished work, (1999).

52 A. Eisenberg, *Physical properties of polymers* (ACS professional reference book, Washington D.C., 1993).

53 M. Nishimoto, H. Keskkula, and D. R. Paul, Macromolecules **23**, 3633 (1990).

54 P.-Y. B. Jar, K. Takahashi, and T. Shinmura, in *Materials in the automotive industry* (Institute of Metals and Materials Australasia Ltd, Melbourne, Australia, 1996), p. 57.

55 G. E. Molau, Polymer Letters **3**, 1007 (1965).

56 E. J. Kramer and L. L. Berger, in *Crazing in Polymers Vol. 2*, edited by H.-H. Kausch (Springer-Verlag, Heidelberg, 1990), Vol. 2, p. 1.

57 E. J. Kramer, in *Crazing in Polymers Vol. 2*, edited by H.-H. Kausch (Springer-Verlag, Heidelberg, 1983), Vol. 1, p. 1.

58 P.-Y. Jar, Ph.D. Thesis, (Rutgers University, 1988).

59 H. Kim, H. Keskkula, and D. R. Paul, Polymer **32**, 2372 (1991).

60 D. Quintens, G. Groeninckx, M. Guest, *et al.*, Polymer Engineering and Science **31**, 1215 (1991).

61 J. Murray and D. Hull, Polymer **10**, 451 (1969).

62 B. D. Lauterwasser and E. J. Kramer, Philosophical Magazine: A **39**, 469 (1979).

63 J. Murray and D. Hull, Journal of Polymer Science: Part A-2 **8**, 1521 (1970).

64 J. A. Sauer and G. C. Richardson, International Journal of Fracture **16**, 499 (1980).

65 R. W. Nunes, J. R. Martin, and J. F. Johnson, Polymer Engineering and Science **22**, 205 (1982).

66 J. A. Sauer and M. Hara, in *Crazing in Polymers Vol. 2*, edited by H.-H. Kausch (Springer-Verlag, Heidelberg, 1990), Vol. 2, p. 69.

67 A. S. Argon and M. I. Bessonov, Philosophical Magazine **35**, 917 (1977).

68 A. S. Argon and J. G. Hannosh, Philosophical Magazine **36**, 1195 (1977).

69 A. C.-M. Yang and E. J. Kramer, Journal of Materials Science **21**, 3601 (1986).

70 H. R. Brown, Macromolecules **24**, 2752 (1991).

71 B. H. Bersted and T. G. Anderson, Journal of Applied Polymer Science **39**, 499 (1990).

72 P. Compston, P.-Y. B. Jar, and K. Takahashi, in *2nd ESIS TC4 Conference on Polymers and Composites*, Switzerland, (1999), 47.

73 M. Todo, K. Takahashi, P. Beguelin, *et al.*, JSME International Journal **42**, 49 (1999).

74 W. Jiang, H. Liang, and B. Jiang, Polymer **39**, 4437 (1998).

75 J. G. Williams, *Fracture mechanics of polymers* (Ellis Horwood Ltd, Chichester, 1984).

76 D. G. Gilbert and A. M. Donald, Journal of Materials Science **21**, 1819 (1986).

77 R. W. Truss, in *22nd Australasian Polymer Symposium*, Auckland, New Zealand, (1997), p. 123.

78 R. P. Kambour, Journal of Polymer Science: Macromolecular reviews **7**, 1 (1973).

79 A. J. Oshinski, H. Keskkula, and D. R. Paul, Polymer **37**, 4891 (1996).

80 M. E. Fowler, H. Keskkula, and D. R. Paul, Journal of Applied Polymer Science **35**, 1563 (1988).

81 V. V. Kozii and B. A. Rosenberg, Polymer Science **34**, 919 (1992).

82 C. B. Bucknall, A. Karpodinis, and X. C. Zhang, Journal of Materials Science **29**, 3377 (1994).

83 Y. Okamoto, H. Miyagi, T. Uno, *et al.*, Polymer Engineering & Science **33**, 1606 (1993).
84 A. J. Kinloch and R. J. Young, *Fracture behaviour of polymers* (Elsevier Applied Science, London, 1983).
85 A. S. Argon and R. E. Cohen, in *Advances Polymer Science*, edited by H. H. Kausch (Springer-Verlag, Berlin, 1990), Vol. 91/92, p. 301.
86 M. E. J. Dekkers and D. Heikens, Journal of Materials Science **20**, 3873 (1985).
87 D. S. Parker, H.-J. Sue, J. Huang, *et al.*, Polymer **31**, 2267 (1990).
88 W.-Y. Chiang and D.-S. Hwung, Polymer Engineering and Science **27**, 632 (1987).
89 Y. Huang and A. J. Kinloch, Journal of Materials Science Letters **11**, 484 (1992).
90 Y. Huang and A. J. Kinloch, Journal of Materials Science **27**, 2763 (1992).
91 Y. Huang and A. J. Kinloch, Journal of Materials Science **27**, 2753 (1992).
92 H. R. Brown and E. J. Kramer, Journal of Macromolecular Science, (Phys) **B19(3)**, 487 (1981).
93 H. Breuer, F. Haff, and J. Stabenow, Journal of Macromolecular Science and Physics **B14**, 387 (1977).
94 Y. Aoki, Polymer Journal **14**, 951 (1982).
95 M. C. O. Chang and R. L. Nemeth, Journal of Applied Polymer Science **61**, 1003 (1996).
96 C. B. Bucknall, in *Polymer Blends*, edited by D. R. Paul and S. Newman (Academic, New York, 1978), Vol. 2, p. 99.
97 A. M. Donald and E. J. Kramer, Journal of Materials Science **17**, 2351 (1982).
98 S. Y. Hobbs, Polymer Engineering and Science **26**, 74 (1986).
99 C. Fond, A. Lobbrecht, and R. Schirrer, International Journal of Fracture **77**, 141 (1996).
100 F. S. Shieu, Polymer **38**, 3135 (1997).
101 Y. Okamoto, H. Miyagi, M. Kakugo, *et al.*, Macromolecules **24**, 5639 (1991).
102 S. Wu, Journal of Applied Polymer Science **35**, 549 (1988).
103 C. B. Bucknall, B. O'Connor, and J. L. Hahnfeld, in *37th International Symposium on Macromolecules*, Gold Coast, (1998), p. 486.
104 P. Beahan, M. Bevis, and D. Hull, Journal of Materials Science **8**, 162 (1972).